



# The Planetary Boundary Layer – where are we now?

Christopher “Chuck” C. Baker, Jr.

Department of Atmospheric and Oceanic Science, University  
of Maryland, College Park, MD 20742, USA  
Earth System Science Interdisciplinary System, University of  
Maryland, College Park, MD 20740, USA  
E-mail: [torcha98@umd.edu](mailto:torcha98@umd.edu)

**Abstract-** *The Planetary Boundary Layer (PBL) is the surface layer of the troposphere that is characterized by rotational turbulent mixing of heat, moisture and momentum. Given the PBL's proximity to Earth's surface, it is the first layer in which heat, moisture and momentum must pass through to reach the free atmosphere. Understanding the PBL's mixing processes of such variables are critical to characterizing weather convection, cloud formation and aerosol disposition between the surface and the atmosphere. Over the past several decades, research has greatly expanded knowledge of the PBL structure, thanks to improvements in experiments, observations (measurements) and simulations. This review summarizes advancements made in these areas, identifying the advantages and disadvantages involved with each technique.*

**Index Terms-** *Planetary boundary layer, near-surface weather parameterization, numerical weather prediction, land-surface interactions*

## I. INTRODUCTION

National Aeronautics and Space Administration (NASA) data indicated that the Summer of 2020 tied with 2016 as the warmest summer in world history since the late 1800s [1]. And scientists from the World Weather Attribution Project went a step further by showing that global warming from climate change was the main culprit causing this extreme heat wave event [2]. Further, when diagnosing the causes of this heat wave, scientists showed that certain changes in Earth's surface air layer were necessary for heat wave formation, implying that being able to predict such changes in the surface layer would improve predictions [3].

But Earth's surface air layer doesn't just influence heat wave formation. Also known as the planetary boundary layer (PBL), it is the first atmospheric layer in which heat, moisture, emittance and momentum pass through to reach

the upper atmosphere [4], [5], [5]–[7]. The moisture level in the PBL also plays a significant role in determining the potential for storm development from available latent heat release [4], [8]. It is therefore apparent how understanding PBL spatiotemporal fluctuations and characteristics is crucial to knowing how and where weather occurs, cloud formation and pollution/emission concentrations in the atmosphere [4], [5], [5], [7], [9]–[11].

The title of this review is meant to elicit thoughts about the development in our comprehension of the PBL over the last several decades. A history of the PBL's background, characteristics and importance to atmospheric science is initially presented, followed by a review of several methods and their respective advantages and disadvantages to modeling the PBL, addressing their preference and feasibility. These methods include both observational (e.g., soundings, radar/lidar measurements) and numerical (e.g., turbulence closure, mixing schemes) techniques that can determine the structure and evolution of the PBL. We then conclude the review with challenges and future directions of PBL research.

## II. BACKGROUND

### A. Origin of Boundary Layer Theory

The concept of the planetary boundary layer was first introduced in the early 1900s by German meteorologist Richard Assmann [12]. In 1904, he conducted a series of balloon soundings to study the vertical structure of the atmosphere, observing that the temperature decreased with height, but the rate of decrease varied at different levels. He concluded that the atmosphere was not well mixed, and there were different layers of air



with distinct characteristics [12], [13].

Later in the 1930s, American meteorologist Horace Byers expounded on Assmann's research by conducting a series of experiments to study the properties of the atmosphere near the Earth's surface [13]–[15]. He used tethered balloons equipped with instruments to measure temperature, humidity, and wind speed at different heights. Byers observed that the temperature and humidity varied significantly within the first few hundred meters above the ground, suggesting that this atmospheric layer was distinct from the rest of the atmosphere, designating it as the "mixed layer" [13]–[16].

A little time later, British meteorologist George Sutton conducted a similar experiment using a hot air balloon, measuring temperature and humidity at different heights. He found that there was a sharp decrease in temperature and humidity within the first few hundred meters above the ground [17]–[19]. Sutton suggested that this layer of the atmosphere was characterized by strong turbulence and was separated from the free atmosphere by a layer of stable air, calling it the "surface layer" [13], [18], [19].

But the term 'planetary boundary layer' wasn't used until later in the 1950s and 60s, when several atmospheric scientists conducted experiments to study the properties of the atmosphere near the Earth's surface [18]. They verified Assmann and Sutton's observations that *globally*, the layer of the atmosphere characterized by strong turbulence and rapid changes in temperature and humidity was separated from the rest of the atmosphere by a layer of stable air [18]–[20]. Today, the term planetary boundary layer<sup>1</sup> continues to reflect the global-scale nature and role it plays in modulating a range of physical and chemical processes in the Earth's atmospheric system [13], [16]–[19].

## B. Structure of the PBL

The PBL's structure and dynamics are complex and depend on a variety of factors, including surface temperature, wind speed, turbulence, and atmospheric stability. The vertical structure of the PBL is made up of several independent layers, each having unique characteristics from the other (see [Figure 1](#)).

The surface layer extends from the Earth's surface up to a height of 20–30 meters. It is strongly influenced by the characteristics of the underlying surface, such as roughness, temperature, and moisture content [17]. Within this layer, wind speeds and temperature gradients are typically high (vary rapidly in space and time), and turbulence is strong [7], [14]. The surface layer can change significantly throughout the day due to the heating and cooling of the Earth's surface by the Sun. As the Sun heats the Earth's surface, the surface temperature increases, causing the air near the surface to warm and rise. This process creates vertical motion in the atmosphere, which can mix the air and pollutants near the surface into the upper layers of the PBL [22], [23]. As the mixed air rises, it cools and sinks back down to the surface, creating a cycle of turbulence and mixing in the PBL [22], [24]. The height of the surface layer can also vary throughout the day. In the morning, the surface layer is typically shallow and well-mixed, as the air near the surface has cooled overnight and is relatively uniform in temperature and humidity [4], [25]. As the Sun rises and heats the surface, the surface layer can deepen, allowing for more turbulence and mixing [4]. In the late afternoon, as the Sun begins to set, the surface layer can become more stable, as the Earth's surface cools and the temperature difference between the surface and the upper layers of the PBL decreases [4]. This stability can limit the mixing of pollutants and other atmospheric constituents, leading to poor air quality in some cases [17],

---

<sup>1</sup> The planetary boundary layer (PBL) is occasionally interchanged with the atmospheric boundary layer (ABL) in literature, with both commonly used to describe the atmospheric layer closest to Earth's surface (where the effects of the surface can be felt) [16], [18], [19], [21]. While their definitions overlap, the ABL is a more specific concept that refers to the air directly influenced by surface processes, where the PBL encompasses the entire layer of air that is influenced by the Earth's surface, whether directly or indirectly, which includes the ABL [19], [21]. Although the term "ABL" may be used more broadly to refer to the entire layer of air that is influenced by the Earth's surface (including the layer of air above the ABL), to avoid confusion, it is important to pay attention to the context in which these terms are used and to clarify any potential ambiguity between them [16], [18], [19], [21].



[25], [26].

Immediately above the surface layer is called the mixed layer<sup>2</sup>, characterized by a more uniform temperature and moisture profile [22], [24]. Any present turbulence is relatively uniform and well-mixed, with little variation in wind speed and temperature [22]. These characteristics can change throughout the day as a result of changes in atmospheric conditions, particularly the heating and cooling of the Earth's surface. During the daytime, the Earth's surface is heated by the sun, which causes the air near the surface to warm and rise. This creates turbulence and mixing in the PBL, deepening the mixed layer as warm air rises and cool air sinks [4], [22]. The depth of the mixed layer increases until it reaches a maximum depth in the afternoon or early evening [4]. The thickness of the mixed layer is influenced by factors such as the strength of the sun's radiation, surface roughness, and wind speed [22], [24], [27]. As the sun sets, the Earth's surface begins to cool, decreasing surface air temperature. This creates a more stable atmospheric condition, which reduces turbulence and mixing in the PBL [24]. The mixed layer gradually becomes shallower as the air near the surface becomes more stable, and the depth of the mixed layer decreases until it reaches a minimum depth in the early morning hours [22], [25].

The residual layer extends from the top of the mixed layer to the height of the residual layer top, which can be several kilometers above the Earth's surface. Within this layer, air is relatively stable, and turbulence is weak, leading to little mixing of air between the residual layer and the mixed layer [4], [28]. During the daytime, the Earth's surface is heated by the sun, which causes the air near the surface to warm and rise. This creates turbulence and mixing in the PBL, which leads to the upward transport of air and pollutants from the mixed layer to the residual layer [24]. As a result, the residual layer becomes enriched with pollutants and becomes more well-mixed than it was at the start of the day [24]. As the sun sets, the Earth's surface begins to cool, decreasing surface air temperature and creating a more stable atmospheric condition, which

reduces turbulence and mixing in the PBL. The air in the residual layer becomes more isolated from the surface and becomes more stable, leading to a decrease in the mixing of air and pollutants within the residual layer [4], [22], [27].

The transition layer is the layer that separates the mixed layer from the residual layer, characterized by a gradual transition from properties of the mixed layer (e.g., air is well-mixed by turbulence and convection) to properties of the residual layer (e.g., air is relatively stable) [5], [10], [27]. During the daytime, air rising due to surface heating creates turbulence and mixing in the PBL, deepening and shrinking the mixed layer as warm air rises and cool air sinks [7]. As a result, the transition layer is relatively thin. When the sun sets, the Earth's surface begins to cool, and the temperature of the air near the surface decreases. This creates a more stable atmospheric condition, which reduces turbulence and mixing in the PBL, resulting in a shallower mixed layer [10], [27]. This in turn expands the transition layer, as the air in this layer becomes more distinct from that of the mixed layer [5], [10]. Eventually, the PBL becomes decoupled, and the residual layer remains stable throughout the night [10], [24], [27].

These vertical features of the PBL can also be affected by geographic location and topography ([see Figure 2](#)). Geographic location can influence the behavior of the PBL because different regions of the Earth experience different amounts of solar radiation and have different surface properties, such as vegetation cover and soil moisture [7], [9], [22]. For example, the PBL over a desert region will behave differently than the PBL over a forested region, as the desert region will have a lower moisture content and a higher surface temperature, which can lead to different atmospheric conditions and behavior in the PBL. Topology can also play a role in PBL behavior because it can affect the flow of air and the interaction between the atmosphere and the underlying surface. For example, mountains can act as a barrier to the flow of air, which can lead

---

<sup>2</sup> The mixed layer is sometimes referred to as the convective boundary layer because it is often driven by convection [22], [24]. The vertical motion from solar surface heating leads to mixing of air in the mixed layer, similar to the process of convection (hence the name "convective boundary layer") [22], [24].



to the formation of different types of turbulence and variations in atmospheric stability [7], [29]. Coastal regions can also experience unique PBL behavior due to the influence of the ocean, such as the formation of sea breezes and the transport of marine aerosols inland [7], [30].

### C. Dynamics of the PBL

As a highly dynamic and variable layer of the atmosphere, the PBL's dynamics are influenced by a wide range of factors, primarily through fluxes in solar radiation, wind, and atmospheric stability.

Solar radiation provides the energy that drives the PBL dynamics by heating the Earth's surface [4], [8], [25], [31]. As the surface temperature increases, it creates a temperature gradient between the surface and the overlying atmosphere [4]. This temperature gradient creates convective motions that mix the air and create turbulence within the PBL [4]. The strength of the convective motions depends on the amount of solar radiation that reaches the surface and the surface type (e.g., land or water). During the day, the PBL can grow to several kilometers in height due to the strong convective mixing driven by solar radiation [4], [5], [7]. However, at night, the solar radiation decreases, and the PBL can become shallower and more stable due to the absence of convective mixing, which can trap pollutants near the surface and cause poor air quality [22], [23], [26].

The wind is another influencing factor by providing the mechanical energy that drives turbulence and mixing within the PBL. As wind blows over the surface, it creates shear forces that generate turbulence at the surface, mixing the overlying air and creating a layer of well-mixed air within the PBL [10], [16]. The strength of the turbulence and mixing depends on the wind speed and direction [22]. In addition to driving turbulence, wind also plays a role in transporting air pollutants within the PBL [22]. As the wind blows, it carries pollutants along with it, creating concentration gradients and altering the chemical composition of the air [22], [24]. The interaction between wind and solar radiation also plays a role in the PBL dynamics. For example, daytime solar radiation creates convective motions that mix the air within the PBL, strengthening the wind and improving the

air mixing capability horizontally [32], [33]. At night, when solar radiation decreases, wind can still transport pollutants and well-mixed air, but the PBL can become shallower and more stable due to the absence of convective mixing, weakening the winds in the process [5], [9], [34], [35].

Atmospheric stability is another important factor that influences PBL dynamics. When the atmosphere is stable, the air near the surface is cooler and denser than the overlying air, which creates a stable layer of air that can act as a lid on the PBL [26], [32], [36]. This stability inhibits vertical mixing, and the PBL can become shallow and well-defined [34], [36]. In contrast, when the atmosphere is unstable, the air near the surface is warmer and less dense than the overlying air, which can lead to strong vertical mixing and the development of deep, well-mixed PBL [4], [36].

It's apparent that temperature is one of the most common parameters for determining atmospheric stability; however, it may not provide the most complete picture. Other factors such as humidity and wind can also influence the stability of the atmosphere. For example, high humidity can increase the stability of the atmosphere by reducing the vertical mixing of the air [27], [37]. Wind can also influence atmospheric stability by generating turbulence and mixing the air [22], [24].

Methods used to measure such variables useful in determining the PBL dynamics will be presented in the *Methods and Discussion* section.

### D. Role of PBL in Weather and Climate

It should not come as a surprise that the PBL has a role in predicting and managing weather and climate-related impacts. Since the PBL plays a crucial role in regulating temperature, mediating moisture exchange, influencing wind patterns, and shaping air quality, it is reasonable to expect that modeling these variations can lead to more accurate diagnoses of the spatial and temporal developments in the atmosphere.

For example, the PBL can influence surface temperature by regulating the exchange of heat between the surface and the overlying air [25], [38]. During the day, the sun heats the surface, creating a temperature gradient between the



surface and the overlying air [39]. The PBL helps mix this warm air with the cooler overlying air, moderating the temperature near the surface [39]. This process is particularly important in urban areas, where the built environment can create a warmer microclimate, known as the urban heat island effect [22], [23]. At night, the PBL can trap the cooler air near the surface, creating a stable layer that can inhibit vertical mixing. This can lead to the development of temperature inversions, where the air near the surface is cooler than the overlying air. Temperature inversions can occur during clear, calm nights and can lead to the accumulation of air pollutants near the surface [24], [37], [40].

The PBL also plays an important role in mediating the exchange of moisture between the Earth's surface and the overlying atmosphere. Water vapor evaporates from the Earth's surface and enters the PBL, where it can be transported and mixed with the overlying air [39]. This process can influence the formation of clouds and precipitation, which can affect weather and climate [20], [25], [38]. The height of the PBL can also vary depending on the moisture content of the air. In humid conditions, the PBL can be deeper, while in dry conditions, it can be shallower [22], [36]. This can affect the transport and mixing of air pollutants within the PBL [23]. The PBL can influence wind patterns and atmospheric circulation in several ways. As wind blows over the surface, it generates shear forces that create turbulence and mixing within the PBL [18], [26], [39]. This mixing can affect the speed and direction of the wind, which can influence atmospheric circulation and weather patterns [20], [25], [41]. The depth of the PBL can also vary depending on the strength of the wind. In calm conditions, the PBL can be shallow, while in windy conditions, it can be deeper, affecting the mixing properties within the PBL and their transport downwind [26], [32].

The PBL plays an important role in air quality by mediating the transport and dispersion of air pollutants. As the wind blows, it can carry pollutants within the PBL, where they can be mixed and transported horizontally [26]. The depth of the PBL and the strength of the mixing

can affect the concentration and dispersion of pollutants. In urban areas (where air pollution is a major concern), the PBL can play a critical role in determining the distribution and concentration of pollutants within the city [22], [26], [31].

In addition to these roles, the PBL can also have significant impacts on weather and climate-related events. For example, thunderstorms are often initiated by the interaction between the PBL and the overlying atmosphere [25], [38]. The PBL can also influence the formation and dissipation of fog, which can affect transportation and aviation [25], [38].

#### *E. Impact of Human Activities*

We have seen how air quality, temperature, and moisture levels alter the PBL structurally and dynamically. Industrial activities, transportation, and agriculture can also significantly impact the PBL, altering its composition and function. This section intends on exploring the impacts of human activities on the PBL through anthropogenic influences on temperature, stability and composition in several ways ([see Figure 3](#)).

Urbanization is one of the more significant human activities that can impact the PBL [23], [36]. The growth of cities has led to the expansion of impervious surfaces such as roads, buildings, and parking lots, which alter the surface energy balance through changing surface albedo<sup>3</sup>, and the amount of heat absorbed by the surface [23]. Leading to urban heat islands, this effect is caused by the absorption of solar radiation by surfaces with low albedo, which are prevalent in urban areas [26], [31], [38]. This absorbed energy is then released back into the atmosphere, which can lead to the formation of warmer and more unstable air masses [26]. The result of this is that urban areas often have higher temperatures and more turbulent air than surrounding rural areas [22], [31].

Agriculture can impact the PBL in several ways, including through emissions of greenhouse gases and air pollutants, changes in land use and albedo, and modification of surface moisture and energy balance.

---

<sup>3</sup> Albedo is a measurement of surface reflectivity [23]. Low albedo corresponds to a darker surface (lower reflectivity) and high albedo corresponds to a lighter surface (higher reflectivity). Examples of low albedo in urban environments include asphalt and concrete [23].



Agricultural activities often involve changes in land use, such as conversion of forests to croplands or pastures. This can alter the reflectivity of the Earth's surface, known as albedo, and lead to changes in the amount of solar radiation absorbed or reflected by the surface [26]. For example, conversion of forests to croplands or pastures can decrease albedo, leading to increased absorption of solar radiation and higher temperatures in the PBL [32].

Surface moisture and energy balance are also affected by irrigation, tillage, and other practices. Irrigation can increase surface moisture, leading to increased evapotranspiration and cooling of the PBL [22], [36]. However, excessive irrigation can also lead to waterlogging and increased soil moisture, which can reduce evapotranspiration and increase humidity in the PBL [22], [24].

Tillage practices can also impact the surface energy balance by altering the amount of energy reflected or absorbed by the surface. For example, tillage can increase the roughness of the surface, leading to increased scattering and reflection of solar radiation, which can contribute to cooling of the PBL [22], [25], [40]. Fertilizers, pesticides, and other chemicals can also impact the PBL. When released into the atmosphere, they can be carried by wind and air currents, contributing to the formation of smog and haze [22]. Mixing of such chemicals can also generate secondary pollutants such as nitric acid, particulate matter, and ozone<sup>4</sup> [22], [23], [26], [31]. As these pollutants can absorb or scatter solar radiation, they can reduce the amount of solar radiation that reaches the ground, which can reduce the amount of heating and cooling that occurs during the day and night, respectively [4], [26], [37]. This can diminish temperature and moisture gradients that drive turbulent vertical mixing, leading to a more stable PBL and ultimately pollutant trapping near the surface [26].

Energy production is another human activity that has a significant impact on the PBL. The burning of fossil fuels for energy production releases greenhouse gases such as carbon dioxide and methane, which can contribute to global warming and alter the climate [17], [37], [39].

This warming effect can alter the temperature gradient in the PBL, leading to changes in atmospheric stability and turbulence [11], [37], [42]. The increased concentration of greenhouse gases can also lead to changes in the chemical composition of the atmosphere, affecting the reactions that take place within it [26], [32], [36]. Transportation is another human activity that can have significant impacts on the PBL. The combustion of fossil fuels in cars, trucks, and airplanes releases pollutants into the atmosphere, contributing to air pollution and climate change [39]. These pollutants can include nitrogen oxides, particulate matter, and volatile organic compounds, all of which can affect the stability of the PBL [22]. The transportation sector can also lead to the formation of localized air pollution hotspots, which can impact the health of nearby communities and the stability of the PBL [8], [31].

Finally, industrial activities also contribute to the alteration of the PBL. The production of goods and services often involves the release of pollutants into the atmosphere, including particulate matter, sulfur dioxide, and nitrogen oxides [31], [39]. These pollutants can affect the chemical composition of the atmosphere, leading to changes in the reactions that take place within it. Industrial activities can also contribute to the formation of localized air pollution hotspots, which can impact the health of nearby communities and the stability of the PBL [8], [22], [26], [31].

### III. METHODS AND DISCUSSION

The development of methods for measuring the planetary boundary layer (PBL) height has evolved over time, driven by a combination of technological advancements, scientific discoveries, and practical applications. Early efforts to measure the PBL height relied on radiosonde measurements, which were first used in the 1920s to track changes in temperature and humidity with height in the atmosphere [18]. Later in the 1960s, researchers began to develop new techniques for measuring the PBL height, such as lidar and ceilometers [19]. In the 1980s

---

<sup>4</sup> Ozone is known to cause a variety of respiratory problems in humans when exposed to high levels, which can lead to asthma and bronchitis [21]. Ozone also damages vegetation by reducing their ability to absorb CO<sub>2</sub> through photosynthesis [21].



and 1990s, researchers continued to refine and improve these methods, developing new techniques in modeling and instrumentation (such as radiometers and Doppler radar) that could further capitalize on identifying characteristics that were previously proven as fundamental when determining PBL height [18], [19].

Today, researchers continue to develop new methods and improve existing ones for measuring the PBL height, driven by the need to better understand atmospheric dynamics, improve weather forecasting, and address air pollution and climate change. While each method is robust in ability, its usefulness depends on various factors such as cost, accuracy, and availability of equipment. In this section, we review several methods of choice used in measuring PBL height, discussing their respective strengths and weaknesses by examining their techniques and comparisons.

#### A. Radiosonde Measurements

Radiosondes are small, lightweight instruments that are attached to balloons and launched into the atmosphere. As the weather balloon ascends, the radiosonde measures atmospheric variables at various altitudes, transmitting the data back to a ground-based receiver. The data is then used to construct a vertical profile of atmospheric variables, which can be used to determine the height of the PBL.

A key variable measured by radiosondes is the vertical profile of temperature (see Figure 4) [24]. During the day, the surface of the Earth heats up, causing the air in the PBL to warm and rise. This creates a temperature inversion above the PBL, where the temperature suddenly stops increasing with height. The height of this inversion is a good estimate of the height of the PBL, as it represents the boundary between the well-mixed air of the PBL and the relatively stagnant air above it [11], [24], [37].

Radiosondes are particularly useful for measuring temperature inversions, as they can provide a detailed vertical profile of

temperature that can be used to identify the height of the inversion [11].

In addition to temperature, radiosonde measurements of humidity and pressure can also be used to estimate the height of the PBL. For example, the height of the PBL can be estimated by identifying the altitude where the humidity suddenly decreases, as this marks the boundary between the moist, well-mixed air of the PBL and the drier, less-mixed air above it [24].

Overall, radiosonde measurements are an important tool for measuring the height of the PBL, as they provide direct measurements of atmospheric variables that can be used to estimate the height of the boundary layer. These measurements are essential for understanding the dynamics of the PBL, and for developing accurate models of atmospheric transport and air quality [37].

We begin exploring several methods that are commonly utilized when analyzing radiosonde-sounding data.

##### a. Richardson Number Method

The Richardson Number ( $Ri$ ) is a dimensionless parameter that describes the relative importance of the buoyancy force to the shear force in the atmosphere. It is defined as the ratio of the potential energy associated with vertical stratification to the kinetic energy associated with wind shear [11]. We can express this ratio mathematically as

$$Ri = \frac{\left(\frac{g}{\theta}\right) \times \frac{\Delta\theta}{\Delta z}}{\left(\frac{\Delta u}{\Delta z}\right)^2}$$

where  $g$  is the acceleration due to gravity,  $\theta$  is the potential temperature<sup>5</sup>,  $\frac{\Delta\theta}{\Delta z}$  is the vertical

gradient of potential temperature, and  $\frac{\Delta u}{\Delta z}$  is the vertical gradient of wind speed.

To estimate the height of the PBL, vertical

<sup>5</sup> Virtual potential temperature can be used in place of potential temperature to account for the effects of moisture. However, it is important to note that the use of virtual potential temperature may require different scaling factors or threshold values compared to using potential temperature, as the relationship between atmospheric stability and  $Ri$  can be affected by moisture content [43].

gradients of potential temperature and wind speed taken from radiosonde measurements are used to calculate  $Ri$  at different altitudes (see

Figure 1). When  $Ri$  is high ( $Ri > \frac{1}{4}$ ), stable

stratification is dominant and turbulent mixing is suppressed<sup>6</sup>. Conversely, when the Richardson Number is low ( $Ri < 0$ ), shear turbulence is dominant and mixing is enhanced<sup>7</sup>.

Between  $0 \leq Ri \leq \frac{1}{4}$ , the buoyancy force

associated with thermal mixing becomes strong enough to overcome the shear force, and turbulent mixing begins to dominate, causing the PBL to deepen<sup>8</sup> [43]. This threshold for determining PBL height is known as the critical Richardson Number ( $Ri_c$ ) [43], [44].

Researchers use various techniques to identify the height at which the critical Richardson Number is reached, such as plotting the Richardson Number as a function of altitude and identifying the point at which the curve crosses the critical threshold (see Figure 5). An alternative form that uses specific altitudinal differences in wind speed and direction rather than total column vertical gradients of temperature and wind speed to estimate atmospheric stability is discussed next.

#### b. Bulk Richardson Number Method

The Bulk Richardson Number Method ( $Ri_B$ ) is a modification of the Richardson Number Method by additionally considering surface friction velocity, accounting for the surface influence on the PBL height [11], [43]. We can express this relationship mathematically as

$$Ri_B = \frac{g}{\theta} \times \frac{\Delta\theta}{\Delta z} \times \frac{\Delta z}{(\Delta\bar{U})^2} = \frac{g}{\theta} \frac{\Delta\theta\Delta z}{(\Delta\bar{u}^2 + \Delta\bar{v}^2)}$$

where  $g$  is the acceleration due to gravity,  $\theta$  is the potential temperature of the profile,

$\frac{\Delta\theta}{\Delta z}$  is the vertical gradient of potential temperature and

$$\Delta\bar{U} = \left( \frac{\partial\bar{u}}{\partial z} \right) + \left( \frac{\partial\bar{v}}{\partial z} \right)$$

is the mean wind speed difference between some arbitrary  $\Delta z$  altitudinal difference.

Like  $Ri$ , the PBL height can be estimated where the  $Ri_B$  falls below a critical value (typically  $\frac{1}{4}$ ).

An effective extension of the  $Ri_B$  method that includes a correction term to account for the effects of shear production and buoyancy flux is known as the Liu and Liang method ( $Ri_{BC}$ ) [4], [11]. Their method assumes that the PBL is well-mixed and that the vertical profile of virtual potential temperature is approximately constant within the PBL [4]. First calculating the  $Ri_B$  using the potential temperature and wind speed data, a correction term is applied to account for the effects of shear production and buoyancy flux at the top of the PBL.

The correction term in the Liu and Liang method can be expressed as

$$Ri_c = \frac{a}{\theta} \left( \frac{\partial\theta}{\partial z} \right) - \frac{b}{\bar{U}} \left( \frac{\partial\bar{U}}{\partial z} \right)$$

where  $\frac{\partial\bar{U}}{\partial z}$  is the vertical gradient of the mean

turbulent kinetic energy,

$\frac{\partial\theta}{\partial z}$  is the vertical gradient of potential

temperature, and the constants  $a$  and  $b$  are

empirical constants (typically set to  $\frac{1}{2}$  and  $\frac{1}{4}$

respectively). The corrected Bulk Richardson number ( $Ri_{BC}$ ) can then be calculated as

$$Ri_{BC} = Ri_B + Ri_c.$$

The PBL height is determined when the  $Ri_{BC}$  first exceeds a critical value, corresponding to the height at which the turbulence in the PBL is

<sup>6</sup> *I.e.*, if the fluid (air) is disturbed by a small vertical displacement, it will return to its initial configuration or harmonically oscillate about that dynamic state [43].

<sup>7</sup> These characteristics define the  $Ri$  convective instability threshold.

<sup>8</sup> This  $Ri$  interval between 0 and  $\frac{1}{4}$  defines the characteristics known as the  $Ri$  dynamic instability threshold [11], [43].

strong enough to overcome the effects of stable stratification (typically values that satisfy

$$0 \leq Ri_{BC} \leq \frac{1}{4}.$$

When validated using additional observations, the Liu and Liang method provides more accurate estimates of the PBL height than the  $Ri_B$  method alone, especially in cases where the PBL is shallow or the shear production and buoyancy flux effects are significant (see Figure 6) [4], [11]. However,  $Ri_{BC}$  assumes a horizontally homogenous atmosphere, which may not always be the case (e.g., particularly in complex terrain or near coastlines) [43]. Sensitivity to the empirical choice of  $Ri_B$  and the constants in  $Ri_C$  can also affect the accuracy of  $Ri_{BC}$ , since one parameter may not be optimal for all atmospheric conditions and locations [4], [43]. Yet as with any estimation technique, the Liu and Liang method should be used in combination with other methods and observations to ensure the reliability of results.

### c. Gradient Method

The Gradient Method assumes that the atmosphere within the PBL is well-mixed, with little variation in the thermodynamic variable of interest [45]. As air rises out of the PBL, it encounters a stable layer where the vertical gradient of the thermodynamic variable increases. The height of this stable layer, identified by a significant change in the gradient, is assumed to be the top of the PBL (see Figure 7).

The vertical gradient of the thermodynamic variable can be calculated using a numerical derivative or other mathematical technique. For example, the gradient of potential temperature<sup>9</sup> can be approximated by

$$\frac{\partial \theta}{\partial z} \cong \frac{\Delta \theta}{\Delta z}$$

where  $\theta$  is the potential temperature, and  $z$  is the height.

The gradient method assumes that the vertical gradient of the thermodynamic variable is a good indicator of the top of the PBL. It could therefore miscalculate PBL height in cases where the atmosphere is not well-mixed (or where other factors are important, such as wind shear or turbulence) [45].

For example, consider the profiles of temperature, pressure and potential temperature (e.g., thermodynamic variable of interest) on a SKEW-T log-P diagram. The height at which the gradient changes significantly is estimated to be the PBL height, which can be identified visually or by using an algorithm to search for a threshold change in the gradient. Such a threshold value is usually parameterized as 1K/100 m. This means that if the vertical gradient of potential temperature exceeds 1K/100 m for a certain height range, this height range is assumed to be outside the PBL. If inversions exist inside the PBL, this could reverse vertical gradients of potential temperature within the boundary layer, making it difficult to accurately identify the PBL height correctly [27].

Another approach is to use a threshold value for the gradient of the thermodynamic variable that is based on the variability of the variable within the PBL. This can be determined by analyzing data from multiple soundings and calculating the standard deviation of the thermodynamic variable within the PBL.

### d. Parcel Theory Method

The parcel theory method is another widely used radiosonde-based technique for measuring PBL height. Based on the concept of a "parcel" of air lifted from the surface, parcel theory involves using radiosonde data to determine the temperature and humidity of the lifted parcel, which is then used to estimate the height of the PBL [46], [47].

Once key meteorological parameters (temperature, pressure and humidity as a function of height) are obtained from the radiosonde, the lifting condensation level (

<sup>9</sup> Another commonly used thermodynamic variable is virtual potential temperature, which considers the effects of moisture on atmospheric stability [11]. The gradient of virtual potential temperature can be calculated using in the

same manner:  $\frac{\partial \theta_v}{\partial z} \cong \frac{\Delta \theta_v}{\Delta z}$ , where  $\theta_v$  is the virtual potential temperature.

$LCL$ ) can be calculated from the parcel's temperature and dew point temperature. This can be calculated from the following:

$$LCL = \frac{T - T_{dew}}{\Gamma_d + \frac{1}{2}\Gamma_m}$$

where  $T$  is the temperature,  $T_{dew}$  is the dew point temperature,  $\Gamma_d$  is the dry adiabatic lapse rate and  $\Gamma_m$  is the moist adiabatic lapse rate.

The PBL height therefore would be simply represented by

$$PBL_{Top} = LCL + z_{station}$$

where  $z_{station}$  is the height of where the radiosonde was launched (e.g., surface station). The parcel theory method has some advantages, including its simplicity and ease of use. It is also able to estimate the height of the PBL even in unstable conditions where the entrainment zone method may not be accurate (see Figure 7) [46]. However, parcel theory assumes the lifted parcel rises adiabatically, leading to errors in estimations when calculated in the presence of convection or where lift is influenced by other atmospheric processes [46], [47]. An example can be that of night radiative cooling, which leads to a stable atmosphere and a decoupling between the surface layer and the overlying air. This can prevent the well-mixed conditions that are required for the parcel theory method to work effectively [46]. Overall, the parcel theory method is a relatively simple and easy-to-use technique that provides accurate and consistent estimates of the PBL height in a wide range of atmospheric conditions.

#### e. Mixed Layer Depth (MLD) Method

The mixing layer depth (MLD) method is another widely used approach for estimating PBL height from radiosonde data, involving the identification of a distinct change in the vertical profiles of meteorological parameters, indicating the top of the well-mixed layer [24], [48]. The equations used in the MLD method involve calculating the gradient Richardson number ( $Ri_g$ ) and the critical Richardson number ( $Ri_{crit}$ ), which are defined as follows:

$$Ri_{grad} = \left(\frac{g}{\theta}\right) \times \left(\frac{\Delta\theta}{\Delta z}\right) \times \left(\frac{\Delta z}{H}\right)^2$$

$$Ri_{crit} = \frac{1}{4}$$

$$H = (\Delta z) \times \left(\frac{Ri_{grad}}{Ri_{crit}}\right)^{-\frac{1}{2}}$$

where  $g$  is the acceleration due to gravity,

$\theta$  is the potential temperature,

$\frac{\Delta\theta}{\Delta z}$  is the vertical gradient of potential

temperature,  $\Delta z$  is the vertical distance between two levels, and  $H$  is the depth of the well-mixed layer.

The MLD method is known for its versatility, providing a simple approach to calculating PBL height while complementing other methods (such as parcel theory) through its ability to be applied to different meteorological parameters (e.g., temperature, humidity and wind speed) (see Figure 8) [24], [48], [49]. However, MLD is naturally sensitive to changes in its key meteorological parameters, which can affect the vertical profiles of meteorological parameters and the height of the well-mixed layer. As such, identifying the top of the well-mixed layer through identification of a distinct change in the vertical profiles of meteorological parameters can become uncertain when such influences prevail (e.g., there could be many distinct shifts vertically) [49].

The calculation of  $Ri_{grad}$  can also be affected by uncertainties in atmospheric conditions since radiosonde data collected at discrete locations creates varied empirical observations, which may not provide a representative sample of the entire PBL [24], [49].

Regardless, the MLD method is a useful tool in analyzing vertical profiles of key meteorological parameters, providing an estimate of mixing layer depth, a key parameter for understanding PBL dynamics.

#### f. Entrainment Zone Depth Method

The entrainment zone method is based on the concept that the PBL is characterized by a stable layer of air at the top, which is separated from the overlying free atmosphere by a transition

layer known as the entrainment zone [9], [50]. Characterized by a sharp increase in potential temperature and a decrease in humidity<sup>10</sup>, the PBL height can be estimated from the height of the top of the stable layer, which is called the capping inversion [9], [22], [48].

The entrainment zone method is based on the vertical distribution of potential temperature or potential temperature variance<sup>11</sup>, which can be calculated using the following relationships:

$$\frac{\Delta\theta}{\Delta z} = \frac{\theta_e - \theta_s}{z_e - z_s}$$

where  $\frac{\Delta\theta}{\Delta z}$  is the potential temperature gradient

(lapse rate),  $\theta_e(z_e)$  is the potential temperature (height) at the top of the entrainment zone, and  $\theta_s(z_s)$  is the potential temperature (height) at the top of the stable boundary layer.

The entrainment zone depth can be calculated similarly, represented by

$$\Delta z_d = \frac{\theta_s - \theta_{sfc}}{\Delta\theta}$$

where  $\theta_{sfc}$  is the potential temperature at the surface.

The PBL depth would then be measured as

$$PBL_H = z_e + \Delta z_d$$

The entrainment zone method is a relatively simple and easy-to-use technique for measuring the PBL height from radiosonde data, not requiring specialized equipment or complex analysis techniques. It is also relatively robust and has been shown to provide accurate and consistent estimates of the PBL height in a wide range of atmospheric conditions (see Figure 9) [48], [50]. Yet because of these assumptions about the entrainment zone (e.g., being well-defined, characterized by a sharp increase in potential temperature, exhibits a decrease in humidity), cases where clouds or pollution<sup>12</sup> are present can alter PBL height calculations given

their temperature and humidity dependencies [22], [23]. Second, the method assumes that the PBL is well-mixed, which may not always be the case diurnally [11]. Yet even with these shortcomings, it is a relatively simple and easy-to-use technique that provides accurate and consistent estimates of the PBL height in a wide range of atmospheric conditions.

#### g. Wavelet Covariance Transform Method

The Wavelet Covariance Transform (WCT) method is based on the wavelet transform, which decomposes a time series signal into different frequency components by calculating covariance matrices of atmospheric variables at different heights [45]. Advantageous in its ability to provide both time and frequency localization, it is well-suited for analyzing atmospheric data with a high vertical resolution [7], [30], [45]. Once radiosonde data is retrieved, a wavelet transform is performed on the data, decomposing it into different frequency components. Such a function is usually in the form of the continuous wavelet transform (CWT), represented by

$$CWT(a, b) = \int [f(t) \cdot \psi(a, b)] dt$$

where  $f(t)$  is the atmospheric variable (e.g., temperature, humidity, or pressure), with  $a$  and  $b$  are scale translation parameters, respectively. Once the wavelet coefficients are obtained from the wavelet transform, the wavelet covariance transform (WCT) can be calculated as

$$WCT(i, j) = \frac{1}{N} \sum_{n=1}^N (W(i, n) - M(i)) \times (W(j, n) - M(j))$$

where  $W(i, n)$  and  $W(j, n)$  are the wavelet coefficients of the operated atmospheric variables at heights  $i$  and  $j$ ,

$N$  is the total number of wavelet coefficients, and  $M(i)$  and  $M(j)$  are the mean values of the wavelet coefficients at corresponding heights  $i$  and  $j$ , respectively.

Once the transform is calculated, thresholding

<sup>10</sup> This distinct characteristic in the vertical profile is due to the mixing of dry air from the free atmosphere into the moist air of the PBL [47].

<sup>11</sup> The potential temperature is defined as the temperature that a parcel of air would have if it were moved adiabatically to a reference pressure level [4].

<sup>12</sup> By absorbing or reflecting incoming solar radiation, depths where aerosols or clouds are present in the PBL can alter vertical temperature and air density profiles, impacting the height of the inversion layer and entrainment zone depth [22], [23].



the WCT matrix can take place. The threshold value is usually chosen as a fraction of the maximum covariance value in the matrix, where the PBL height is identified to be the height where the WCT matrix first exceeds the threshold value [45], [51]. The specific value used may vary depending on the study and the atmospheric conditions being analyzed; but in general, threshold values between 0.3 and 0.5 have been used in the literature [30]. The choice of threshold value can have an impact on the accuracy of the PBL height estimation, so it is important to carefully evaluate the results using other independent measurements ([see Figure 10](#)) [30], [45], [52].

The WCT method has several advantages over other methods for estimating the PBL height, particularly its ability to capture fine-scale vertical structures of the atmosphere [30]. And because of this high vertical resolution, detailed analysis of atmospheric variables at different heights is computationally efficient and can be applied to large datasets [30], [45].

However, the WCT relies on the assumption that the atmospheric variables are locally stationary, which may not be valid under certain conditions (such as in the presence of strong synoptic-scale variability) [45]. Additionally, the method is sensitive to the choice of wavelet function and threshold value, which may affect the accuracy of the PBL height estimation [45].

The WCT method is a powerful tool for estimating the PBL height from radiosonde data, with abilities to capture fine-scale vertical structures of the atmosphere at high computational efficiencies making it a valuable method for atmospheric research and applications [30], [45], [51].

### B. Radar/Lidar Measurements

Radar and lidar are remote sensing instruments that use electromagnetic radiation to measure the height and structure of the atmosphere.

*RADAR* (or *RA*dio *DE*tectioN *ANd* *RA*nging) uses radio waves to detect the location, velocity, and other properties of objects in the atmosphere.

Doppler radar can be used to measure the vertical velocity of air particles in the PBL, which can help to identify the top of the PBL. The height of the PBL can also be estimated by measuring the reflectivity of the atmosphere and identifying the height at which the reflectivity abruptly decreases [9], [35].

*LIDAR* (or *LI*ght *DE*tectioN *ANd* *RA*nging) uses lasers to measure the height and structure of the atmosphere, providing high-resolution measurements of the PBL height and structure by detecting the backscattered light from aerosols and other atmospheric particles [6], [9]. This backscattered light can be used to estimate the vertical profile of aerosol concentration in the atmosphere, which can help to identify the top of the PBL [53]. Additionally, lidar can be used to estimate the temperature and humidity profiles of the atmosphere, which can provide information about the stability of the PBL [53].

Both radar and lidar are valuable tools for measuring the PBL height, as they can provide detailed vertical information about the structure and dynamics of the PBL. However, they also have some limitations<sup>13</sup>. For example, radar can be affected by attenuation due to precipitation or other sources of moisture, limiting its ability to detect the PBL height [53], [54]. Lidar can also be affected by attenuation and scattering from clouds and other atmospheric particles, making it difficult to accurately measure the PBL height under certain conditions [53], [54]. Overall, radar and lidar are powerful tools for measuring the PBL height, but they are often used in conjunction with other methods, such as the WCT method from radiosonde data, to provide a more comprehensive understanding of the PBL dynamics and structure [10], [53]. We explore several methods using radar/lidar and their roles in measuring PBL height.

#### a. Raman Lidar

The Raman Lidar method is one of the most effective techniques for measuring PBL height with high accuracy and precision. Based on the

---

<sup>13</sup> Clouds and precipitation can affect the accuracy of lidar measurements in multiple ways, such as attenuation, multiple scattering, signal noise, and false targets [10]. The laser beam can be absorbed or scattered by clouds and precipitation, reducing its intensity and making it difficult to accurately measure the height and properties of atmospheric particles [10]. Moreover, precipitation particles can create noise in lidar signals, which can lead to errors in the measured particle properties and contribute to uncertainties in the lidar data [52], [53].

Raman scattering effect<sup>14</sup>, portions of transmitted laser light scatters from interactions with nitrogen ( $N_2$ ), oxygen and water vapor molecules ( $\nu$ ), shifting the wavelength of the scattered light [11], [55]. This shift in wavelength (refractive index) can be used to measure atmospheric temperature and composition at different altitudes, which can be applied at measuring the PBL depth [10], [55]. Using the Raman Lidar method is straightforward. Once the backscattering signal has been recorded from the laser pulses, the signal relation to temperature and composition can be measured from evaluating the following:

$$I(z) = \frac{P(z) \cdot \sigma(z) \cdot \eta(z) \cdot [1 - e^{-2\alpha(z) \cdot L}]}{2 \cdot \alpha(z)}$$

where  $I(z)$  is the backscattering signal at range  $z$ ,  $P(z)$  is the laser power at range  $z$ ,  $\sigma(z)$  is the molecular scattering cross-section at range  $z$ ,  $\eta(z)$  is the Raman scattering efficiency at range  $z$ ,  $\alpha(z)$  is the atmospheric extinction coefficient at range  $z$ , and  $L$  is the length of the lidar pulse.

The changes in temperature and backscatter signals with range can be then measured as

$$\frac{I_\nu(z)}{I_{N_2}(z)} = \frac{Q_\nu}{Q_{N_2}} \cdot e^{\frac{-h\nu + h_{N_2}}{k_B \cdot T(z)}}$$

where  $I_\nu(z)$  is the Raman scattering signal from water vapor at range  $z$ ,  $I_{N_2}(z)$  is the molecular scattering signal from nitrogen at range  $z$ ,  $Q_\nu$  and  $Q_{N_2}$  are the Raman scattering efficiencies,  $h\nu$  and  $h_{N_2}$  are the Raman signal energies,  $k_B$  is the Boltzmann constant and  $T(z)$  is the atmospheric temperature at range  $z$ . The left-hand side (LHS) of the equation is related to the refractive index of the atmosphere. By

measuring the ratio  $\frac{I_\nu(z)}{I_{N_2}(z)}$  at different ranges,

we can infer the atmospheric temperature from water vapor and nitrogen molecules, which in turn can be used to calculate the atmospheric lapse rate:

$$\frac{\partial T(z)}{\partial z} = \frac{\Delta T(z)}{\Delta z} = \gamma$$

where  $\Delta T(z)$  is the change in temperature with range  $z$ ,  $\Delta z$  is the range interval and  $\gamma$  is the atmospheric lapse rate.

Determining the vertical threshold where the lapse rate changes abruptly ( $\lim_{\frac{\partial T(z)}{\partial z} \rightarrow 0}$ )

determines the PBL height:

$$PBL_H = \frac{T(z_{top}) - T_{sfc}}{\gamma}$$

From a rigor perspective, the Raman Lidar method is capable of high accuracy and precision, typically with a spatial and temporal error of 50 meters or less and 1 hour (see [Figure 11](#)) [10], [11], [55]. It is also capable of multi-parameter observations, providing information on atmospheric temperature, water vapor concentration, and aerosol properties [55]. But with such effectiveness and rigor comes at cost and complexity, with Raman systems requiring skilled operators to operate and maintain the instruments [10]. Clear sky conditions are also necessary for this method to work, as clouds, precipitation and high aerosol concentrations can obscure the lidar beam and interfere with the Raman scattering signals, lowering the signal-to-noise ratio (SNR) and reducing accuracy and precision of the measurements [10], [11], [55]. If other methods are used to compensate for non-optimal periods in the lidar scanning, the Raman Lidar method would remain an overall powerful technique for measuring PBL height with high-resolution observations with high accuracy and precision

<sup>14</sup> The Raman scattering effect is a physical phenomenon in which light interacts with matter and changes its wavelength and energy [11], [55]. Specifically, when a photon of light interacts with a molecule, it can transfer energy to the molecule, causing it to vibrate. This vibration results in a small shift in the energy of the scattered photon, known as the Raman shift [54]. The Raman shift can be used to identify the molecular species present in a sample and to determine their concentration and temperature [54]. This effect is named after the Indian physicist C.V. Raman, who discovered it in 1928 and was awarded the Nobel Prize in Physics in 1930 for his work [11]. The Raman scattering effect has numerous applications in fields such as materials science, chemistry, and biology, as well as in atmospheric and environmental research, where it is used in the Raman Lidar method to measure the height of the PBL [11].



[10], [11], [55].

*b. Coherent Doppler Lidar*

Coherent Doppler Lidar (CDL) is a remote sensing technique that uses laser light to remotely sense atmospheric parameters such as wind velocity and direction. This method utilizes the Doppler effect<sup>15</sup> to determine the velocity of the scattering particles in the atmosphere, inferring PBL height from backscatter analysis [57]. CDL works by transmitting laser pulses into the atmosphere and receiving the backscattered light. The frequency of the transmitted laser pulse is shifted due to the Doppler effect when it interacts with the scattering particles in the atmosphere. By measuring the frequency shift, the wind velocity in the atmosphere can be determined and subsequently the PBL height from the change in the wind velocity profile as a function of height [56], [57].

The frequency shift data is analyzed using the following relationship:

$$\frac{\Delta f}{f} = -2 \frac{v_{scatter}}{c}$$

where  $\Delta f$  is the frequency shift,  $f$  is the transmitted frequency,  $v_{scatter}$  is the velocity of the scattering particles, and  $c$  is the speed of light. Note that solving for  $v_{scatter}$  can determine wind velocity from the frequency shift.

As a functioning lidar, the CDL offers high vertical and temporal resolution, providing information on wind direction and speed in the atmosphere (see Figure 12) [56]. However, it is an expensive method that requires specialized training and is limited in spatial range [56]. It is also affected by atmospheric conditions (such as clouds and precipitation), which can reduce its accuracy and precision [56], [57].

*c. Radio Acoustic Sounding System (RASS)*

The Radio Acoustic Sounding System (RASS) method is another remote sensing technique that involves inferring the height of the PBL from measuring and analyzing the speed of sound.

RASS uses a combination of radio waves and acoustic waves to probe the atmosphere and measure the temperature profile, based on the principle that the speed of sound is dependent on the temperature of the medium through which it travels [58], [59]. By transmitting an acoustic signal vertically and receiving the return signal, the RASS system can measure the time delay between the transmitted and received signals. This time delay can be converted into a temperature measurement, which is used to calculate the speed of sound [59], [60].

The techniques involved in using RASS constitute of radio frequency (RF) transmissions, pulsed into the atmosphere at typically 54.1 MHz [58]. These RF pulses travel upward into the atmosphere until they encounter a temperature inversion layer, which typically marks the top of the PBL. Once encountering the inversion, the pulses are scattered back towards the ground where a receiver detects the scattered RF pulses and measures the time it takes for them to travel back to the ground. This travel time is then used to calculate the height of the temperature inversion layer, and thus the height of the PBL [58]–[60]. The RASS method also employs an acoustic wave component, which is used to measure the temperature profile of the PBL [58]. The acoustic wave is generated by a loudspeaker on the ground, which sends a series of sound pulses upward into the atmosphere. As the acoustic wave travels upward, it is refracted by the temperature gradient, causing it to bend back toward the ground. The RASS receiver detects the scattered acoustic waves and measures the time it takes for them to travel back to the ground, subsequently calculating the PBL temperature profile from this time travel [58]–[60].

To measure PBL height from RASS backscattering, the speed of sound at the surface ( $c_s$ ) is first calculated using surface temperature ( $T_{sfc}$ ), pressure and the ratio of specific heats ( $\lambda$ ):

$$c_s = (\lambda \cdot R \cdot T_{sfc})^{0.5}$$

where  $R$  is the specific gas constant and

<sup>15</sup> The Doppler effect is a phenomenon that occurs when there is relative motion between a source of waves (such as sound or light) and an observer. The effect causes the frequency of the waves received by the observer to be shifted from the original frequency of the source [56].

$\lambda = \frac{c_p}{c_v}$  is the ratio of the heat capacities of a gas at constant pressure ( $c_p$ ) and constant volume ( $c_v$ ).

The virtual temperature as the surface ( $T_{v\_sfc}$ ) is then calculated:

$$T_{v\_sfc} = T_{sfc} \cdot \left[ 1 + \frac{0.61}{100} RH \right]$$

where  $RH$  is the relative humidity at the surface.

Altitude-dependent virtual temperature can then be approximated as

$$T_{v\_z} = T_{v\_sfc} + \frac{\Delta T_v}{\Delta z} (z - z_s)$$

where  $\Delta T_v$  is the change in virtual temperature with respect to height,  $\Delta z$  is the vertical resolution of the RASS (usually around 30 meters), and  $z (z_s)$  is the height above the surface (surface height), respectively. The gradient of  $T_{v\_z}$  is then taken to determine

where the gradient reaches a certain threshold,

or  $\frac{dT_{v\_z}}{dz} > 0.2 K^{-1} m^{-1}$ . When met, this

threshold is considered to be the PBL top [58], [60].

The RASS method offers several advantages for measuring PBL height. Firstly, it provides real-time measurements with high vertical and temporal resolution, which allows for a better understanding of the PBL dynamics (see Figure 13) [58]. RASS measurements are also not affected by atmospheric conditions such as humidity, which can be a limitation for other methods such as ceilometers [58]. Additionally, the RASS method can provide information on both the PBL height and temperature profile, which is useful for a variety of atmospheric studies [58], [59]. However, the RASS requires a high level of stability in the atmosphere, as even small fluctuations in temperature gradients can affect the accuracy of the measurements [58]. Additionally, the RASS system can be affected by wind turbulence, which can cause variations in the speed of sound measurements [58]. Another limitation is that the RASS method is dependent on the availability of a suitable acoustic source, and it may not be

feasible to use in all locations [58]. This makes the RASS generally limited to measuring the PBL height during daytime hours, when the surface temperature is warmer than the air above, limiting its applicability for nocturnal PBL studies [58]–[60].

Regardless, the RASS method is a valuable technique for measuring PBL height, especially when used in conjunction with other methods. It provides a non-intrusive way to estimate the PBL height and can be used in a variety of weather conditions. The RASS method is relatively easy to operate and provides real-time data. Despite its limitations, such as sensitivity to temperature gradients and potential signal contamination from nearby sources, the RASS method remains a popular and effective technique for measuring PBL height [58], [59]. Continued advancements in technology and data processing techniques are likely to improve the accuracy and reliability of the RASS method in the future, making it an even more useful tool for atmospheric researchers and forecasters.

#### d. Wind Profiling Radar

Wind profiling radar is a technique that uses radar technology to measure the atmosphere's vertical structure. The basic principle behind wind profiling radar is that it can measure the Doppler shift of radar signals scattered by atmospheric targets, such as turbulence or aerosols, to infer the velocity and direction of atmospheric winds at different altitudes [5], [50], [60].

The wind profiling radar operates by sending out a series of radar pulses into the atmosphere, measuring the Doppler shift of the scattered radar signals [54], [56]. When this Doppler shift is measured at different altitudes, the radial wind speed ( $v$ ) and direction ( $\theta$ ) can be inferred for each altitude using the following equations:

$$v = -\frac{\lambda \cdot f \cdot D}{2 \cdot \Delta f \cdot \cos(\theta)}$$

$$\theta = \tan^{-1} \left[ \frac{\Delta f}{f} \cdot \tan(\theta_0) \right]$$

$$\frac{\Delta f}{f} = -2 \frac{v_{scatter}}{c}$$

where  $\lambda$  is the radar signal wavelength,  $D$  is the

antenna diameter,  $\Delta f$  is the frequency shift,  $f$  is the transmitted frequency,  $v_{scatter}$  is the velocity of the scattering particles, and  $c$  is the speed of light and  $\theta_0$  is the angle between the radar beam and the horizontal.

The PBL height can then be estimated from the vertical profile of the wind speed or other atmospheric parameters, such as the vertical gradient of refractive index (e.g., the difference in radial wind speed between two altitudes divided by the difference in altitude):

$$\frac{\partial v}{\partial z} = \frac{v(z+h) - v(z)}{h}$$

where  $h$  is the height resolution of the radar data retrieved. The height at which the vertical gradient of the radial wind speed starts to decrease rapidly or become constant is the estimated height of the PBL top [7], [52], [53]. The wind profiler method offers several advantages for measuring PBL height, the primary being that it can provide continuous and real-time measurements of the vertical wind profile, allowing for the determination of PBL height in near-real-time, which is important for air quality management and weather forecasting [7], [10], [45]. Another advantage is that it can measure the vertical wind profile up to several kilometers, providing a more comprehensive view of the atmosphere compared to other methods (see Figure 14) [7], [45]. However, the accuracy of wind profilers can be affected by the presence of strong winds or turbulence in the lower atmosphere, causing fluctuations in the vertical wind profile measurements [7]. Wind profilers also require the use of multiple wind profilers deployed over a large area to capture the spatial variability of the PBL height, which can be expensive and time-consuming [53]. Additionally, the wind speed gradient calculation relies on the assumption of hydrostatic equilibrium, which may not hold in cases of rapidly changing weather conditions or near the boundary layer [56], [57]. This can also occur in cases of weak vertical wind shear, which affects the quality and accuracy of the signal-to-noise (SNR) analysis [53], [56]. Yet the profiler's ability to provide continuous measurements of wind speed and direction throughout the vertical column makes it an effective technique for detecting the boundary

layer height. With the availability of advanced technology, wind profilers have become more accurate and reliable over time [53], [54]. However, there are still some limitations, such as sensitivity to atmospheric conditions, that can affect the accuracy of measurements. Despite these limitations, the wind profiler remains an essential tool for studying the PBL and its interaction with the atmosphere [7], [45], [53], [61].

#### e. Ceilometer

Ceilometers are a type of remote sensing instrument used to measure the vertical distribution of aerosols and clouds in the atmosphere [62]. By emitting a laser or LED light beam to measure the intensity of the backscattered light, the PBL height can be estimated from the vertical profile of the backscatter intensity [63], [64]. When analyzing the data, a 'jump' in the backscatter signal is usually in indication of the PBL top, since sharp increases in aerosol concentration are common near the top of a temperature inversion (e.g., capping inversion) [64], [65]. Jumps in signal are usually identified after the backscattering profile has been smoothed to reduce noise and improve accuracy [65]. Filters (such as a moving average ( $\beta$ ) or Savitzky-Golay filter) are applied, using a similar method to the following:

$$\beta_{smooth(z)} = \frac{1}{N} \sum_{i=1}^N \beta \cdot (z - (i-1)\Delta z)$$

where  $N$  is the number of points in the filter window and  $\Delta z$  is the height resolution. Changes in the gradient of this new smoothed profile can be identified by taking  $\frac{d\beta}{dz}$  and

finding departures from 0. Since the possibility exists for critical variations in gradient departures, a common criterion for identifying the PBL layer is to select a threshold the gradient must exceed:

$$\frac{d\beta}{dz} > 2 \times 10^{-3} sr^{-1} m^{-1}$$

Once points that exceed this threshold are



accumulated, the maximum gradient<sup>16</sup> (e.g., inflection points) can be found by analyzing the backscattering profile slope:

$$\frac{d^2 \beta}{dz^2} = 0$$

The PBL height can then be inferred from the difference between the maximum gradient's altitudinal magnitude and the ground-level altitude:

$$PBL_H = z_g - z_{\frac{d^2 \beta}{dz^2}=0}$$

The ceilometer method offers several advantages for measuring the PBL height. First, it is a low-cost and relatively simple technique compared to other methods such as radiosonde or lidar, with similar abilities at measuring other atmospheric parameters (such as cloud base height and aerosol concentration) ([see Figure 15](#)) [63]–[65]. It can also provide continuous measurements of the PBL height with high temporal resolution, allowing for the detection of PBL height variations on shorter timescales [63]. Their ease of installation and maintenance also makes them suitable for long-term monitoring at a fixed location [63].

While the ceilometer method has many advantages, the dependence on backscattered light from clouds or aerosols can be affected by cloud cover anomalies or the absence of aerosols from their multiple scattering or partial absorption properties of signals [62], [63], [65]. Furthermore, interference from variables with larger cross sections than aerosols (e.g., rain, snow, vegetation, etc.) may interfere with the backscattered light signal, potentially affecting measurements [63], [65].

Yet despite these shortcomings, the advantages of the ceilometer method, such as its affordability, portability, and real-time data acquisition, make it an attractive option for many researchers and atmospheric scientists [62]. Furthermore, advancements in technology and calibration techniques have led to improvements in the accuracy and precision of ceilometer measurements [62]. With the growing importance of understanding the dynamics and effects of the PBL, ceilometers will likely continue to be a valuable tool in

atmospheric research and applications [62]–[65].

### C. Satellite Observations

Satellite observations have emerged as a useful tool in measuring PBL height due to their ability to provide near-global coverage and frequent measurements [66], [67]. Being either active remote sensing methods (e.g., lidar and radar) or passive remote sensing methods (e.g., radiometry), measurements from these methods can be used to estimate PBL height through the detection of atmospheric features such as aerosol layers, temperature inversions, and cloud bases [66], [67].

One of the major advantages of using satellite observations to measure PBL height is the ability to obtain data over remote or inaccessible regions, which would be difficult to obtain using ground-based methods ([see Figure 16](#)) [65]. Additionally, satellite observations provide continuous and frequent measurements, which can help capture diurnal and seasonal variability in PBL height [65]. Offering a promising approach to measuring PBL height on a global scale, ongoing efforts to improve satellite technology and data analysis techniques are expected to enhance the accuracy and reliability of these measurements in the future [66], [67]. We explore several methods using satellite observations and their roles in measuring PBL height.

#### a. Passive microwave radiometry

Passive microwave radiometry is a remote sensing technique that measures the natural microwave radiation emitted by the Earth's surface and atmosphere [49]. It has been used to estimate the height of the planetary boundary layer (PBL) through the ability to detect temperature inversion layers, which can be observed by measuring the brightness temperature of the atmosphere at different frequencies [49], [68]. At frequencies around 50 GHz, the brightness temperature is primarily determined by the temperature of the PBL [68]. At higher frequencies (e.g., 150 GHz), the

<sup>16</sup> A root-finding algorithm such as the Bisection method or the Newton-Raphson method is comparable to finding the maximum gradient [65].

brightness temperature is determined by the temperature of the atmosphere above the PBL [68]. The difference in brightness temperature between the two frequencies can be used to estimate the height of the temperature inversion layer and, thus, the height of the PBL [49], [68]. To calculate the brightness temperature difference ( $\Delta T_b$ ), the variance between two frequencies is calculated:

$$\Delta T_b = T_{b_h} - T_{b_l}$$

where  $T_{b_h}$  and  $T_{b_l}$  are the brightness temperature of the higher and lower frequencies, respectively.

Once the brightness temperature is found, the height of the temperature inversion ( $h_{inv}$ ) can be estimated by the following relationship:

$$h_{inv} = \frac{\lambda}{4\Delta T_b}$$

where  $\lambda$  is the wavelength of the microwave radiation.

The PBL height can then be inferred by taking the difference between the average height of the PBL (in km) and the temperature inversion height:

$$PBL_H = 5 - h_{inv}$$

The passive microwave radiometry method offers several advantages that are characteristic to other remote sensing techniques, including the ability to provide high vertical resolution measurements over a wide area without the need for in situ measurements (see Figure 17) [68]. It can also operate day and night and in most weather conditions, making it a reliable tool for PBL height estimation and allowing for more comprehensive and efficient monitoring of the PBL height [68]. But as a remote sensing instrument, it's higher sensitivity to changes in atmospheric temperature and water vapor content over changes in aerosol concentrations makes it less effective in regions where aerosols are a dominant factor in PBL dynamics [49], [68].

Yet the passive microwave radiometry method remains a promising technique for measuring PBL height given its advantages of being able to

measure PBL heights over large areas and have high temporal resolution, allowing for better understanding of the temporal and spatial dynamics of the PBL. While difficulties remain in its ability to separate the PBL signal from the surface and atmospheric effects (which can lead to uncertainties in PBL height estimation), with further research and development, passive microwave radiometry has the potential to become a valuable tool for PBL height measurements, particularly in remote and hard-to-reach areas where other methods are not feasible [49], [68].

### b. Infrared and visible imaging

Infrared and visible imaging is another remote sensing technique that uses satellite or ground-based cameras to capture images of the Earth's surface and atmosphere in the visible and infrared spectrum [69]–[71]. Temperature and humidity of the air in the PBL can affect the scattering and absorption of solar radiation, causing a change in the refractive index of the air. This change in the direction of light rays passing through the atmosphere can result in an observable visible and infrared gradient that can identify the capping inversion (related to PBL height) (see Figure 18) [69]–[71].

Common with other ground-based systems, changes in the temperature or moisture gradients are the preferred methods of identifying the PBL top:

$$\frac{\Delta T}{\Delta z} = \frac{T_2 - T_1}{z_2 - z_1}$$

$$\frac{\Delta M_c}{\Delta z} = \frac{q_2 - q_1}{z_2 - z_1}$$

where  $T$  is the temperature,  $\frac{\Delta M_c}{\Delta z}$  is the moisture gradient and  $q$  is the specific

humidity<sup>17</sup>. Departures from  $\frac{\Delta T}{\Delta z} = 0$  and

$\frac{\Delta M_c}{\Delta z} = 0$  can indicate the top of the PBL, yet

examining surrounding atmospheric conditions should be taken into account to confirm the PBL

<sup>17</sup> Machine learning techniques have also been used to evaluate PBL height through training a model on a set of labeled images to identify the PBL height and then using the trained model to automatically identify the PBL height in new images [69]–[71].



height (as stabilizing gradients could result from changes in atmospheric conditions, temporary lapses in data collection, or the occurrence of an inversion layer) [71].

As a remote sensing method, infrared and visible imaging provides high-resolution atmospheric images of weather conditions, allowing for a more detailed analysis of temporal and spatial variability [69], [71]. Yet these imaging platforms are also susceptible to the same shortcomings of other remote sensing techniques, such as being strongly dependent on the atmosphere being cloud-free and relatively unpolluted<sup>18</sup> [71].

To mitigate these limitations, other remote sensing techniques (e.g., LIDAR, radiosondes) can validate and improve the accuracy of these imaging techniques, making infrared and visible platforms increasingly popular in atmospheric research [69]. With continued advancements in technology and methods, infrared and visible imaging have the potential to provide valuable insights into the dynamics of the PBL and its interactions with the lower atmosphere [69], [71], [72].

### c. GPS occultation

GPS occultation is a remote sensing technique that utilizes signals from Global Positioning System (GPS) satellites to measure atmospheric properties. When GPS signals pass through the atmosphere, its path is bent due to the variations in refractive index caused by atmospheric changes in the temperature, pressure, and humidity [73]. This atmospheric refraction affects the time it takes for the GPS signal to travel from the satellite to the receiver on the ground, changing the signal's phase and amplitude as it travels through the atmosphere [73]. PBL height can be determined from GPS occultation data by analyzing the vertical gradient of refractivity in the lowest few kilometers of the atmosphere, which is indicative of the PBL height [73], [74].

The atmospheric refractivity ( $N$ ) is a function of height, or  $N(h)$ . The following equation can express the refractivity of the atmosphere at any height:

$$N(h) = N_o e^{\frac{-h}{H}}$$

where  $N_o$  is the surface refractivity,  $h$  is the height above the surface and  $H$  is the scale height of the atmosphere.

Changes in the refractivity profile ( $\frac{\partial N}{\partial h} = 0$ ) is

indicative of the PBL height [73].

While providing high-resolution spatial observations, the advantage of measuring the refractive index and bending angle of the atmosphere means GPS occultation is less susceptible to factors that can impact other techniques, such as the presence of clouds, precipitation, and aerosols [73], [74]. But as a GPS platform, a high level of signal quality and stability is necessary to prevent any disruptions or fluctuations in the signal. This means a clear line of sight between the GPS satellite and the receiver on the ground must be maintained, which can be difficult in areas near buildings, trees, and other obstacles [73]. The vertical resolution of GPS is also affected by the size of the Fresnel zone<sup>19</sup>, making it less suitable for studying smaller-scale atmospheric features at longer distances from the source [73], [74]. Compared to other remote sensing methods, GPS occultation has several advantages, including its ability to obtain vertical profiles of atmospheric parameters with high accuracy and low bias, its independence from ground-based observations, and its ability to provide near-global coverage (see Figure 19) [73]. GPS occultation is also less affected by atmospheric conditions, such as clouds and precipitation, making it suitable for use in a wide range of environments [73]. Despite its acceptable drawbacks, GPS occultation has shown promising results in various studies and is

<sup>18</sup> Cloud cover can limit the availability of radiation reaching the Earth's surface and can affect the accuracy of the temperature measurements, while atmospheric aerosols can cause scattering of the radiation, which can lead to errors in the temperature measurements.

<sup>19</sup> The Fresnel zone is an elliptical area around a direct line-of-sight signal transmission path that can be affected by obstacles or reflections, causing signal distortion [73]. The size of the Fresnel zone depends on the frequency of the signal and the distance of the transmission path [73]. GPS usually has a larger signal distortion than the typical vertical resolution of other remote sensing methods (such as radiosondes and lidar) [73].



becoming increasingly popular in atmospheric research with its growing potential to provide valuable insights into the dynamics of the atmosphere and its interactions with the Earth's surface [73], [74].

#### D. Numerical Modeling

Numerical modeling is the primary modern tool for characterizing atmospheric sensitivities and how they compare to observations<sup>20</sup> [4], [22], [34], but even the PBL cannot be explicitly represented by such techniques. This shortcoming is amended through using an algorithmic or statistical approach, characterized as a parameterization [10], [41]. It's these parameter schemes that are crucial to modeling how the PBL height (PBLH) changes with time, making it one of the most significant parameters in the fields of atmospheric science [34], [41], [75].

One of the key benefits of numerical modeling is its ability to simulate the behavior of the PBL under a wide range of conditions and scenarios using fluid dynamics, thermodynamics and atmospheric chemistry [41]. Models can also be used to simulate the impact of human activities on PBL dynamics, such as changes in land use, emissions from industrial activities, and the use of renewable energy sources [41], [76].

These impacts, however, are complex processes that drive PBL behavior. Considerations of atmospheric turbulence, convection, radiation, and chemical reactions can be difficult to accurately simulate given the computational power and sophisticated algorithms necessary for spatial and temporal scales [10], [41], [43]. Regardless, numerical models have proven to be highly effective tools for simulating the behavior of the atmosphere and predicting weather and climate patterns. Advances in computing power, observational data, and modeling techniques have led to significant improvements in the accuracy of numerical

models in recent years [41], [77].

To create improved algorithmic or statistical determinations of the PBL, many methods have been researched and developed. We examine 4 sub grid-scale parameterizations and how they influence the model's ability to represent PBL dynamics.

##### a. Large-eddy simulation (LES)

The Large Eddy Simulation (LES) is a powerful tool in numerical modeling that is increasingly used to simulate the PBL. This technique allows for a more accurate representation of turbulent flows at high Reynolds numbers than traditional modeling techniques such as the Reynolds-Averaged Navier-Stokes (RANS) equations [78], [79]. In the context of PBL height measurement, LES can be used to simulate the vertical profile of turbulent mixing and derive estimates of the PBL height, solving the governing equations of fluid motion at a high resolution and modeling the smaller turbulent structures that are responsible for mixing within the PBL [79], [80].

The LES method uses a grid system to divide the atmosphere into smaller cells, each representing a volume of air [81]. The equations of motion<sup>21</sup> are then solved for each cell, including turbulent motion of small-scale air molecules [79], [81].

One of the most significant advantages of LES is its ability to capture the dynamics of turbulent processes, capable of resolving turbulent eddies down to a certain scale and capturing the turbulent formation and evolution of eddies (see Figure 20) [41], [77]–[81]. LES is also computationally efficient compared to Direct Numerical Simulation (DNS), which resolves all scales of turbulence, making it possible to simulate large areas of the atmosphere for longer periods [41], [77], [78]. LES can also be applied to a wide range of

---

<sup>20</sup> Observations have a wide and varying network. Examples of the current observing network include *Temp* (shorthand for Radiosonde-based temperature soundings), *Pilot* (shorthand for Pilot Balloons), *Profiler* (shorthand for Wind Profilers), *Synop* (refers to surface synoptic observations), *Metar* (refers to Meteorological Terminal Air), *AMDAR* (refers to Aircraft Meteorological Data Relay), and *AMV* (Atmospheric Motion Vectors, from tracking clouds and moisture plumes seen by Geosynchronous Satellites) [22], [23].

<sup>21</sup> The basic equation of motion is the Navier-Stokes equation, which describes the conservation of momentum, mass, and energy [79], [81]. In addition, the equations of continuity and thermodynamics are used to describe the conservation of mass and energy [79], [81].



atmospheric phenomena, such as cloud formation, atmospheric boundary layers, and atmospheric chemistry, making it ideal for both micro- and mesoscale studies [41], [77]–[81]. An immediate disadvantage that arises is that LES requires high computational power. As computational cost is proportional to the number of grid points, LES simulations require supercomputers with significant computing power, limiting the range of applications for LES, particularly for large-scale simulations [41], [79].

Another disadvantage of LES is that it requires accurate boundary conditions and initial conditions [41], [77]. Inaccurate boundary conditions and initial conditions can significantly impact LES results, making it difficult to interpret the results [41], [77]. LES also requires accurate parameterization of unresolved scales, which presents significant challenges due to the complexity of atmospheric processes [41], [78].

Despite these limitations, LES has significant potential for future atmospheric research. With advancements in computing power and modeling techniques, LES can be applied to increasingly complex atmospheric phenomena, leading to improved understanding and forecasting of weather and climate [78], [79], [81]. Future research should focus on developing efficient algorithms and models, improving the accuracy of boundary and initial conditions, and developing accurate parameterizations of unresolved scales [41], [78]–[82].

### *b. Boundary layer parameterization*

Boundary layer parameterization (BLP) is a key aspect of atmospheric modeling that aims to capture the complex interactions between the lower atmosphere and the Earth's surface. BLP is the process of representing the exchange of heat, moisture, and momentum between the Earth's surface and the lower atmosphere in a numerical model [75], [83]. Given the PBL's turbulent flow regime, the non-linearity associated with these characteristics makes modeling PBL dynamics difficult to accurately capture in numerical models [38], [78].

As a result, boundary layer parameterization

schemes are used to approximate the behavior of the boundary layer in numerical models. These parameterization schemes use simplified equations that are derived from observations and theory to represent the dynamics of the boundary layer [38], [41], [75], [84], [85]. The most common approach to boundary layer parameterization is to divide the boundary layer into layers, and to apply a separate parameterization scheme to each layer [41]. The simplest scheme is the "surface layer" scheme, which describes the flow closest to the Earth's surface inside the PBL [25], [38]. This scheme is based on the Monin-Obukhov similarity theory, which states that the turbulent fluxes of heat and momentum are proportional to the vertical gradients of temperature and wind speed, respectively [21], [41].

The next layer up is the "mixed layer," characterized by convective turbulence driven by solar heating. The entrainment of air from the free atmosphere into the mixed layer is an important process that determines the growth of the mixed layer [4]. The most common parameterization scheme for the mixed layer is the K-profile parameterization, which assumes a linear variation of temperature and wind speed with height within the mixed layer [34], [84].

Above the mixed layer is the "upper boundary layer," which is characterized by a more stable stratification and a weaker turbulence intensity [4]. The parameterization of the upper boundary layer is less well established, and different schemes are used depending on the specific application [21], [84].

Boundary layer parameterization schemes improve numerical modeling by *having an ability* to capture PBL dynamics in numerical models [21], [41], [77]. Without these schemes, numerical models would not be able to accurately simulate the complex interactions between the atmosphere and the Earth's surface [41], [75], [83]. They also provide a framework for testing and comparing different parameterization schemes, which can lead to improvements in their accuracy and reliability ([see Figure 21](#)) [41], [77].

However, the lack of observational data<sup>22</sup> to validate the parameterization schemes and high computational demands lead to uncertainties in the accuracy of the simulations, limiting the ability to develop and improve the parameterization schemes [38], [83], [85]. Because the PBL is characterized by turbulent motions, it requires a high spatial and temporal resolution to accurately capture its dynamics, loading heavy computational costs on atmospheric models [10], [77], [84], [85]. Overall, the lack of observational data to validate boundary layer parameterization schemes is a major challenge, as it makes it difficult to evaluate the accuracy and reliability of the modeled atmospheric processes [10], [38], [41], [75], [77], [84], [85]. However, advances in observational techniques, such as remote sensing and in situ measurements, are helping to address some of these challenges and improve our understanding of boundary layer modeling [38], [83].

### *c. Radiative transfer models*

The radiative transfer model (or scheme) is a widely used method in numerical modeling for measuring PBL height. This model is based on the principle that the temperature of the PBL varies with height due to the absorption and emission of radiation by the atmosphere, considering the interaction of radiation with atmospheric gases and aerosols when estimating the PBL [32], [62], [69]. The radiative transfer equation is the fundamental equation governing the transfer of radiation through a medium, involving the scattering and absorption of radiation by atmospheric constituents. The equation can be solved numerically using various methods such as the discrete ordinate method, the Monte Carlo method, and the finite volume method [49], [61], [68]. These methods allow the radiative transfer equation to be solved for a range of atmospheric conditions and

geometries [38], [83], [86].

Radiative transfer schemes work by dividing the atmosphere into layers, each with its own temperature, pressure, and moisture content [41], [86]. The radiative transfer equation is then solved for each layer, allowing for net radiative flux at the top and bottom of each layer to be calculated [41], [77], [85].

The radiative transfer scheme is then coupled with other parameterization schemes, such as those for turbulence and convection, to simulate the complex processes that occur within the PBL [41]. The PBL height can then be estimated by identifying the layer where the vertical gradient of potential temperature or virtual potential temperature exceeds a certain threshold (see Figure 22) [21], [83].

One advantage of the radiative transfer parameterization scheme is its ability to capture the diurnal cycle of the PBL height, which is influenced by the changing balance between radiative cooling and turbulent mixing [41], [83]. It also allows for the simulation of the effects of aerosols on the PBL height, which is important for air quality and climate studies [41], [83].

Yet as dependent on models and their initialization, radiative transfer parameterization schemes rely on various assumptions about the atmosphere, such as the vertical distribution of aerosols, the existence of a horizontally homogeneous atmosphere and the neglect of horizontal advection [41], [77], [83]. They therefore can only provide information on PBL height rather than the PBL structure, limiting their usefulness in some applications (e.g., air quality forecasting) [10], [21], [75], [77], [85].

### *d. Turbulence closure schemes (local and non-local)*

In addition to other studies, Cohen et al. (2015) [84] explored various local and nonlocal PBL parameterization schemes used in numerical

---

<sup>22</sup> One of the challenges in using boundary layer parameterization schemes is the lack of observational data to validate the schemes for temporal and spatial variations [78], [85]. For instance, radiosondes can only provide point measurements and are limited in their spatial and temporal coverage [4], [11]. Other techniques such as lidar and remote sensing also have limitations in terms of their vertical resolution and the atmospheric conditions under which they can operate [55], [57], [75]. Additionally, ground-based observations are often limited in their spatial coverage and may not capture the full complexity of the PBL [54]. As a result, it can be difficult to validate boundary layer parameterization schemes and to accurately represent the boundary layer in numerical models [54], [78], [86].



weather prediction models and its associated processes (see Figure 23). These schemes can be classified as local or nonlocal, based on how they represent the turbulence and mixing within the PBL. Several schemes related to local and non-local techniques are presented in this section derived from Cohen's study. Local schemes simulate the PBL by parameterizing the turbulence and mixing processes within the surface layer, using simple algebraic equations to relate the vertical fluxes of momentum, heat, and moisture to the local gradients of these variables [34], [77], [84].

One such local scheme is the Blackadar (BK) technique, where assumptions about turbulence within the PBL are driven by buoyancy [83]. This scheme is computationally inexpensive and works well under stable atmospheric conditions, but falls short when representing the PBL in convective conditions due to its inability to capture the effects of shear-generated turbulence [34], [41], [84].

The Eddy-Diffusivity Mass-Flux (EDMF) scheme represents the PBL as a set of eddies with different sizes and velocities, producing turbulence and mixing through interacting with each other [83]. This scheme includes additional terms to represent the effects of entrainment and detrainment of air masses at the top and bottom of the PBL, capturing the diurnal cycle of the PBL for both stable and convective conditions [83]. However, it requires a larger number of model parameters and is more computationally expensive than the BK scheme [41], [84].

The Mellor-Yamada-Janjić (MYJ) scheme represents the PBL as a set of sublayers with different turbulence intensities, using algebraic equations to relate the vertical fluxes to the local gradients of temperature and wind speed within each sublayer [83]. Including effects of entrainment and detrainment of air masses, shear production and dissipation of turbulence, MYJ is suitable for both stable and convective conditions while remaining relatively computationally efficient (see Figure 24) [41], [84]. However, it may not accurately represent the PBL during rapidly changing atmospheric conditions [83].

Nonlocal schemes simulate the PBL by explicitly resolving the turbulence and mixing processes over a finite vertical domain [41], [77], [84]. They use differential equations to represent the evolution of the turbulent eddies and the associated fluxes of momentum, heat, and moisture [83].

The K-profile parameterization (KPP) scheme is one such nonlocal configuration that represents the PBL as a set of eddies with different sizes and velocities, using differential equations to represent the evolution of the turbulent kinetic energy within each eddy [83]. KPP includes terms to represent the effects of shear production and turbulent dissipation, as well as effects of entrainment and detrainment of air masses [83]. Also suitable for both stable and convective conditions, it requires a larger number of model parameters, making it more computationally expensive than the local schemes [41], [84].

The Nonlocal-Mellor-Yamada (NLMY) scheme extends the MYJ scheme by explicitly resolving the turbulence and mixing processes over a finite vertical domain [83]. Using differential equations to represent the evolution of the turbulent kinetic energy, the NLMY scheme includes vertical wind shear and molecular viscosity, making it more advantageous to other parameterizations in abilities to capture the effects of entrainment and detrainment, which can significantly impact the PBL height and structure [34], [78], [84]. This scheme also allows for vertical variability of turbulent kinetic energy, which can improve the representation of PBL dynamics in heterogeneous terrain [34], [84]. However, NLMY requires a higher demand computationally due to its higher-resolution grids, potentially limiting operational numerical weather prediction models [41], [84]. Additionally, the performance of the NLMY scheme is sensitive to the choice of model parameters and tuning, which can be challenging and time-consuming [83]. Outside of observations, parameterization schemes play a crucial role in numerical weather prediction models for representing turbulence and mixing approaches to define PBL structures [16], [34], [38], [41], [77], [78], [84]. Local schemes like the MRF and YSU schemes are computationally efficient and

suitable for stable and weakly unstable conditions (see Figures 23 and 24) [83]. However, they may not adequately capture the complex dynamics of the PBL under strongly unstable conditions [83]. Nonlocal schemes, such as the MYJ and NLMY schemes, are more accurate in simulating the PBL under a wider range of atmospheric conditions through the inclusion of eddy dispersion throughout the PBL (see Figures 23 and 24) [34], [77], [84]. Yet they require more computational resources due to their higher complexity [83]. Overall, choosing an appropriate parameterization scheme depends on the specific atmospheric conditions and the computational resources available [41], [78], [84].

#### IV. CONCLUSION

##### A. Challenges and Future Directions

Modeling PBL height and its characteristics remain a prevalent challenge despite the various methods available [47], [87]–[89]. Perhaps the most agreed-on factor that plays on the accuracy of modeling the PBL is the lack of precise measurements of PBL height and structure [7], [42], [54], [66], [84], [86]. Radiosonde measurements, for example, can be affected by uncertainties in the instrument calibration, atmospheric variability, and the vertical resolution of the instrument [4], [24], [37]. Similarly, Radar/Lidar measurements may be influenced by attenuation, beam broadening, and the presence of clouds and precipitation [56], [57], [61], [82]. Satellite measurements may also be hindered by atmospheric variability, cloud cover, and instrument calibration errors [66], [67]. In addition, Numerical Modeling techniques that rely on these observations also rely on various parameterization schemes that may not accurately represent the complex physics of the PBL, in part due to not being able to capture nocturnal to convective diurnal transitions [11], [21], [38], [78], [85].

Another challenge in modeling the PBL is the complex interplay between atmospheric processes, including radiation, convection, turbulence, and mixing [25], [48], [49], [52]. These processes are often nonlinear, and their interactions are difficult to model accurately [25], [78], [85], [86]. For example, the presence of

clouds and precipitation can affect the radiative balance of the atmosphere, leading to changes in temperature and vertical mixing [62], [74], [86]. The representation of these processes in numerical models can be challenging, particularly at high spatial and temporal resolutions [4], [26], [47], [88].

Furthermore, the PBL is influenced by a range of factors, including surface characteristics, topography, and synoptic weather patterns [14], [17], [38], [55]. These factors can introduce significant spatial and temporal variability in PBL height and structure, making it difficult to model the PBL accurately over large regions and timeframes [77], [84]. The effects of anthropogenic emissions on the PBL are not well understood, and their representation in numerical models remains a challenge [21], [38], [41], [65]. To address these challenges, efforts are underway to improve the accuracy and resolution of measurements used to characterize the PBL, primarily through investigating the benefit of a multi-method combination to balance the disadvantages of a single technique (see Figure 25) [37], [77], [90]. Such intercomparison studies involve comparing the results obtained from different models or observational techniques to assess their reliability and identify any discrepancies, which are crucial in improving the accuracy and reliability of atmospheric models and observational techniques (especially in the context of PBL modeling) [27], [90].

One type of intercomparison study involves comparing the results of different numerical models. For example, the Global Energy and Water Cycle Experiment (GEWEX) Continental-Scale International Project (GCIP) conducted an intercomparison of seven numerical models to determine their accuracy in simulating the PBL structure and its diurnal variation over the Southern Great Plains of the United States (see Figures 26 and 27) [91]–[96]. This study found that while all models captured the general structure of the PBL, there were significant differences in the predicted PBL height and its diurnal variation, highlighting the need for improved observational data [91]–[96]. The project also revealed the need for improved parameterizations of turbulence and mixing processes in PBL schemes, as the current parameterizations are often oversimplified and fail to capture the complex physics of the PBL [91]–



[96]. This is especially true for the transition between the convective and stable boundary as the timing and intensity of radiative cooling, the degree of surface cooling, and the strength of the nocturnal inversion are highly nonlinear and can vary substantially from one location to another (from the dependence on local meteorological and surface conditions) [4], [52], [93].

Another type of intercomparison study involves comparing the results of different observational techniques. For example, the Boundary Layer Late Afternoon and Sunset Turbulence ([BLLAST](#)) campaign conducted an intercomparison of different remote sensing techniques for estimating the PBL height using radiosondes, ceilometers and Doppler lidars [97]. This study found that the different techniques provided consistent estimates of the PBL height during the afternoon (convective PBL) but exhibited more variability during the evening and nighttime hours (nocturnal PBL) as mixing potential diminished [97]. This can be largely in part due to the shallow nature of the nocturnal PBL, making it difficult to capture the decoupling of the convective boundary layer from the surface and identify the combined effects of radiative cooling, surface cooling and entrainment of cooler air from above [4], [98]. Furthermore, the spatial heterogeneity of clouds, fog, and other low-lying atmospheric phenomena can obscure the PBL's boundary, further complicating remote sensing measurements [7], [87].

In addition to these specific studies, there are also ongoing intercomparison efforts as part of larger international projects. For example, the World Meteorological Organization's Global Atmosphere Watch ([GAW](#)) program has established a network of PBL observation sites worldwide to collect data on PBL height and structure using a variety of techniques [95]. The collected data is then used to evaluate the performance of different models and observational techniques and identify areas for improvement [95].

It remains clear that accurately modeling the PBL height and structure remains a challenging task in atmospheric science. The variety of observational techniques and numerical models available provide valuable information, but also introduce uncertainties and discrepancies in the data.

In terms of future research, it is important to

continue to develop and refine the available methods and models for PBL height and structure estimation. Further intercomparison studies between different techniques and models should be conducted to identify areas of uncertainty and improve the accuracy of estimates ([see Figure 28](#)). Additionally, incorporating more detailed and comprehensive observations and measurements, such as those from unmanned aerial vehicles (UAVs) or high-resolution remote sensing technologies, can provide additional insights into the PBL ([see Figure 29](#)) [95].

Moreover, advances in numerical modeling techniques and computing power allow for more sophisticated PBL parameterizations in climate models. These developments have the potential to improve the representation of the PBL and its interactions with other components of the Earth system, ultimately leading to more accurate predictions of weather and climate.

Overall, the challenges in modeling the PBL height and characteristics should not discourage further research in this area; rather it should motivate continued efforts to develop and improve methods and models, ultimately leading to a better understanding of the PBL and its role in the Earth system.

## REFERENCES

- [1] “2020 Tied for Warmest Year on Record, NASA Analysis Shows | NASA.” <https://www.nasa.gov/press-release/2020-tied-for-warmest-year-on-record-nasa-analysis-shows> (accessed Apr. 04, 2023).
- [2] Q. Schiermeier, “Climate change made Europe’s mega-heatwave five times more likely,” *Nature*, vol. 571, no. 7764, pp. 155–155, Jul. 2019, doi: 10.1038/d41586-019-02071-z.
- [3] M. Röthlisberger and L. Papritz, “Quantifying the physical processes leading to atmospheric hot extremes at a global scale,” *Nat. Geosci.*, vol. 16, no. 3, pp. 210–216, Mar. 2023, doi: 10.1038/s41561-023-01126-1.
- [4] S. Liu and X.-Z. Liang, “Observed Diurnal Cycle Climatology of Planetary Boundary Layer Height,” *Journal of Climate*, vol. 23, no. 21, pp. 5790–5809, Nov. 2010, doi: 10.1175/2010JCLI3552.1.
- [5] A. Molod, H. Salmun, and M. Dempsey, “Estimating Planetary Boundary Layer Heights



from NOAA Profiler Network Wind Profiler Data,” *Journal of Atmospheric and Oceanic Technology*, vol. 32, no. 9, pp. 1545–1561, Sep. 2015, doi: 10.1175/JTECH-D-14-00155.1.

[6] V. Caicedo *et al.*, “An Automated Common Algorithm for Planetary Boundary Layer Retrievals Using Aerosol Lidars in Support of the U.S. EPA Photochemical Assessment Monitoring Stations Program,” *Journal of Atmospheric and Oceanic Technology*, vol. 37, no. 10, pp. 1847–1864, Oct. 2020, doi: 10.1175/JTECH-D-20-0050.1.

[7] J. C. Compton, R. Delgado, T. A. Berkoff, and R. M. Hoff, “Determination of Planetary Boundary Layer Height on Short Spatial and Temporal Scales: A Demonstration of the Covariance Wavelet Transform in Ground-Based Wind Profiler and Lidar Measurements\*,” *Journal of Atmospheric and Oceanic Technology*, vol. 30, no. 7, pp. 1566–1575, Jul. 2013, doi: 10.1175/JTECH-D-12-00116.1.

[8] X. Wang, K. Wang, and L. Su, “Contribution of Atmospheric Diffusion Conditions to the Recent Improvement in Air Quality in China,” *Sci Rep*, vol. 6, no. 1, p. 36404, Nov. 2016, doi: 10.1038/srep36404.

[9] S. A. Cohn and W. M. Angevine, “Boundary Layer Height and Entrainment Zone Thickness Measured by Lidars and Wind-Profiling Radars,” *J. Appl. Meteor.*, vol. 39, no. 8, pp. 1233–1247, Aug. 2000, doi: 10.1175/1520-0450(2000)039<1233:BLHAEZ>2.0.CO;2.

[10] K. Nakoudi, E. Giannakaki, A. Dandou, M. Tombrou, and M. Kompoula, “Planetary boundary layer height by means of lidar and numerical simulations over New Delhi, India,” *Atmos. Meas. Tech.*, vol. 12, no. 5, pp. 2595–2610, May 2019, doi: 10.5194/amt-12-2595-2019.

[11] C. Sivaraman *et al.*, “Planetary Boundary Layer (PBL) Height Value Added Product (VAP): Radiosonde Retrievals,” 2013.

[12] R. Assmann, *The Vertical Structure of the Atmosphere in Clear and Cloudy Weather*. Springer-Verlag, 1908.

[13] R. B. Stull, *An introduction to boundary layer meteorology*. in Atmospheric and oceanographic sciences library, no. volume 13. Dordrecht: Springer, 2009.

[14] J. C. Kaimal and J. J. Finnigan, *Atmospheric boundary layer flows: their structure and measurement*. New York: Oxford University Press, 1994.

[15] J. R. Garratt and G. D. Hess, “BOUNDARY LAYERS | Neutrally Stratified Boundary Layer,” in *Encyclopedia of Atmospheric Sciences*, Elsevier, 2003, pp. 262–271. doi: 10.1016/B0-12-227090-8/00090-7.

[16] D. B. Kinnison and D. A. Randall, *The Planetary Boundary Layer: A Review of Physical Structure and Dynamics*. Annual Review of Fluid Mechanics, 1995.

[17] S. Roland, “The Atmospheric Boundary Layer,” in *Atmospheric Science*, Elsevier, 2006, pp. 375–417. doi: 10.1016/B978-0-12-732951-2.50014-4.

[18] G. K. Batchelor, *A History of the Atmospheric Boundary Layer*, vol. The Atmosphere and the Sea in Motion: Scientific Contributions to the Rossby Memorial Volume. Rockefeller Institute Press, 1970.

[19] R. T. DeGrandpre and J. L. Mitchell, *The History of Meteorology: To 1800*, vol. 14. American Meteorological Society, 1997.

[20] S. Schneider, *The Genesis and Early History of the General Circulation Model*. 1979.

[21] P. Oliveira, J. Soares, H. A. Karam, M. M. R. Pereira, and E. P. Marques Filho, “NUMERICAL MODELING OF THE PLANETARY BOUNDARY LAYER,” *RET*, vol. 3, no. 1, Jun. 2004, doi: 10.5380/ret.v3i1.3490.

[22] G. Tang *et al.*, “Mixing layer height and its implications for air pollution over Beijing, China,” *Atmos. Chem. Phys.*, vol. 16, no. 4, pp. 2459–2475, Mar. 2016, doi: 10.5194/acp-16-2459-2016.

[23] L. Wang *et al.*, “Vertical observations of the atmospheric boundary layer structure over Beijing urban area during air pollution episodes,” *Atmos. Chem. Phys.*, vol. 19, no. 10, pp. 6949–6967, May 2019, doi: 10.5194/acp-19-6949-2019.

[24] X. Y. Wang and K. C. Wang, “Estimation of atmospheric mixing layer height from radiosonde data,” *Atmos. Meas. Tech.*, vol. 7, no. 6, pp. 1701–1709, Jun. 2014, doi: 10.5194/amt-7-1701-2014.

[25] X.-Z. Liang *et al.*, “Surface Boundary Conditions for Mesoscale Regional Climate Models,” *Earth Interactions*, vol. 9, no. 18, pp. 1–28, Oct. 2005, doi: 10.1175/EI151.1.

[26] Q. Huang, X. Cai, J. Wang, Y. Song, and T. Zhu, “Climatological study of the Boundary-layer air Stagnation Index for China and its relationship with air pollution,” *Atmos. Chem. Phys.*, vol. 18, no. 10, pp. 7573–7593, May 2018,



doi: 10.5194/acp-18-7573-2018.

- [27] P. Seibert, "Review and intercomparison of operational methods for the determination of the mixing height," *Atmospheric Environment*, vol. 34, no. 7, pp. 1001–1027, 2000, doi: 10.1016/S1352-2310(99)00349-0.
- [28] G. C. Holzworth, "ESTIMATES OF MEAN MAXIMUM MIXING DEPTHS IN THE CONTIGUOUS UNITED STATES," *Mon. Wea. Rev.*, vol. 92, no. 5, pp. 235–242, May 1964, doi: 10.1175/1520-0493(1964)092<0235:EOMMMD>2.3.CO;2.
- [29] A. H. Cox, M. J. Dowling, G. W. Loomis, S. E. Engelhart, and J. A. Amador, "Geospatial Modeling Suggests Threats from Stormy Seas to Rhode Island's Coastal Septic Systems," *Journal of Sustainable Water in the Built Environment*, vol. 6, no. 3, Art. no. 3, Aug. 2020, doi: 10.1061/JSWBAY.0000917.
- [30] I. M. Brooks, "Finding Boundary Layer Top: Application of a Wavelet Covariance Transform to Lidar Backscatter Profiles," *J. Atmos. Oceanic Technol.*, vol. 20, no. 8, pp. 1092–1105, Aug. 2003, doi: 10.1175/1520-0426(2003)020<1092:FBLTAO>2.0.CO;2.
- [31] X. Wang, R. E. Dickinson, L. Su, C. Zhou, and K. Wang, "PM<sub>2.5</sub> Pollution in China and How It Has Been Exacerbated by Terrain and Meteorological Conditions," *Bulletin of the American Meteorological Society*, vol. 99, no. 1, pp. 105–119, Jan. 2018, doi: 10.1175/BAMS-D-16-0301.1.
- [32] D. E. Horton, Harshvardhan, and N. S. Duffenbaugh, "Response of air stagnation frequency to anthropogenically enhanced radiative forcing," *Environ. Res. Lett.*, vol. 7, no. 4, p. 044034, Dec. 2012, doi: 10.1088/1748-9326/7/4/044034.
- [33] R. S. Bradley, F. T. Keimig, and H. F. Diaz, "Climatology of surface-based inversions in the North American Arctic," *J. Geophys. Res.*, vol. 97, no. D14, p. 15699, 1992, doi: 10.1029/92JD01451.
- [34] L. Zhang *et al.*, "Understanding the Major Impact of Planetary Boundary Layer Schemes on Simulation of Vertical Wind Structure," *Atmosphere*, vol. 12, no. 6, p. 777, Jun. 2021, doi: 10.3390/atmos12060777.
- [35] L. Bianco and J. M. Wilczak, "Convective Boundary Layer Depth: Improved Measurement by Doppler Radar Wind Profiler Using Fuzzy Logic Methods," *J. Atmos. Oceanic Technol.*, vol.

- 19, no. 11, pp. 1745–1758, Nov. 2002, doi: 10.1175/1520-0426(2002)019<1745:CBLDIM>2.0.CO;2.
- [36] J. M. Garrido-Perez, R. García-Herrera, and C. Ordóñez, "Assessing the value of air stagnation indices to reproduce PM<sub>10</sub> variability in Europe," *Atmospheric Research*, vol. 248, p. 105258, Jan. 2021, doi: 10.1016/j.atmosres.2020.105258.
- [37] D. J. Seidel, C. O. Ao, and K. Li, "Estimating climatological planetary boundary layer heights from radiosonde observations: Comparison of methods and uncertainty analysis," *J. Geophys. Res.*, vol. 115, no. D16, p. D16113, Aug. 2010, doi: 10.1029/2009JD013680.
- [38] S. M. Njuki, C. M. Mannaerts, and Z. Su, "Influence of Planetary Boundary Layer (PBL) Parameterizations in the Weather Research and Forecasting (WRF) Model on the Retrieval of Surface Meteorological Variables over the Kenyan Highlands," *Atmosphere*, vol. 13, no. 2, p. 169, Jan. 2022, doi: 10.3390/atmos13020169.
- [39] J. M. Wallace and P. V. Hobbs, *Atmospheric science: an introductory survey*. New York: Academic Press, 1977.
- [40] X. Wang and K. Wang, "Homogenized Variability of Radiosonde-Derived Atmospheric Boundary Layer Height over the Global Land Surface from 1973 to 2014," *Journal of Climate*, vol. 29, no. 19, pp. 6893–6908, Oct. 2016, doi: 10.1175/JCLI-D-15-0766.1.
- [41] D. J. Stensrud, M. C. Coniglio, K. H. Knopfmeier, and A. J. Clark, "NUMERICAL MODELS | Model Physics Parameterization," in *Encyclopedia of Atmospheric Sciences*, Elsevier, 2015, pp. 167–180. doi: 10.1016/B978-0-12-382225-3.00493-X.
- [42] J. Guo *et al.*, "A merged continental planetary boundary layer height dataset based on high-resolution radiosonde measurements, ERA5 reanalysis, and GLDAS," *Meteorology*, preprint, May 2022. doi: 10.5194/essd-2022-150.
- [43] Y. Zhang *et al.*, "On the computation of planetary boundary-layer height using the bulk Richardson number method," *Geosci. Model Dev.*, vol. 7, no. 6, pp. 2599–2611, Nov. 2014, doi: 10.5194/gmd-7-2599-2014.
- [44] J. Guo *et al.*, "Investigation of near-global daytime boundary layer height using high-resolution radiosondes: First results and comparison with ERA-5, MERRA-2, JRA-55, and NCEP-2 reanalyses," *Aerosols/Remote*



Sensing/Troposphere/Physics (physical properties and processes), preprint, May 2021. doi: 10.5194/acp-2021-257.

[45] H. Li, J. Chang, Z. Liu, L. Zhang, T. Dai, and S. Chen, “An improved method for automatic determination of the planetary boundary layer height based on lidar data,” *Journal of Quantitative Spectroscopy and Radiative Transfer*, vol. 257, p. 107382, Dec. 2020, doi: 10.1016/j.jqsrt.2020.107382.

[46] W.-Y. Sun and O. M. Sun, “Revisiting the parcel method and CAPE,” *Dynamics of Atmospheres and Oceans*, vol. 86, pp. 134–152, Jun. 2019, doi: 10.1016/j.dynatmoce.2019.03.008.

[47] M. Collaud Coen, C. Praz, A. Haeferle, D. Ruffieux, P. Kaufmann, and B. Calpini, “Determination and climatology of the planetary boundary layer height above the Swiss plateau by in situ and remote sensing measurements as well as by the COSMO-2 model,” *Atmos. Chem. Phys.*, vol. 14, no. 23, pp. 13205–13221, Dec. 2014, doi: 10.5194/acp-14-13205-2014.

[48] X. Feng, B. Wu, and N. Yan, “A Method for Deriving the Boundary Layer Mixing Height from MODIS Atmospheric Profile Data,” *Atmosphere*, vol. 6, no. 9, pp. 1346–1361, Sep. 2015, doi: 10.3390/atmos6091346.

[49] S. Odintsov, E. Miller, A. Kamardin, I. Nevzorova, A. Troitsky, and M. Schröder, “Investigation of the Mixing Height in the Planetary Boundary Layer by Using Sodar and Microwave Radiometer Data,” *Environments*, vol. 8, no. 11, p. 115, Oct. 2021, doi: 10.3390/environments8110115.

[50] W. M. Angevine, A. B. White, and S. K. Avery, “Boundary-layer depth and entrainment zone characterization with a boundary-layer profiler,” *Boundary-Layer Meteorol.*, vol. 68, no. 4, pp. 375–385, Mar. 1994, doi: 10.1007/BF00706797.

[51] L. Mei *et al.*, “Detection of the planetary boundary layer height by employing the Scheimpflug lidar technique and the covariance wavelet transform method,” *Appl. Opt.*, vol. 58, no. 29, p. 8013, Oct. 2019, doi: 10.1364/AO.58.008013.

[52] T. Su, Z. Li, and R. Kahn, “A new method to retrieve the diurnal variability of planetary boundary layer height from lidar under different thermodynamic stability conditions,” *Remote Sensing of Environment*, vol. 237, p. 111519, Feb. 2020, doi:

10.1016/j.rse.2019.111519.

[53] A. Tangborn, B. Demoz, B. J. Carroll, J. Santanello, and J. L. Anderson, “Assimilation of lidar planetary boundary layer height observations,” *Atmos. Meas. Tech.*, vol. 14, no. 2, pp. 1099–1110, Feb. 2021, doi: 10.5194/amt-14-1099-2021.

[54] Y.-C. Wang, S.-H. Wang, J. R. Lewis, S.-C. Chang, and S. M. Griffith, “Determining Planetary Boundary Layer Height by Micro-pulse Lidar with Validation by UAV Measurements,” *Aerosol Air Qual. Res.*, vol. 21, no. 5, p. 200336, 2021, doi: 10.4209/aaqr.200336.

[55] D. Summa, P. Di Girolamo, and D. Stelitano, “Characterization of PBL height and structure by Raman lidar: Selected case studies from the convective and orographically-induced precipitation study,” presented at the RADIATION PROCESSES IN THE ATMOSPHERE AND OCEAN (IRS2012): Proceedings of the International Radiation Symposium (IRC/IAMAS), Dahlem Cube, Free University, Berlin, 2013, pp. 208–211. doi: 10.1063/1.4804743.

[56] L. Wang, W. Qiang, H. Xia, T. Wei, J. Yuan, and P. Jiang, “Robust Solution for Boundary Layer Height Detections with Coherent Doppler Wind Lidar,” *Adv. Atmos. Sci.*, vol. 38, no. 11, pp. 1920–1928, Nov. 2021, doi: 10.1007/s00376-021-1068-0.

[57] Y. Chen, X. Jin, N. Weng, W. Zhu, Q. Liu, and J. Chen, “Simultaneous Extraction of Planetary Boundary-Layer Height and Aerosol Optical Properties from Coherent Doppler Wind Lidar,” *Sensors*, vol. 22, no. 9, p. 3412, Apr. 2022, doi: 10.3390/s22093412.

[58] W. M. Angevine, “Radio acoustic sounding system (RASS) applications and limitations,” in *IGARSS 2000. IEEE 2000 International Geoscience and Remote Sensing Symposium. Taking the Pulse of the Planet: The Role of Remote Sensing in Managing the Environment. Proceedings (Cat. No.00CH37120)*, Honolulu, HI, USA: IEEE, 2000, pp. 1180–1182. doi: 10.1109/IGARSS.2000.858060.

[59] T. V. Chandrasekhar Sarma, P. Srinivasulu, and T. Tsuda, “Preliminary observation of temperature profiles by radio acoustic sounding system (RASS) with a 1280 MHz lower atmospheric wind profiler at Gadanki, India,” Others (Wind, Precipitation, Temperature, etc.)/Remote Sensing/Instruments and Platforms,



preprint, Jun. 2012. doi: 10.5194/amtd-5-4447-2012.

[60] J. M. Jacobs, R. L. Coulter, and W. Brutsaert, "Surface heat flux estimation with wind-profiler/RASS and radiosonde observations," *Advances in Water Resources*, vol. 23, no. 4, pp. 339–348, Jan. 2000, doi: 10.1016/S0309-1708(99)00028-7.

[61] H. Li, J. Chang, Z. Liu, L. Zhang, T. Dai, and S. Chen, "An improved method for automatic determination of the planetary boundary layer height based on lidar data," *Journal of Quantitative Spectroscopy and Radiative Transfer*, vol. 257, p. 107382, Dec. 2020, doi: 10.1016/j.jqsrt.2020.107382.

[62] D. Zhang, J. Comstock, and V. Morris, "Comparison of planetary boundary layer height from ceilometer with ARM radiosonde data," *Atmos. Meas. Tech.*, vol. 15, no. 16, pp. 4735–4749, Aug. 2022, doi: 10.5194/amt-15-4735-2022.

[63] H. D. Kambezidis, B. E. Psiloglou, A. Gavriil, and K. Petrinoli, "Detection of Upper and Lower Planetary-Boundary Layer Curves and Estimation of Their Heights from Ceilometer Observations under All-Weather Conditions: Case of Athens, Greece," *Remote Sensing*, vol. 13, no. 11, p. 2175, Jun. 2021, doi: 10.3390/rs13112175.

[64] J. Lee *et al.*, "Ceilometer Monitoring of Boundary-Layer Height and Its Application in Evaluating the Dilution Effect on Air Pollution," *Boundary-Layer Meteorol.*, vol. 172, no. 3, pp. 435–455, Sep. 2019, doi: 10.1007/s10546-019-00452-5.

[65] H. N. Duc *et al.*, "Study of Planetary Boundary Layer, Air Pollution, Air Quality Models and Aerosol Transport Using Ceilometers in New South Wales (NSW), Australia," *Atmosphere*, vol. 13, no. 2, p. 176, Jan. 2022, doi: 10.3390/atmos13020176.

[66] M. Santosh, "Estimation of daytime planetary boundary layer height (PBLH) over the tropics and subtropics using COSMIC-2/FORMOSAT-7 GNSS-RO measurements," *Atmospheric Research*, vol. 279, p. 106361, Dec. 2022, doi: 10.1016/j.atmosres.2022.106361.

[67] S. P. Palm, P. Selmer, J. Yorks, S. Nicholls, and E. Nowottnick, "Planetary Boundary Layer Height Estimates From ICESat-2 and CATS Backscatter Measurements," *Front. Remote Sens.*, vol. 2, p. 716951, Sep. 2021, doi: 10.3389/frsen.2021.716951.

[68] G. De Arruda Moreira *et al.*, "Study of the planetary boundary layer by microwave radiometer, elastic lidar and Doppler lidar estimations in Southern Iberian Peninsula," *Atmospheric Research*, vol. 213, pp. 185–195, Nov. 2018, doi: 10.1016/j.atmosres.2018.06.007.

[69] S. M. Loria-Salazar *et al.*, "Evaluation of Novel NASA Moderate Resolution Imaging Spectroradiometer and Visible Infrared Imaging Radiometer Suite Aerosol Products and Assessment of Smoke Height Boundary Layer Ratio During Extreme Smoke Events in the Western USA," *JGR Atmospheres*, vol. 126, no. 11, Jun. 2021, doi: 10.1029/2020JD034180.

[70] M. Mitchell, R. E. Isdell, J. Herman, and C. Tombleson, "Impact Assessment and Management Challenges of Key Rural Human Health Infrastructure Under Sea Level Rise," *Frontiers in Marine Science*, vol. 8, 2021, Accessed: Jul. 10, 2022. [Online]. Available: <https://www.frontiersin.org/articles/10.3389/fmars.2021.631757>

[71] B. Albina, M. M. Cazacu, A. Timofte, D. G. Dimitriu, and S. O. Gurlui, "Studies of planetary boundary layer by infrared thermal imagery," presented at the TIM 2013 PHYSICS CONFERENCE, Timisoara, Romania, 2014, pp. 174–179. doi: 10.1063/1.4903034.

[72] M. T. Richardson, D. R. Thompson, M. J. Kurowski, and M. D. Lebsock, "Boundary layer water vapour statistics from high-spatial-resolution spaceborne imaging spectroscopy," *Atmos. Meas. Tech.*, vol. 14, no. 8, pp. 5555–5576, Aug. 2021, doi: 10.5194/amt-14-5555-2021.

[73] C. O. Ao *et al.*, "Planetary boundary layer heights from GPS radio occultation refractivity and humidity profiles: PBL HEIGHT FROM GPS RO," *J. Geophys. Res.*, vol. 117, no. D16, p. n/a-n/a, Aug. 2012, doi: 10.1029/2012JD017598.

[74] Y. Wang, X. Zeng, X. Xu, F. Xie, and Y. Zhao, "Improving the Estimate of Summer Daytime Planetary Boundary Layer Height Over Land From GPS Radio Occultation Data," *Geophysical Research Letters*, vol. 49, no. 2, Jan. 2022, doi: 10.1029/2021GL096304.

[75] T. Gal-Chen, M. Xu, and W. L. Eberhard, "Estimations of atmospheric boundary layer fluxes and other turbulence parameters from Doppler lidar data," *J. Geophys. Res.*, vol. 97, no. D17, p. 18409, 1992, doi: 10.1029/91JD03174.

[76] D. Li, "Turbulent Prandtl number in the



atmospheric boundary layer - where are we now?," *Atmospheric Research*, vol. 216, pp. 86–105, Feb. 2019, doi:

10.1016/j.atmosres.2018.09.015.

[77] "A Comparison of Three Boundary Layer Schemes for Numerical Weather Prediction," *Appl. Math. Inf. Sci.*, vol. 14, no. 6, pp. 1093–1101, Nov. 2020, doi: 10.18576/amis/140616.

[78] A. Peña and A. N. Hahmann, "Evaluating planetary boundary-layer schemes and large-eddy simulations with measurements from a 250-m meteorological mast," *J. Phys.: Conf. Ser.*, vol. 1618, no. 6, p. 062001, Sep. 2020, doi: 10.1088/1742-6596/1618/6/062001.

[79] X. Yin, C. Jiang, Y. Shao, N. Huang, and J. Zhang, "Large-eddy-simulation study on turbulent particle deposition and its dependence on atmospheric-boundary-layer stability," *Atmos. Chem. Phys.*, vol. 22, no. 7, pp. 4509–4522, Apr. 2022, doi: 10.5194/acp-22-4509-2022.

[80] U. Rizza *et al.*, "Large-eddy simulation of the planetary boundary layer under baroclinic conditions during daytime and sunset turbulence: LES of daytime and sunset turbulence," *Met. Apps*, vol. 20, no. 1, pp. 56–71, Mar. 2013, doi: 10.1002/met.1284.

[81] M. Auvinen, S. Boi, A. Hellsten, T. Tanhuanpää, and L. Järvi, "Study of Realistic Urban Boundary Layer Turbulence with High-Resolution Large-Eddy Simulation," *Atmosphere*, vol. 11, no. 2, p. 201, Feb. 2020, doi: 10.3390/atmos11020201.

[82] K. Nakoudi, E. Giannakaki, A. Dandou, M. Tombrou, and M. Kompoula, "Planetary boundary layer height by means of lidar and numerical simulations over New Delhi, India," *Atmos. Meas. Tech.*, vol. 12, no. 5, pp. 2595–2610, May 2019, doi: 10.5194/amt-12-2595-2019.

[83] A. E. Cohen, S. M. Cavallo, M. C. Coniglio, and H. E. Brooks, "A Review of Planetary Boundary Layer Parameterization Schemes and Their Sensitivity in Simulating Southeastern U.S. Cold Season Severe Weather Environments," *Weather and Forecasting*, vol. 30, no. 3, pp. 591–612, Jun. 2015, doi: 10.1175/WAF-D-14-00105.1.

[84] A. E. Cohen, S. M. Cavallo, M. C. Coniglio, and H. E. Brooks, "A Review of Planetary Boundary Layer Parameterization Schemes and Their Sensitivity in Simulating Southeastern U.S. Cold Season Severe Weather Environments," *Weather and Forecasting*, vol.

30, no. 3, pp. 591–612, Jun. 2015, doi:

10.1175/WAF-D-14-00105.1.

[85] H. H. Shin and J. Dudhia, "Evaluation of PBL Parameterizations in WRF at Subkilometer Grid Spacings: Turbulence Statistics in the Dry Convective Boundary Layer," *Monthly Weather Review*, vol. 144, no. 3, pp. 1161–1177, Mar. 2016, doi: 10.1175/MWR-D-15-0208.1.

[86] A. Atmosphere Radiation Measurement User Facility, "New Evaluation Product Estimates of Planetary Boundary Layer Height." Jul. 03, 2012. [Online]. Available:

<https://www.arm.gov/news/data/post/18304>

[87] J. D. Hegarty *et al.*, "Analysis of the Planetary Boundary Layer Height during DISCOVER-AQ Baltimore–Washington, D.C., with Lidar and High-Resolution WRF Modeling," *Journal of Applied Meteorology and Climatology*, vol. 57, no. 11, pp. 2679–2696, Nov. 2018, doi: 10.1175/JAMC-D-18-0014.1.

[88] B. Stevens, "The Role of the Planetary Boundary Layer in Climate Modeling," *Journal of Climate*, 2005.

[89] Y. Zhang, D. J. Seidel, J.-C. Golaz, C. Deser, and R. A. Tomas, "Climatological Characteristics of Arctic and Antarctic Surface-Based Inversions," *J. Climate*, vol. 24, no. 19, pp. 5167–5186, Oct. 2011, doi: 10.1175/2011JCLI4004.1.

[90] C. Q. Dias-Júnior *et al.*, "Intercomparison of Planetary Boundary Layer Heights Using Remote Sensing Retrievals and ERA5 Reanalysis over Central Amazonia," *Remote Sensing*, vol. 14, no. 18, p. 4561, Sep. 2022, doi: 10.3390/rs14184561.

[91] M. F. McCabe, A. Ershadi, C. Jimenez, D. G. Miralles, D. Michel, and E. F. Wood, "The GEWEX LandFlux project: evaluation of model evaporation using tower-based and globally gridded forcing data," *Geosci. Model Dev.*, vol. 9, no. 1, pp. 283–305, Jan. 2016, doi: 10.5194/gmd-9-283-2016.

[92] V. Wulfmeyer, "LAND - ATMOSPHERE FEEDBACK EXPERIMENT (LAFe)." Atmospheric Radiation Measurement (ARM), Aug. 31, 2017. [Online]. Available: <https://www.arm.gov/research/campaigns/sgp2017/lafe>

[93] GEWEX, "LS4P and TPemip: Third Pole Land Surface and Subsurface Temperatures May Have Substantial Remote Predictive Capability for Subseasonal to Seasonal



- Precipitation,” *GEWEX Quarterly*, vol. 24, no. 4, 2019, [Online]. Available: [chrome-extension://efaidnbmnnnibpcajpcglclefindmkaj/https://www.gewex.org/gewex-content/files\\_mf/1576784370Nov2019.pdf](chrome-extension://efaidnbmnnnibpcajpcglclefindmkaj/https://www.gewex.org/gewex-content/files_mf/1576784370Nov2019.pdf)
- [94] Read “Global Energy and Water Cycle Experiment (GEWEX) Continental-Scale International Project: A Review of Progress and Opportunities” at *NAP.edu*. doi: 10.17226/6149.
- [95] “Global Atmosphere Watch Programme,” Oct. 15, 2015. <https://public.wmo.int/en/programmes/global-atmosphere-watch-programme> (accessed May 07, 2023).
- [96] “Global Energy and Water Exchanges (GEWEX).” <https://www.wcrp-climate.org/gewex> (accessed May 07, 2023).
- [97] M. Lothon *et al.*, “The BLLAST field experiment: Boundary-Layer Late Afternoon and Sunset Turbulence,” *Atmos. Chem. Phys.*, vol. 14, no. 20, pp. 10931–10960, Oct. 2014, doi: 10.5194/acp-14-10931-2014.
- [98] T. Su, Z. Li, and R. Kahn, “A new method to retrieve the diurnal variability of planetary boundary layer height from lidar under different thermodynamic stability conditions,” *Remote Sensing of Environment*, vol. 237, p. 111519, Feb. 2020, doi: 10.1016/j.rse.2019.111519.

APPENDIX

FIGURES

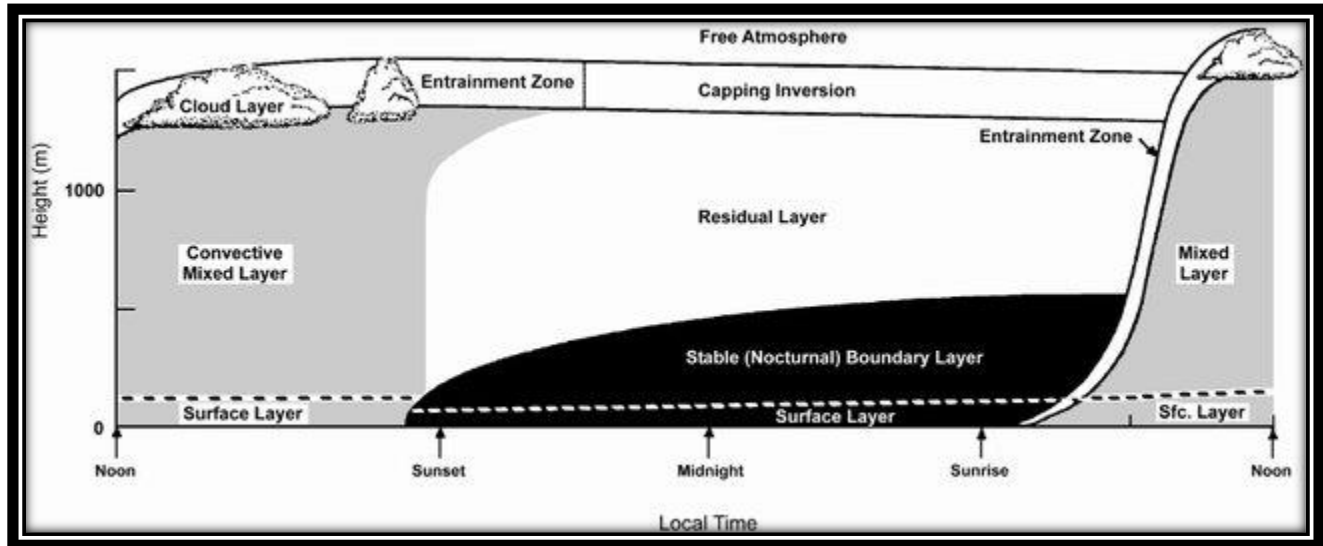


Figure 1- The planetary boundary layer with its three primary sub-layers. The less turbulent residual layer contains the former mixed layer air and the stable (nocturnal) inversion layer.

Source: Stull, 1998, *Introduction to Boundary Layer Meteorology* [13]

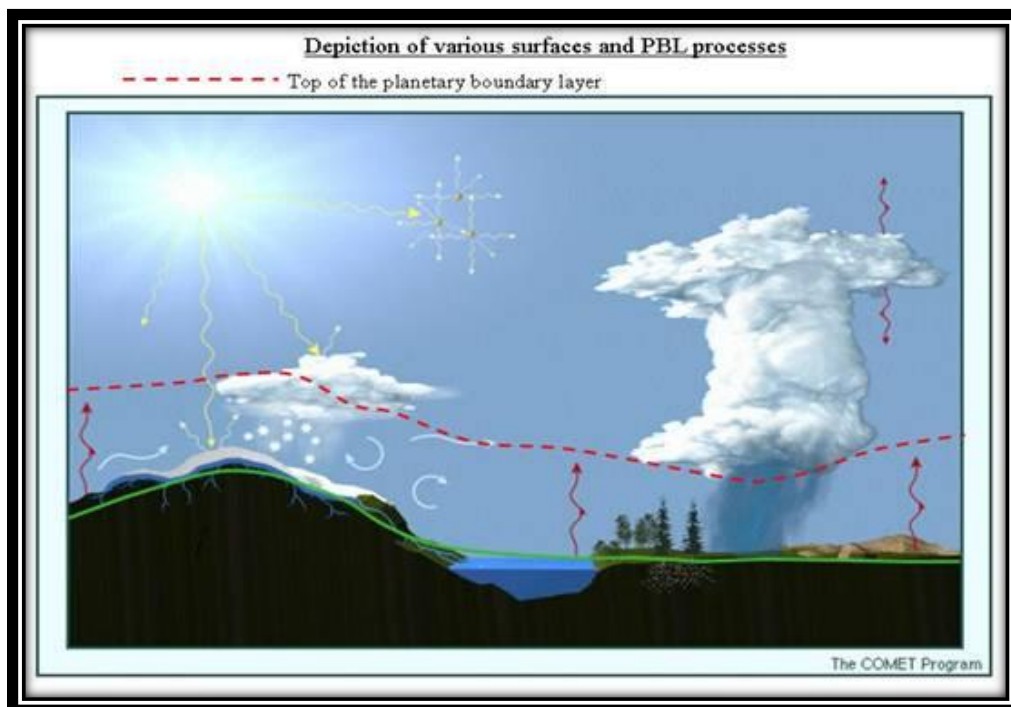


Figure 2- A visual summary of the planetary boundary layer over different surfaces.

Source: NOAA Earth System Research Laboratory

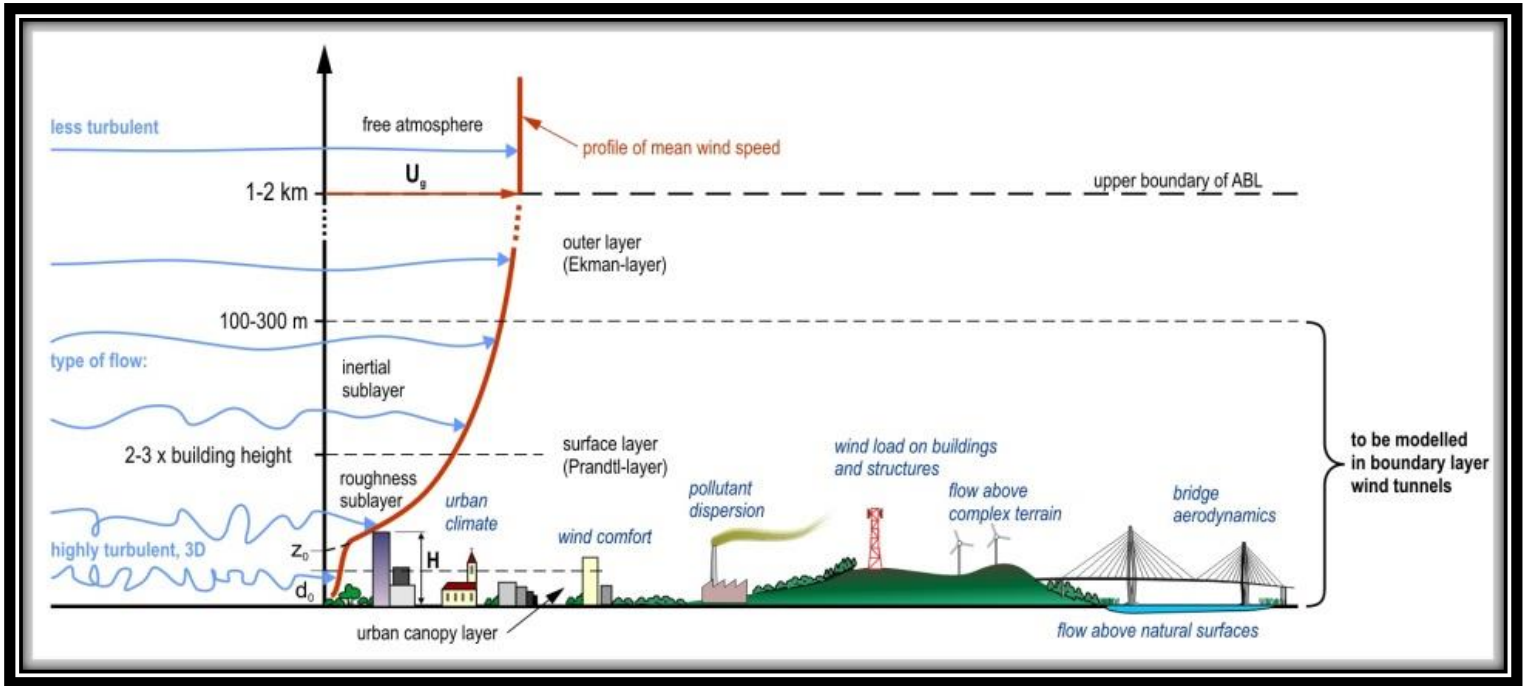


Figure 3- Features and layers of the planetary boundary layer, including phenomena suitable for wind tunnel analysis. Notice the wind characteristics influenced by surface elements, disrupting smooth flow and generating turbulent eddies.

Source: Budapest University of Technology and Economics (BME) Atmospheric Flow Laboratory.

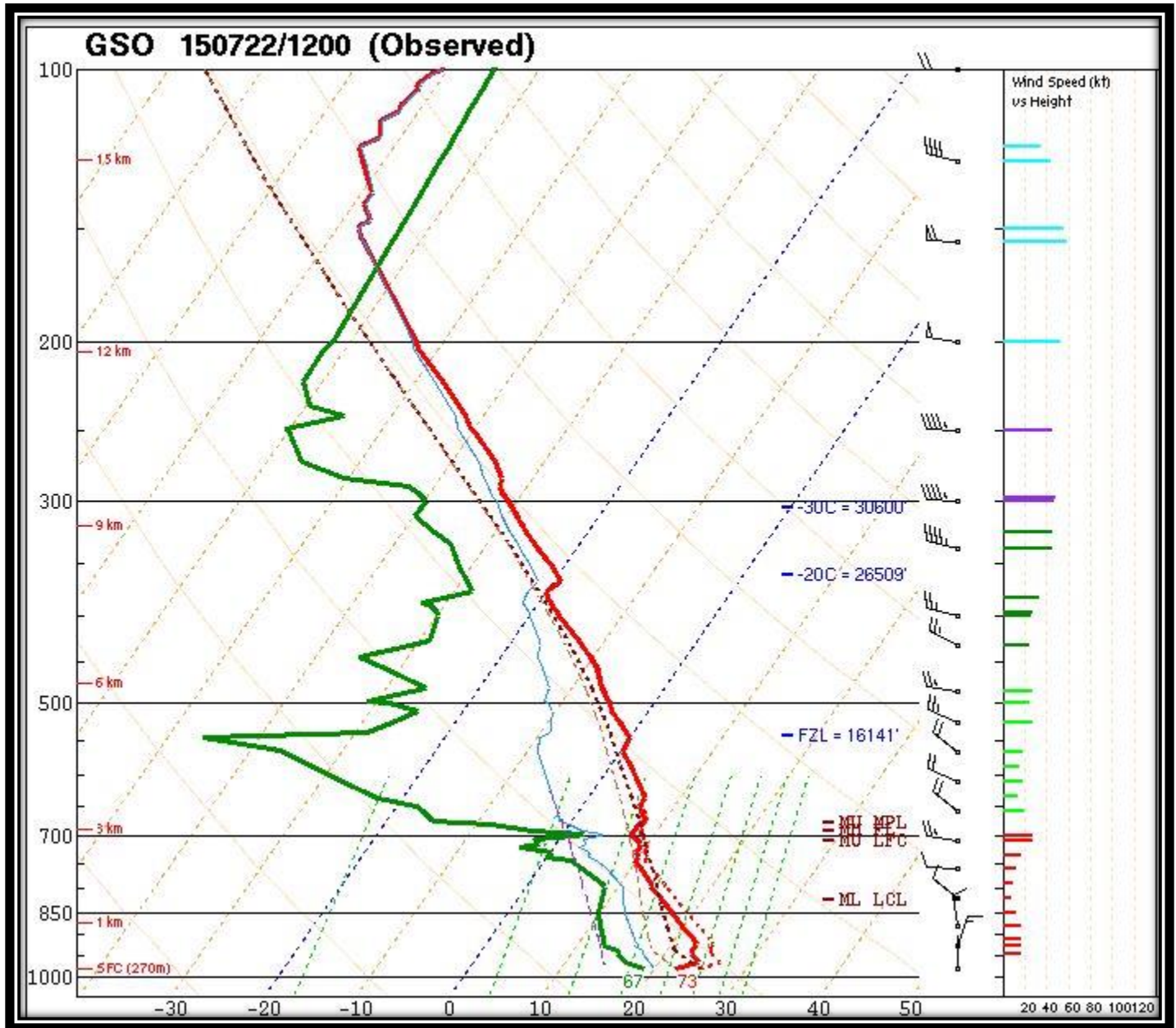
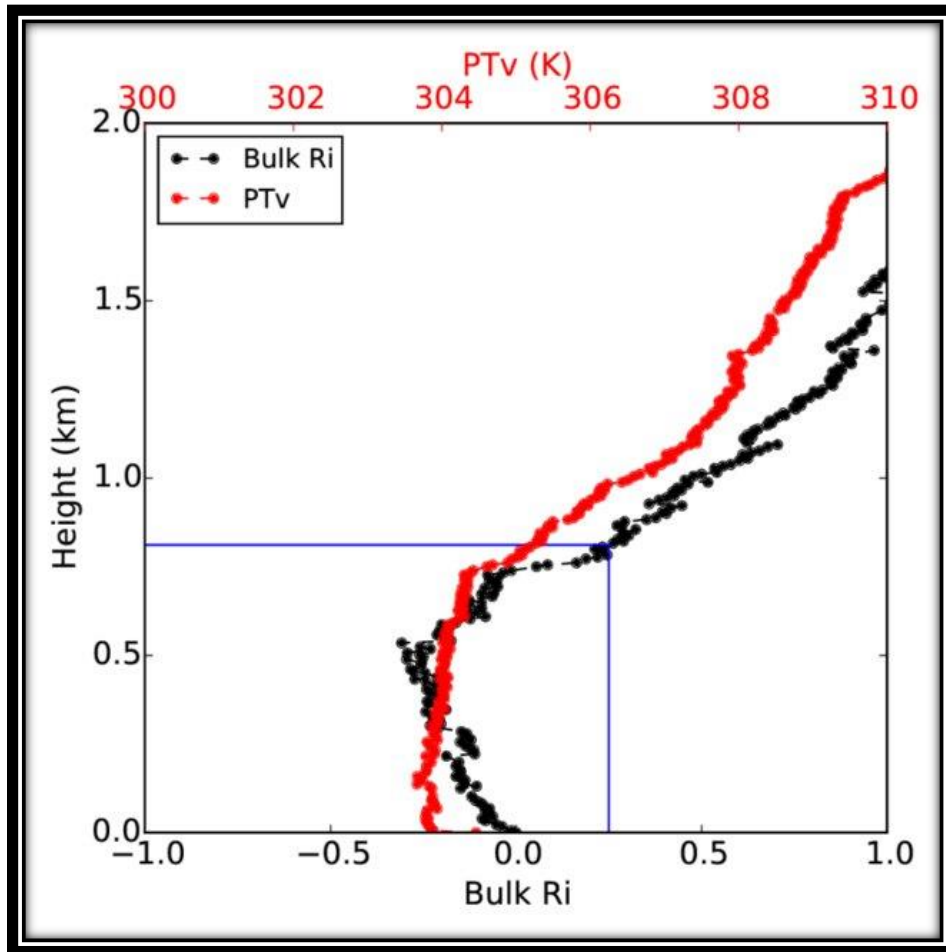


Figure 4- A graphical representation displaying a sample of radiosonde data, wherein the variation of temperature with altitude is depicted through a prominent red line. The green line depicts the dewpoint, indicating atmospheric moisture at specific levels. Additionally, the chart incorporates wind barbs denoting the wind direction and speed with increasing altitude.

Source: National Weather Service.



*Figure 5- Using L-band sounding observations taken in Beijing on 30th June 2013 at 1400 BJT, a graphical representation depicts the variations in the bulk Richardson number (Ri, shown in black) and virtual potential temperature (PTv, represented in red) along vertical profiles. The boundary layer height corresponds to the altitude where Ri initially attains a value of 0.25, denoted by the presence of blue lines.*

Source: Miao et al. 2016.

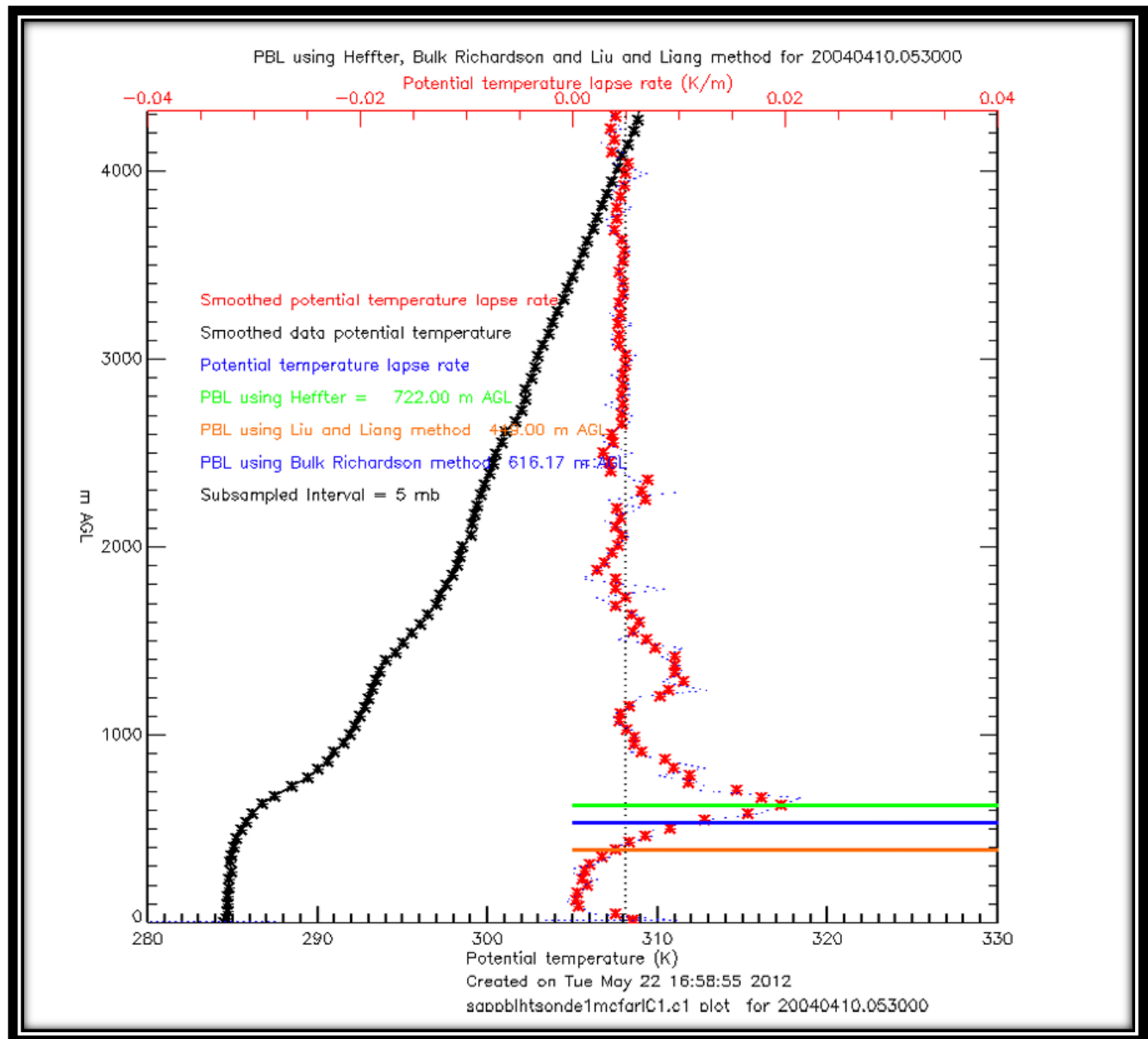


Figure 6- Example plot from the Atmospheric Radiation Measurement (ARM) Value-Added Product (VAP) showing potential temperature (black) and potential temperature lapse rates (red) from a single radiosonde along with the estimates of PBL height from the three methods shown. Particular attention should be devoted to the Bulk Richardson and Liu & Liang Methods, with horizontal lines colored to represent their respective PBL height approximation.

Source: [www.ARM.gov](http://www.ARM.gov)

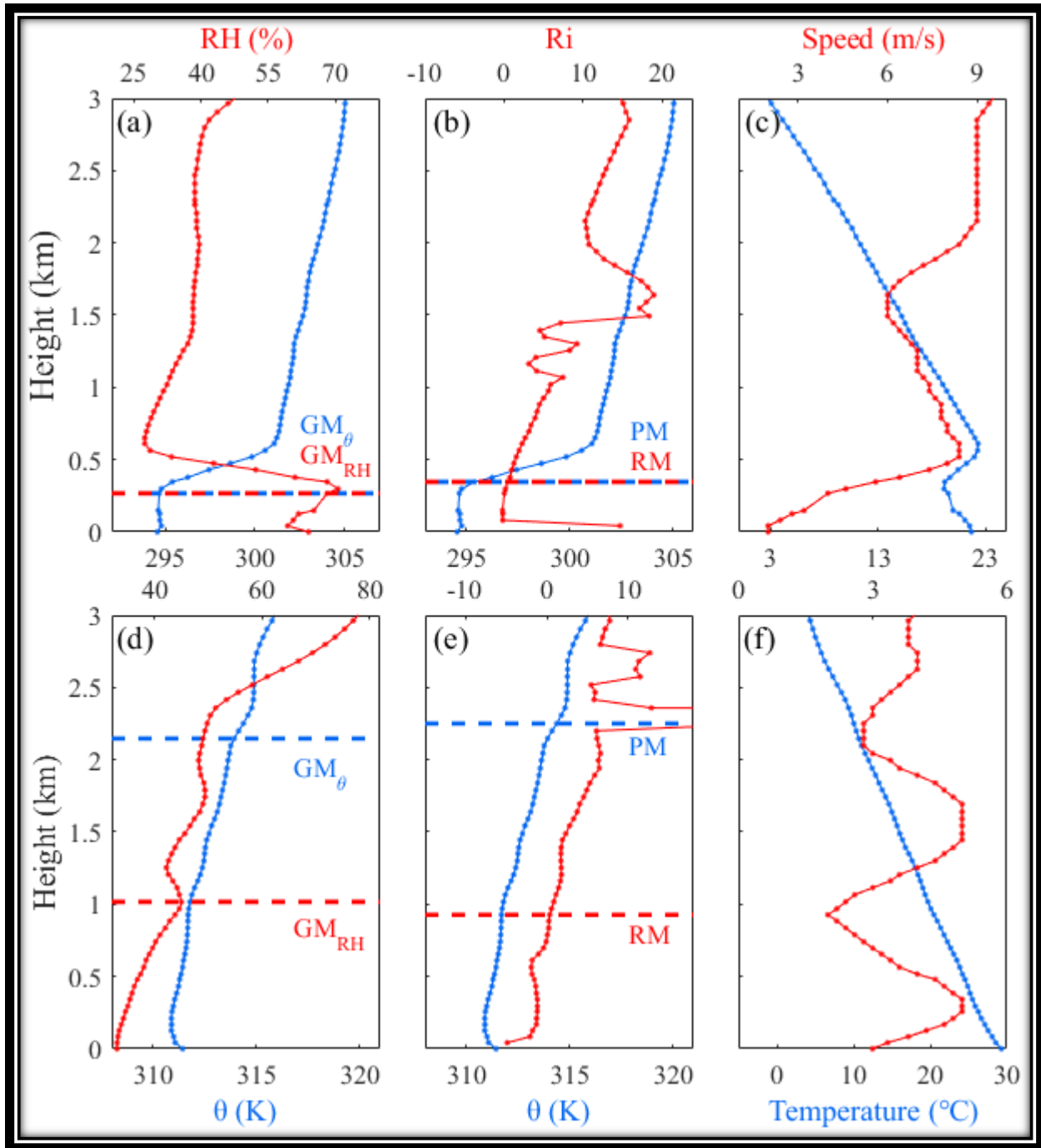


Figure 7- Case studies of PBLH determination from (a) potential temperature gradient method ( $GM_{\theta}$ ) (blue) and relative humidity ( $RH$ ) gradient method ( $GM_{RH}$ ) (red), (b) parcel method ( $PM$ ) (blue) and Richardson's Number method ( $RM$ ) (red), and (c) profiles of temperature (blue) and wind speed (red) under a daytime PBL (convective PBL) classification. Note the uplifted inversion layers in the profiles. Clearly identifiable lifted inversion layers are observed when determining PBLH through the four methods, suggesting that the boundary layer's configuration impacts the dependability of PBLH results derived from remote sensing data.

Source: Liu et al. 2021.

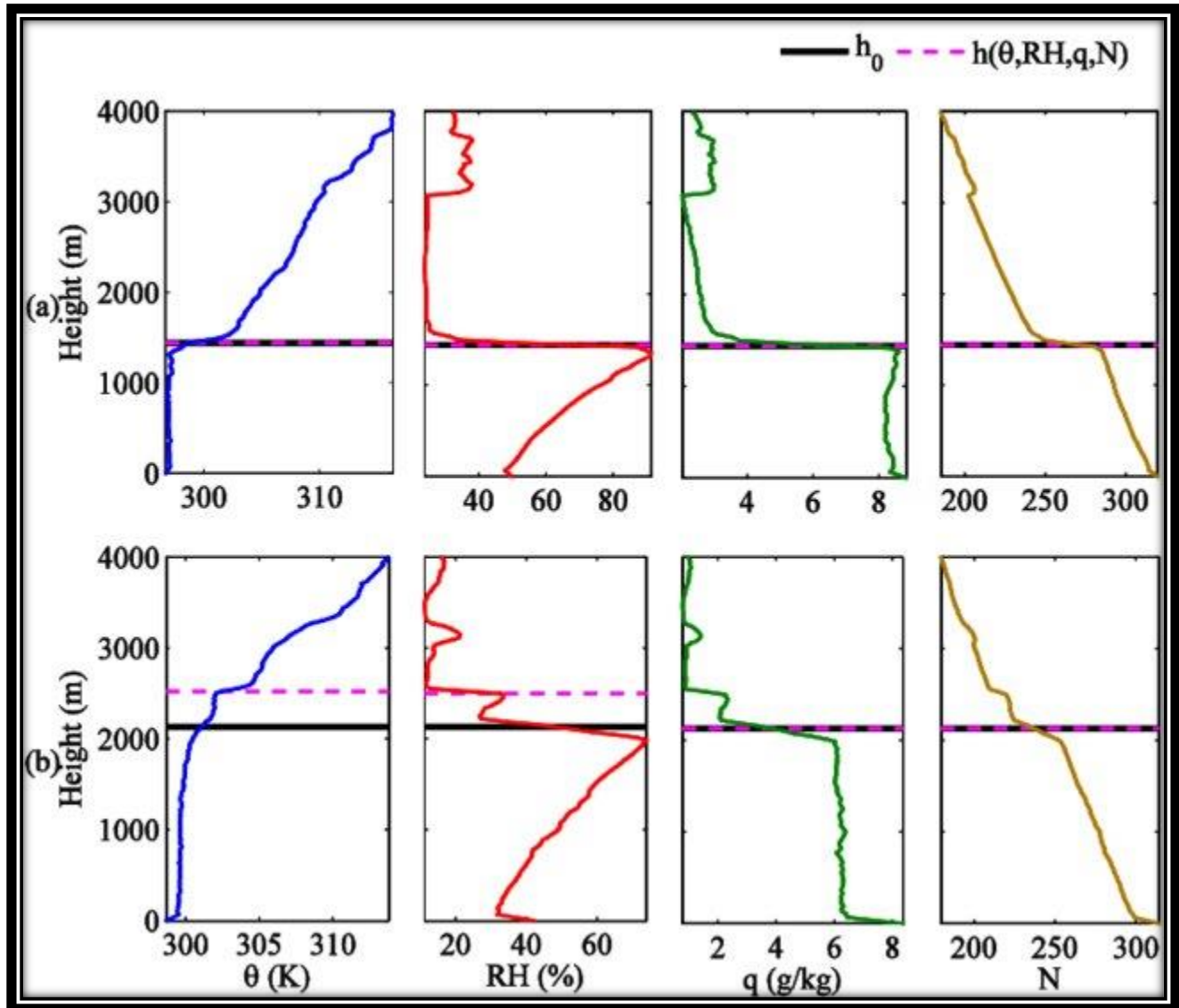


Figure 8- The vertical profiles of relative humidity ( $RH$ ), potential temperature ( $\theta$ ), specific humidity ( $q$ ), refractivity ( $N$ ), and the corresponding mixing layer height ( $h$ ) are derived from these profiles. The height above ground level is represented on the y-axis. Additionally, two representations of the mixing layer height determined by individual standards (magenta dotted line) and integrating the information of  $\theta$ ,  $RH$ ,  $q$ , and  $N$  (black solid line), are also displayed. Stations (a) and (b) represent profiles at Green Bay, WI for 00:00 UTC on 13 August 2006 and 00:00 UTC on 23 August 2006, respectively.

Source: Wang et al. 2014

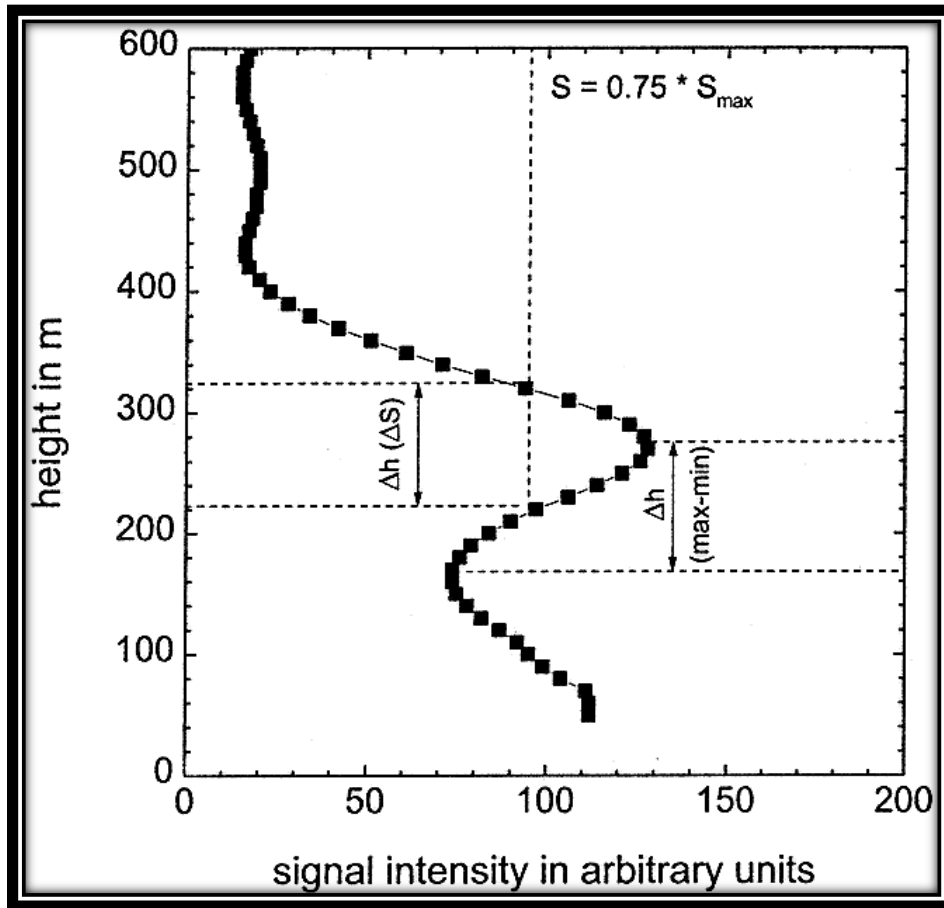


Figure 9- Visualization showcasing the utilization of profile-based methods to estimate the depth of the entrainment zone (EZ) from sodar backscatter intensity profiles.

Source: Beyrich et al. 1998

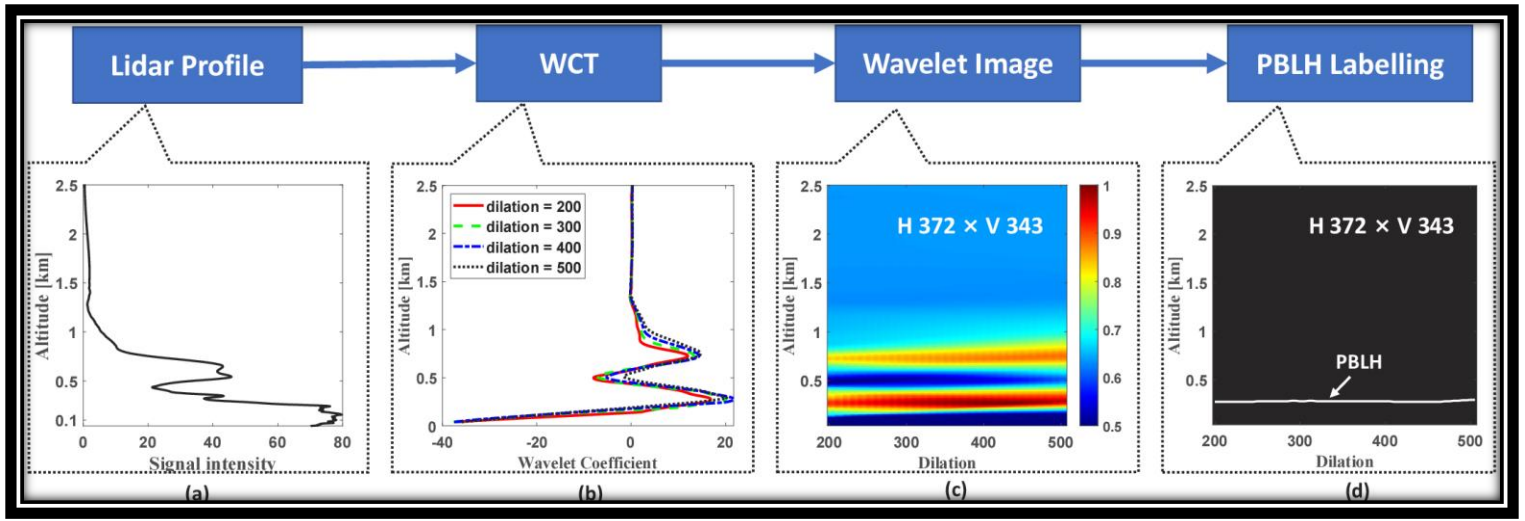


Figure 10- The diagram illustrates the process of generating the training set for PBL height calculation, comprising (a) a lidar profile (can be a radiosonde profile), (b) the Wavelet Coefficient Transformation (WCT) performed with varying dilation values, (c) a 2D wavelet image of dimensions and (d) the image with PBLH (Planetary Boundary Layer Height) labels. In the 2D wavelet image, brighter patterns (colored red or dark red) correspond to larger wavelet coefficients, indicating a higher gradient in the observation profile. The horizontal axis of figure (c) represents the dilation value ranging from 200 m to 505 m, while the vertical axis represents the measurement altitude. Notably, each pixel in the 2D wavelet image represents an altitude range interval of 7 m.

Source: Mei et al. 2022

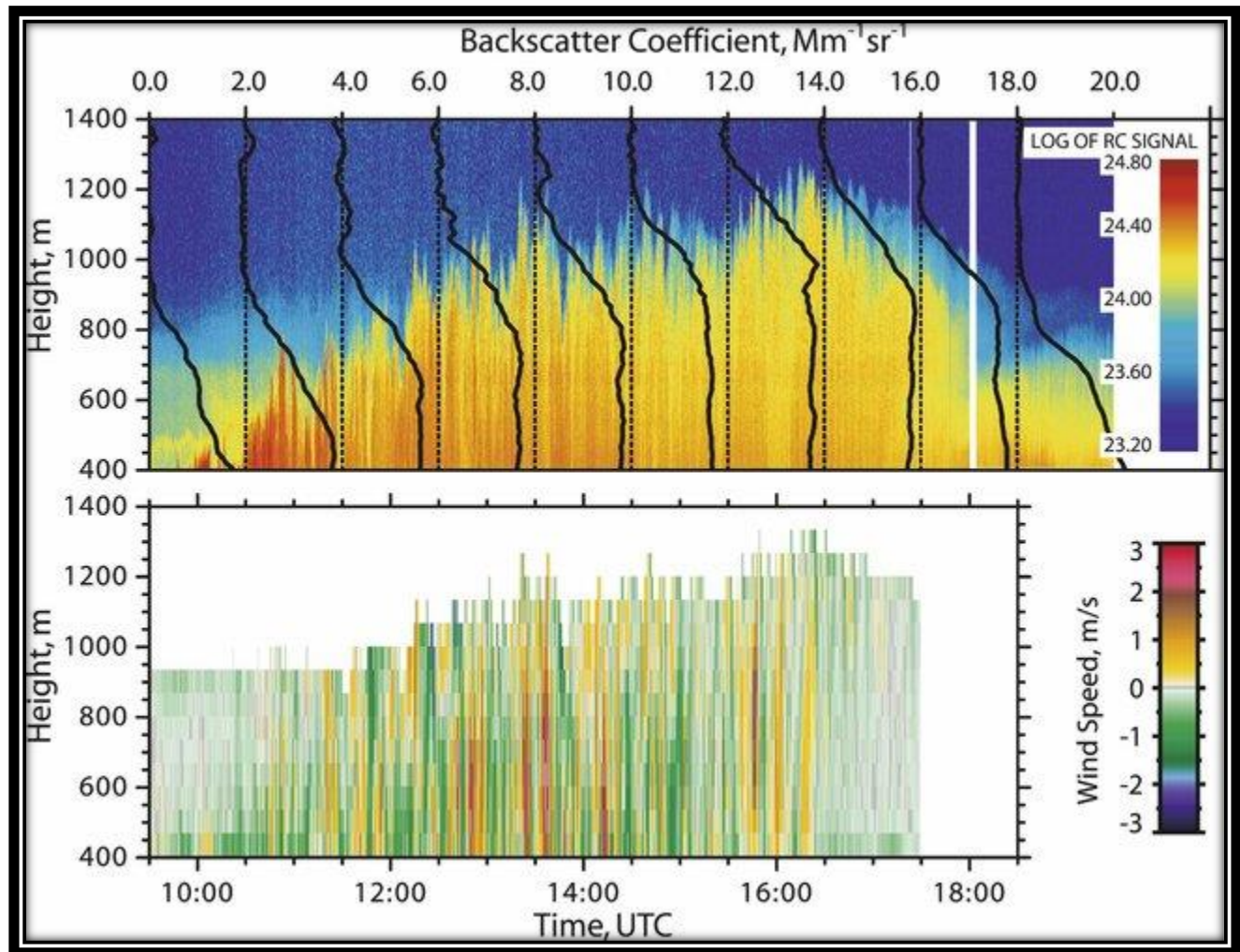


Figure 11- The development of the planetary boundary layer (PBL) was observed using both Raman lidar and Doppler wind lidar. The top figure displays the range-corrected 532-nm signal (resolution 7.5 m, 5 s), as well as 1-hour averaged profiles of the backscatter coefficient at 532 nm, which have been shifted by 2  $\text{Mm}^{-1}\text{sr}^{-1}$  or 1 hour. The bottom figure shows the corresponding vertical wind speed (resolution 75 m, 5 s).

Source: Engelmann et al. 2008

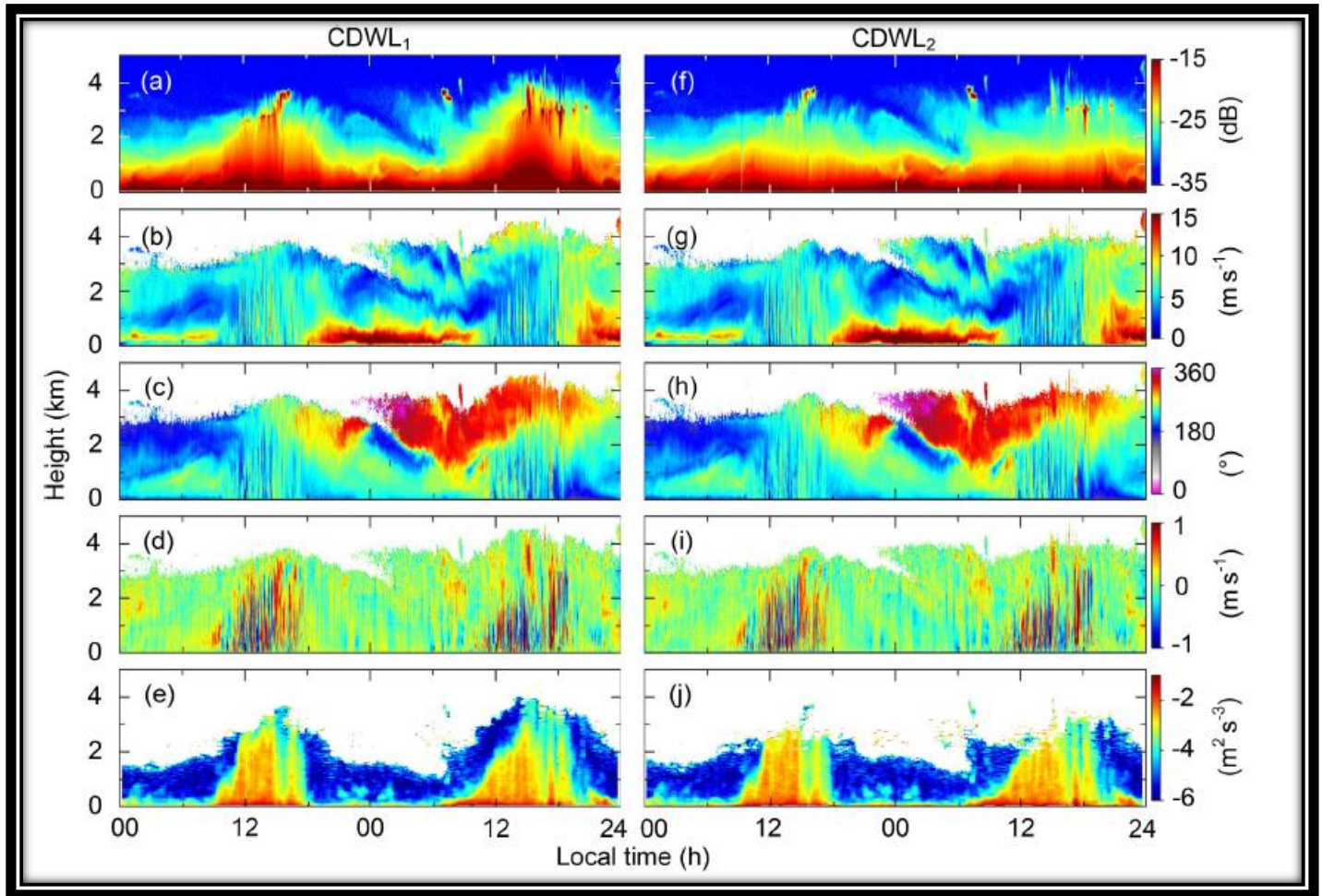


Figure 12- Results from a coherent Doppler wind lidar (CDWL) were used to observe various atmospheric parameters. These results are presented as follows: (a) aerosol-related parameters, such as aerosol backscatter coefficient or carrier-to-noise ratio (CNR); (b) horizontal wind speed; (c) horizontal wind direction, which is defined as  $0^\circ$  for northerly wind, rotating clockwise; (d) vertical wind speed, where negative values denote rising motion; (e) the logarithm of turbulence-related parameters, such as vertical wind speed variance or turbulent kinetic energy dissipation rate (TKEDR) for CDWL<sub>1</sub>. Results for CDWL<sub>2</sub> are presented in figures (f) to (j).

Source: Wang et al. 2021

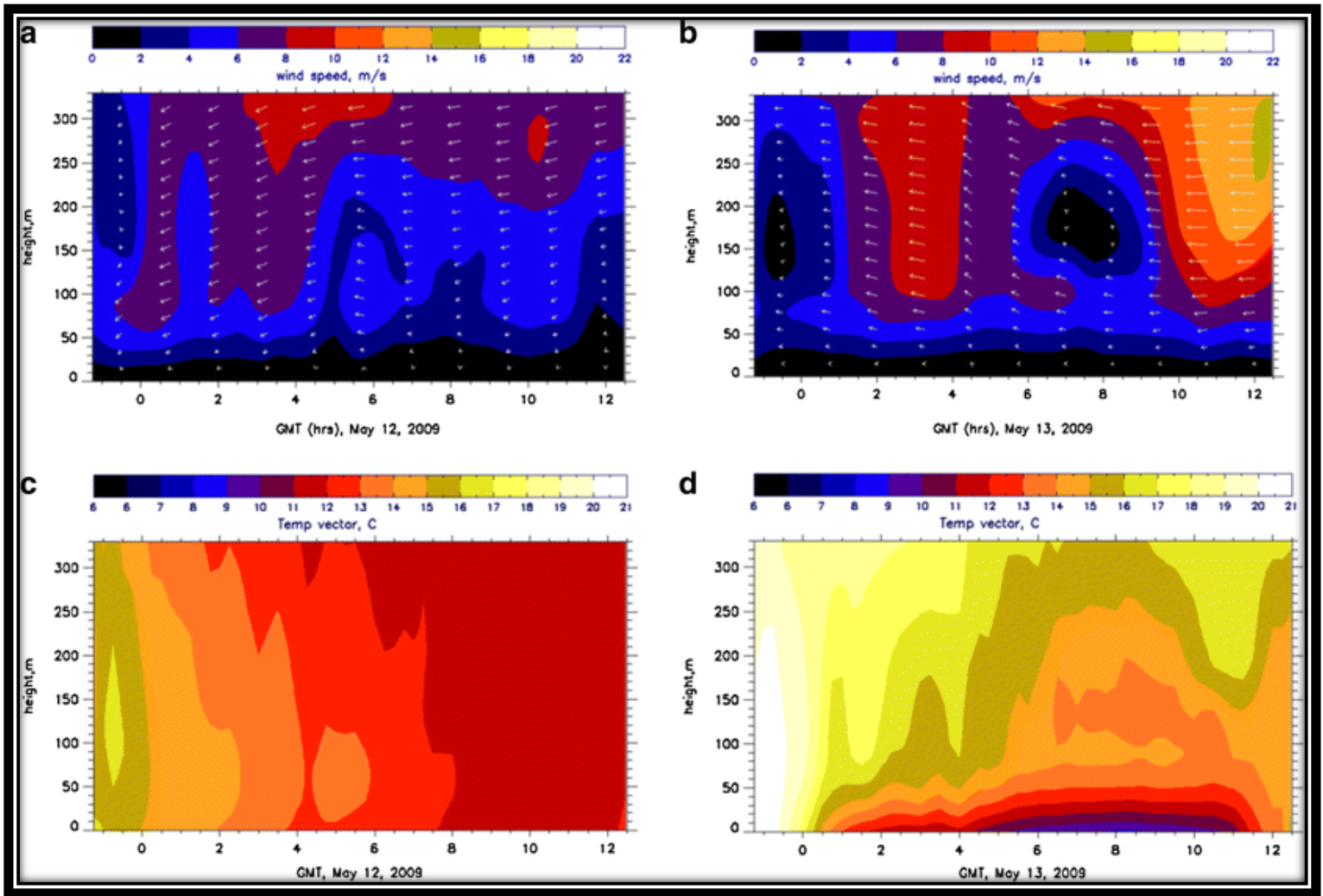


Figure 13- The following profiles were obtained using the Radio Acoustic Sounding System (RASS): (a) Night 1 wind speed and direction, (b) Night 2 wind speed and direction, (c) Night 1 temperature, and (d) Night 2 temperature. Attention should be devoted to the temporal evolution of the temperature and wind speed (GMT = Greenwich Meridian Time), where a clear boundary is formed indicated by the capping inversion and sharp transitions in wind speed intensity from convective to stable boundary layers.

Source: Werth et al. 2017

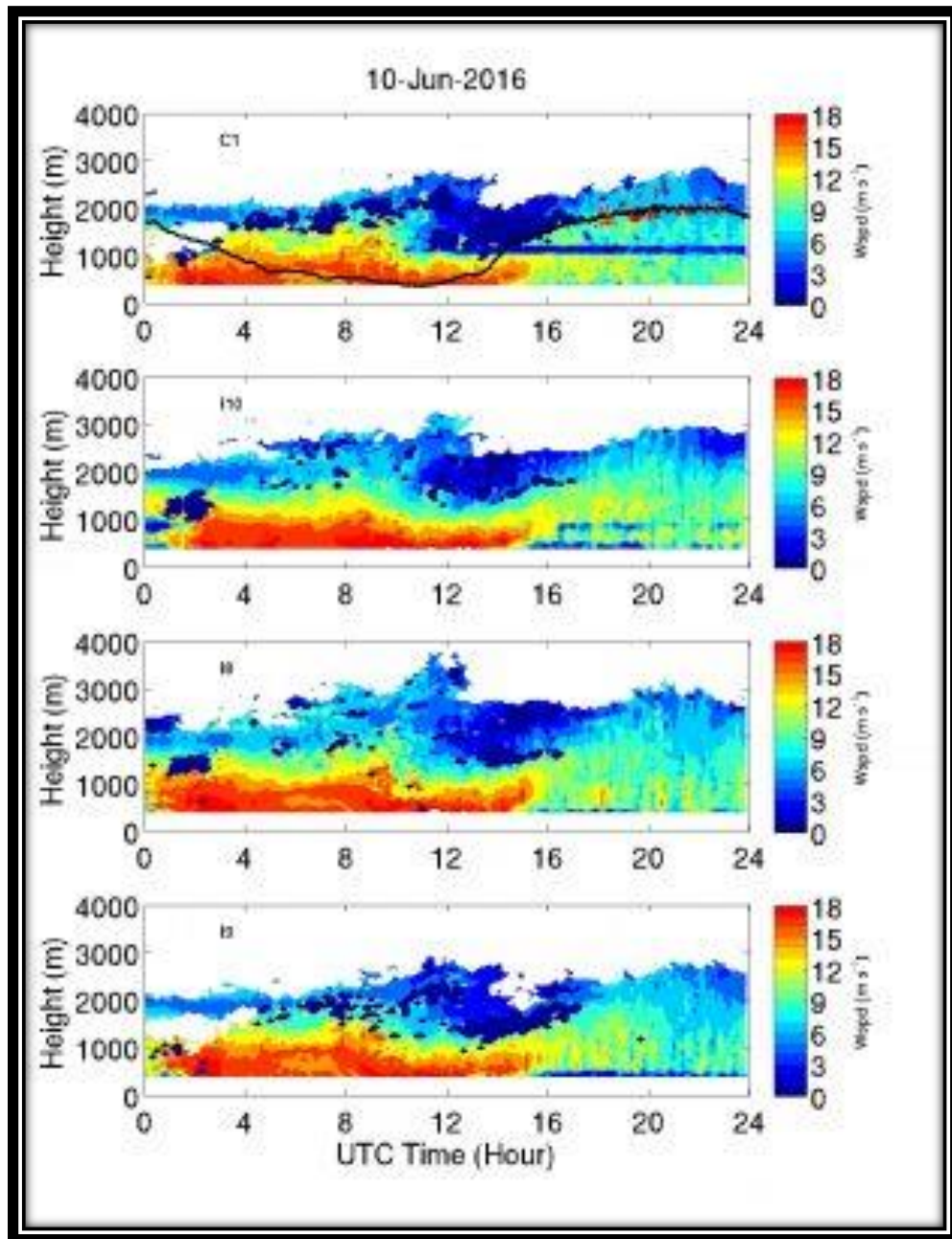


Figure 14- Displayed are time-height images depicting wind speed captured by radar wind profilers at four observing facilities within the Southern Great Plains. The wind speed is presented at a consistent resolution of 10 minutes and 50 meters. Each panel is accompanied by the name of the respective facility, positioned in the top left corner. The top panel of the images illustrates the first cloud base height recorded by ceilometers (highlighted in red) and the lifting condensation level, determined through surface measurements (also marked in red).

Source: [www.ARM.gov](http://www.ARM.gov)

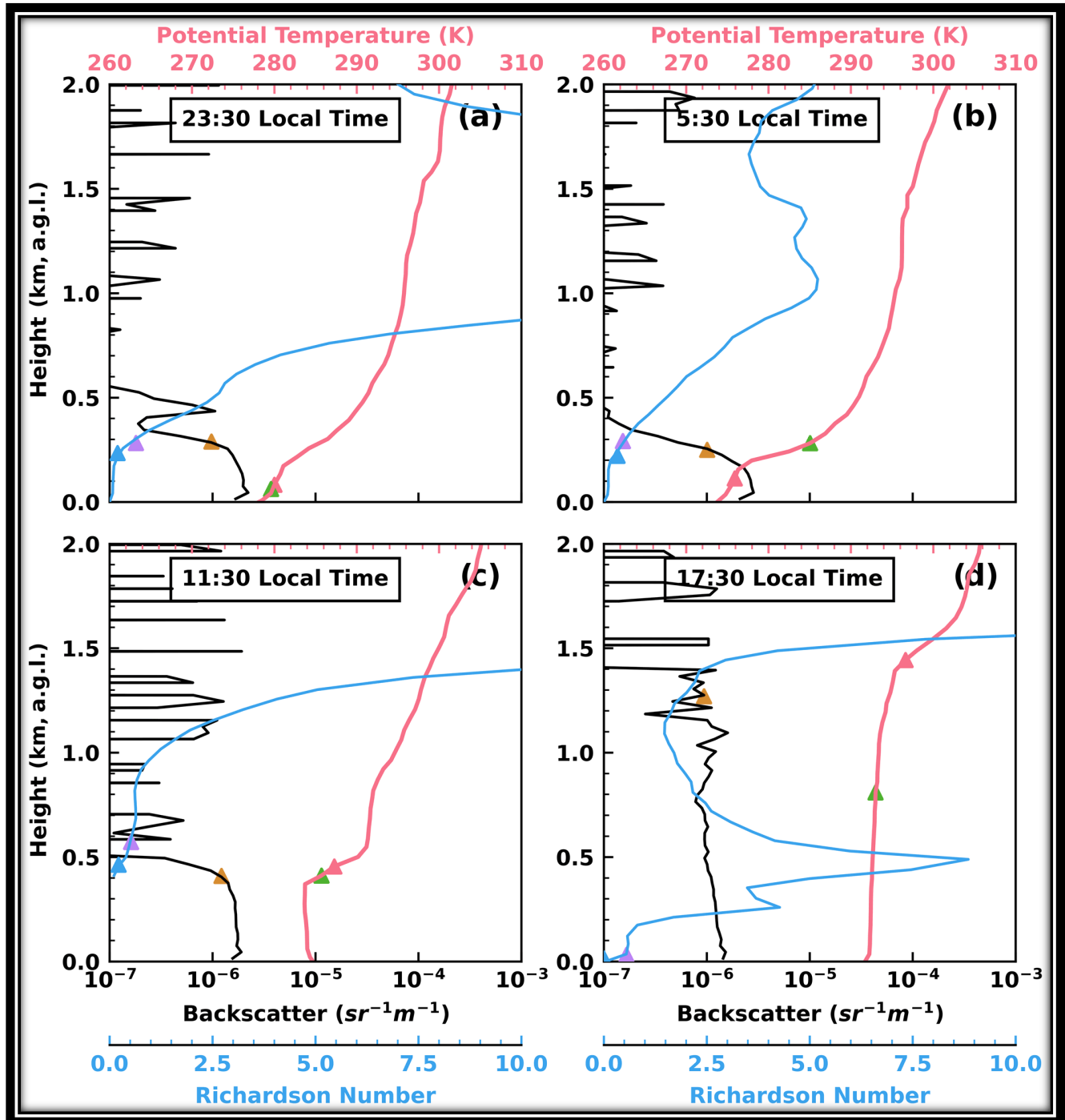


Figure 15- The profiles of ceilometer backscatter coefficient (black solid line), radiosonde-derived potential temperature (magenta solid line), and Richardson number (blue solid line) were recorded at the following radiosonde launching times on February 9th: (a) 23:30 local time (LT), (b) 05:30 LT on February 10th, (c) 11:30 LT on February 10th, and (d) 17:30 LT on February 10th.

Source: Zhang et. al. 2022

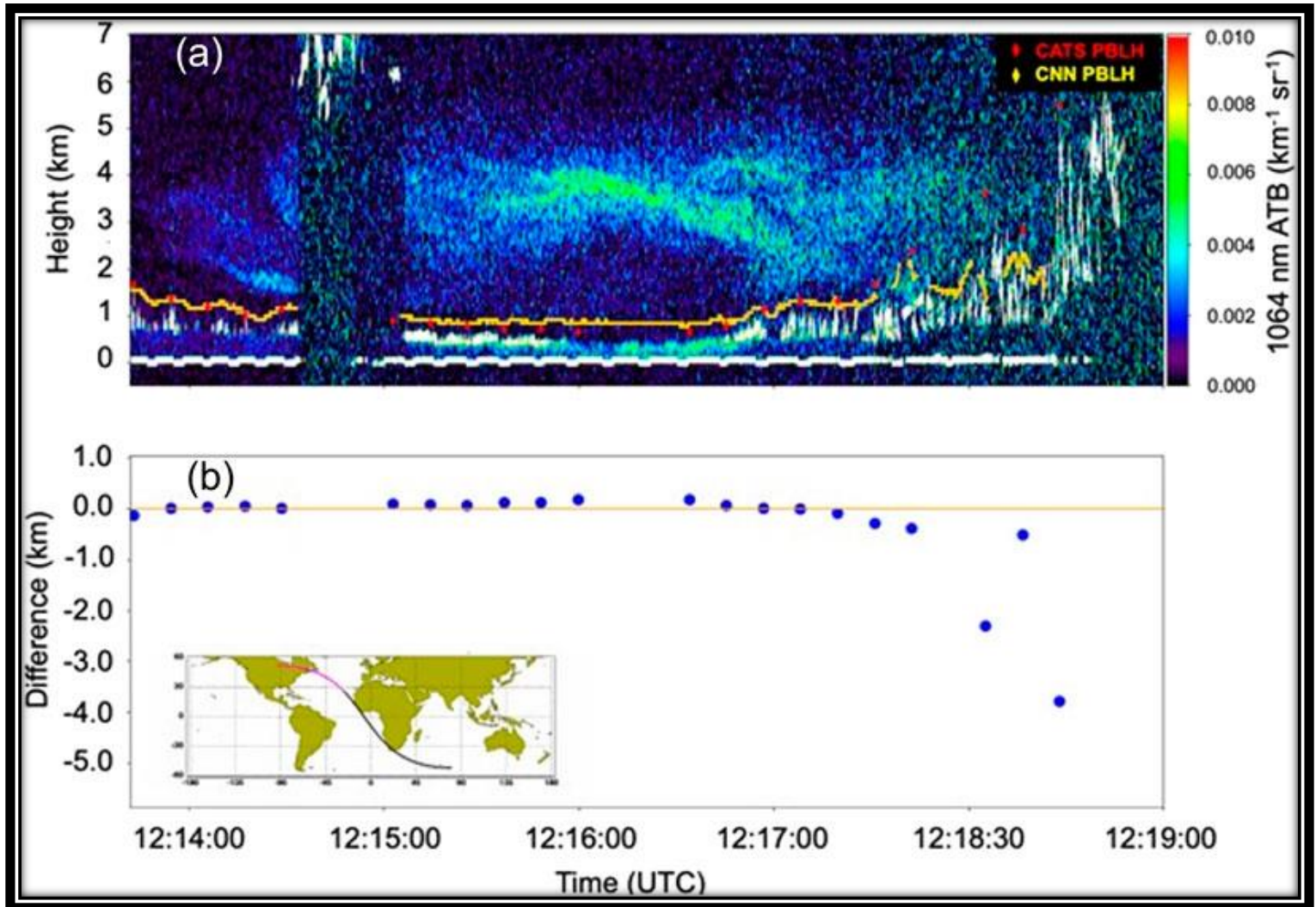


Figure 16- The attenuated total backscatter at 1064 nm from the satellite lidar Cloud-Aerosol Transport System (CATS) along the indicated track on the map inset was temporally recorded on September 15, 2015. The overlaid information includes the boundary layer height obtained from both the threshold technique (represented by red dots) and the Convolutional Neural Network (CNN) technique (represented by yellow dots). (B) The difference between the CNN and threshold techniques for the same scene can be observed.

Source: Palm et al. 2021

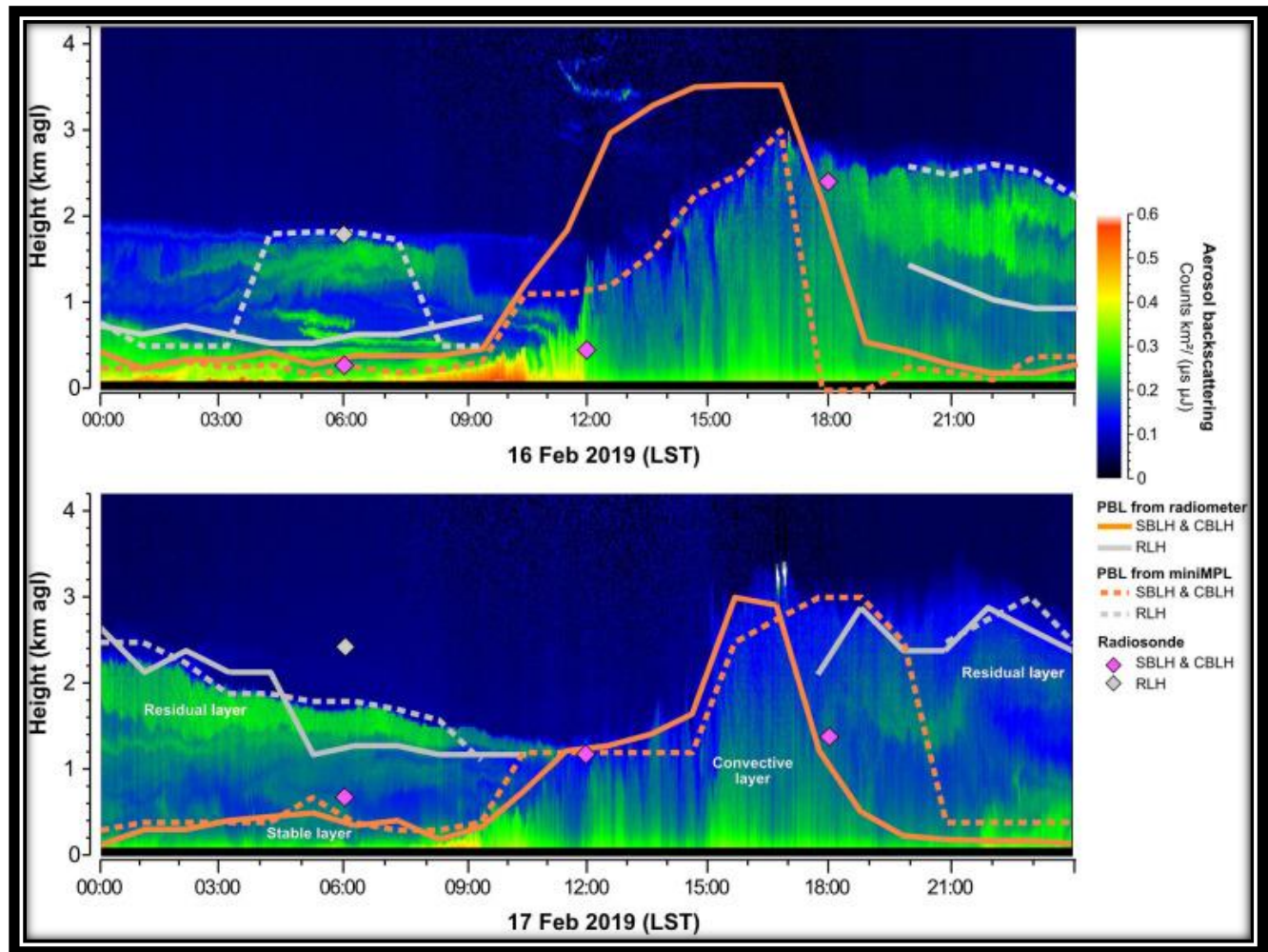


Figure 17- The intercomparison of attenuated total backscattering of PBL features such as stable boundary layer height (SBLH), convective boundary layer height (CBLH), and residual layer height (RLH) detected from a microwave radiometer (MWR), mini-Micro Pulse Lidar (MPL), and radiosondes (RS).

Source: Osibanjo et al. 2021

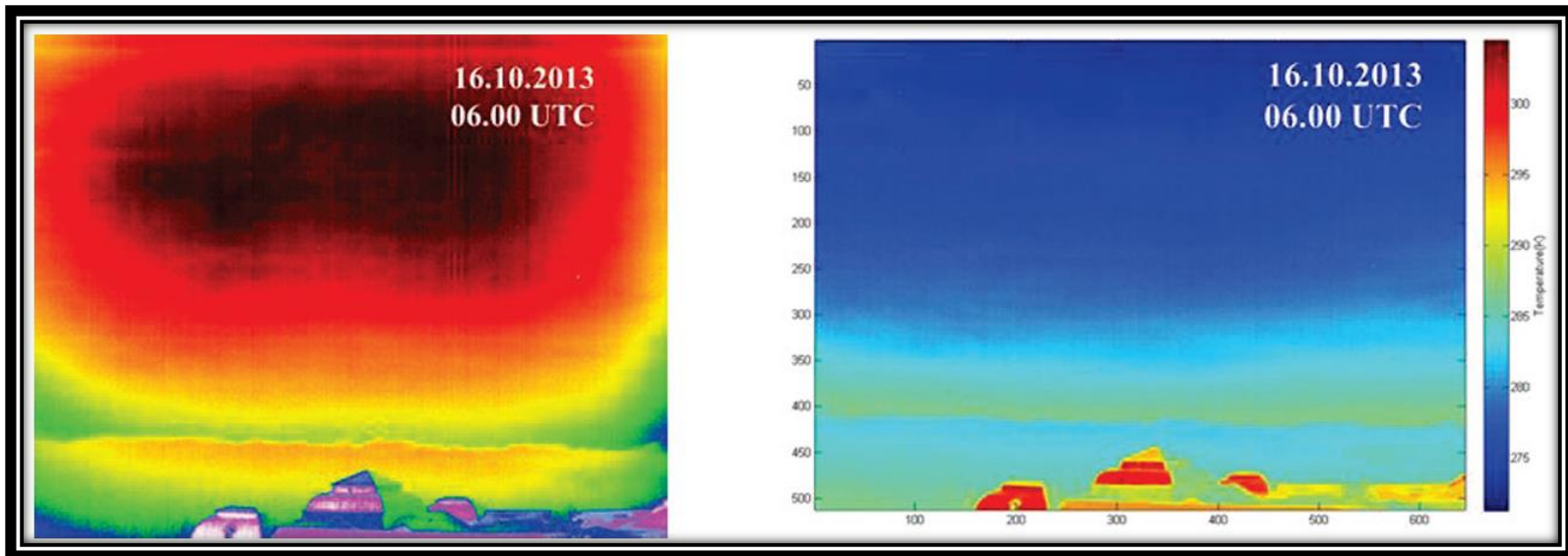


Figure 18- The image on the left is the raw image, while the image on the right is the processed IR image. Notice the raw image can be converted into a meaningful tool for temperature investigations through application of scripts and calibration curves. The processed IR image clearly shows the rising thermal inversion (e.g., capping inversion), a confident marker of PBL height.

Source: Albina et al. 2014

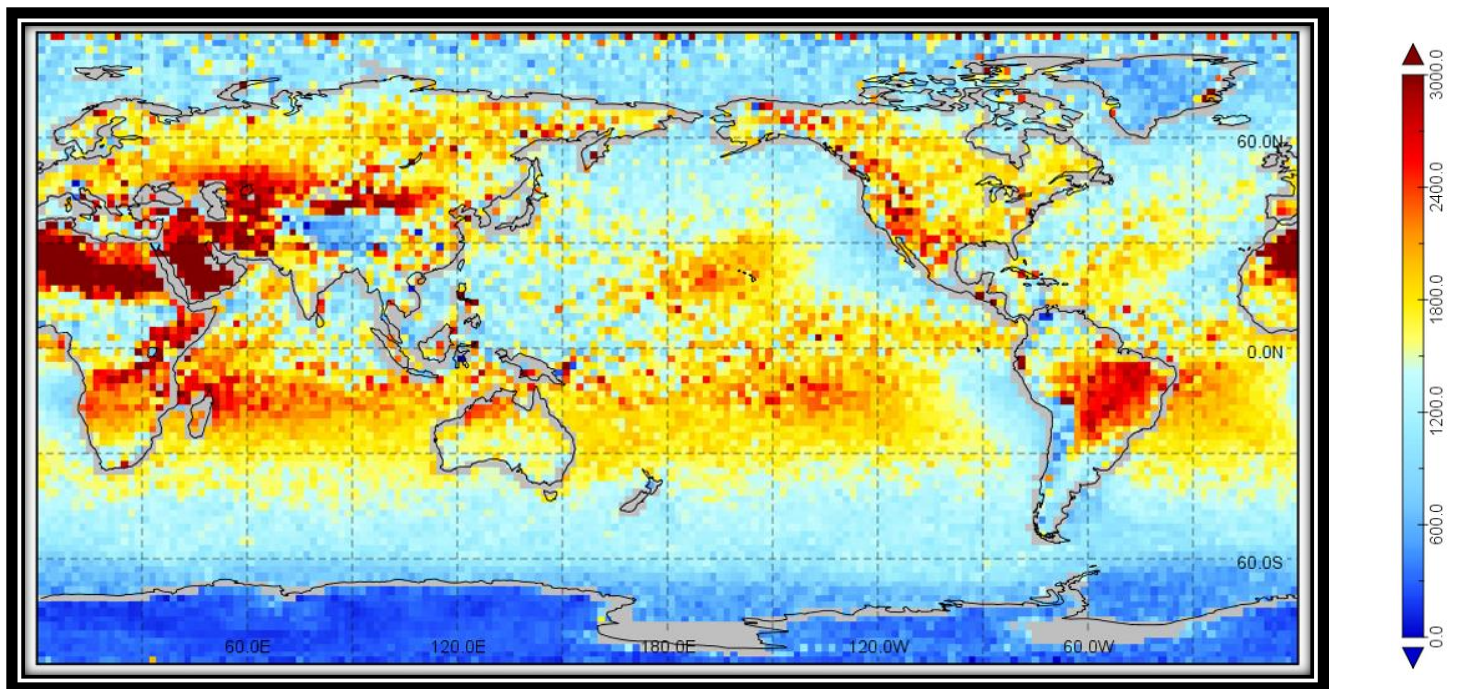


Figure 19- The depiction shows the 10-year seasonal mean of PBL height measured using GPS radio occultation (GPSRO). The figure indicates a reasonable daytime variation and spatial distribution of the PBL height, while noting the significant variability of resolution with different grid definitions. GPS occultation measurements offer a valuable complement to the limited spatial and temporal sampling of traditional single-point observations, such as radiosondes. The emergence of GPSRO has enabled global PBL sensing with high vertical resolution (approximately 100 meters) and an ability to conduct all-weather sounding.

Source: Ding et al. 2019

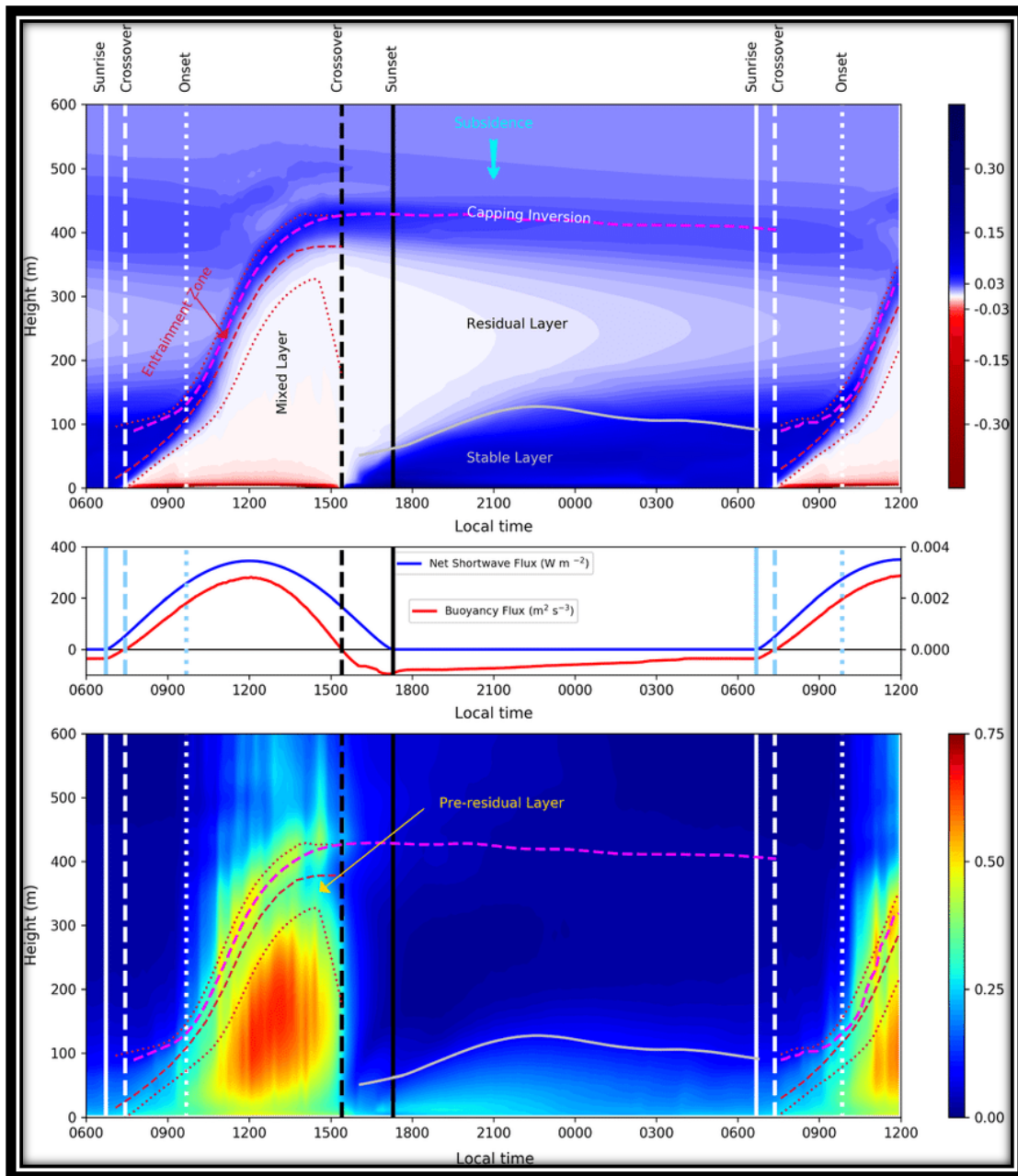


Figure 20- This figure presents a schematic representation of the diurnal cycle of the PBL obtained from a large-eddy simulation. Panel (a) shows the changes in the vertical gradient of the horizontally averaged potential temperature ( $\theta$ ), indicated by white and black vertical lines for different times during the morning and evening transitions. The height of the stable boundary layer is represented by a light grey line, while the elevated maximum of the  $\theta$  gradient is marked by a dashed magenta line. The dashed crimson line indicates the height of the minimum buoyancy flux during the unstable boundary layer period, while the crimson dotted lines indicate the upper and lower boundaries of the entrainment zone during the same period. The figure also highlights the rise of the entrainment zone, the development of the well-mixed layer, and the subsidence of the capping inversion after the evening transition. Panel (b) shows the evolution of the net downward shortwave flux at the surface and the surface buoyancy flux, while panel (c) presents the changes in the square root of the variance of the vertical velocity with height. The lines in panels (a) and (c) are consistent with those of panel (a), depicting the pre-residual layer. This representation helps in understanding the diurnal variability of the ABL, which plays a crucial role in atmospheric processes such as weather and climate.

Source: Angevine et al. 2020

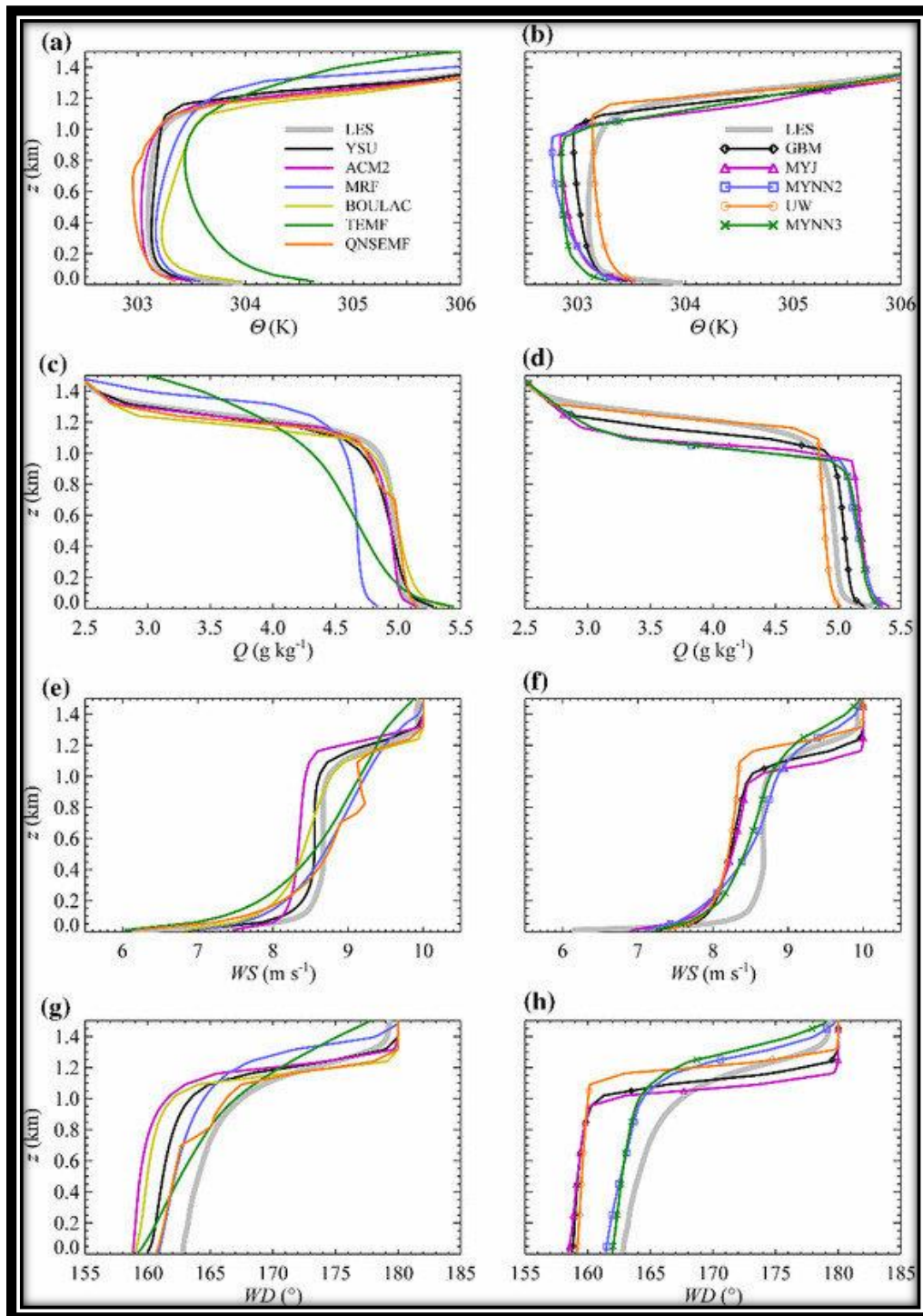


Figure 21- The figure depicts the vertical profiles obtained from 1-D model runs using 11 PBL schemes. The left panels represent the hybrid local and non-local schemes, while the right panels represent the local schemes. The potential temperature is depicted in panels (a) and (b), the water vapor mixing ratio in panels (c) and (d), the wind speed in panels (e) and (f), and the wind direction in panels (g) and (h). It should be noted that the lines representing the MYNN2 and MYNN3 schemes may overlap in some cases, making them indistinguishable. Notice the variability in their capturing of the PBL threshold (e.g.,  $\frac{d}{dx}$  variable  $\neq 0$ ).

Source: Wang et al. 2016

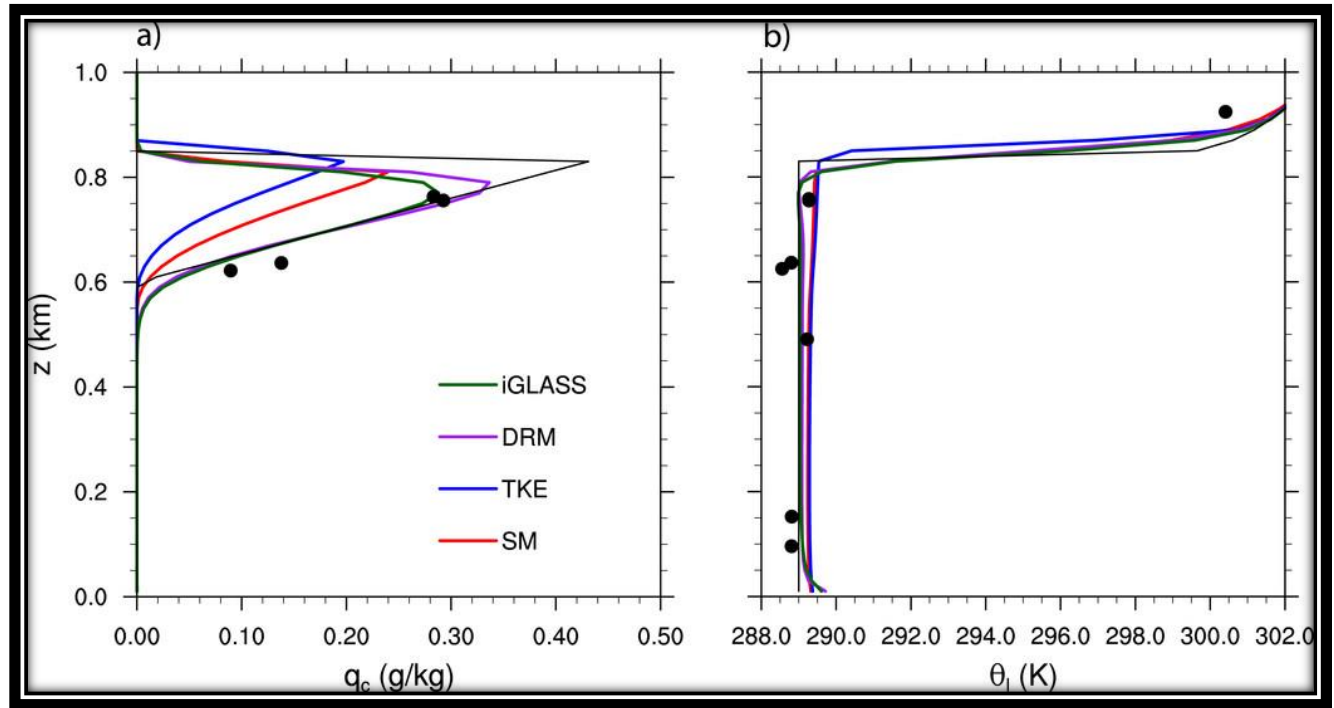


Figure 22- The figure displays the horizontal- and time-mean profiles of cloud water mixing ratio ( $q_c$ ) and liquid water potential temperature ( $\theta_l$ ) in the stratocumulus-capped boundary layer (SCBL) simulations. These simulations are performed using 1-km horizontal and 20-m vertical grid spacing. The black lines represent the initial conditions of  $q_c$  and  $\theta_l$ , while the black dots represent the observed values during the first research flight (RF01) of the Second Dynamics and Chemistry of Marine Stratocumulus field study (DYCOMS II). Panel (a) shows the  $q_c$  profile, and panel (b) shows the  $\theta_l$  profile. These profiles are crucial in understanding the behavior of SCBL and can be used to validate model results against observations.

Source: Shi et al. 2019

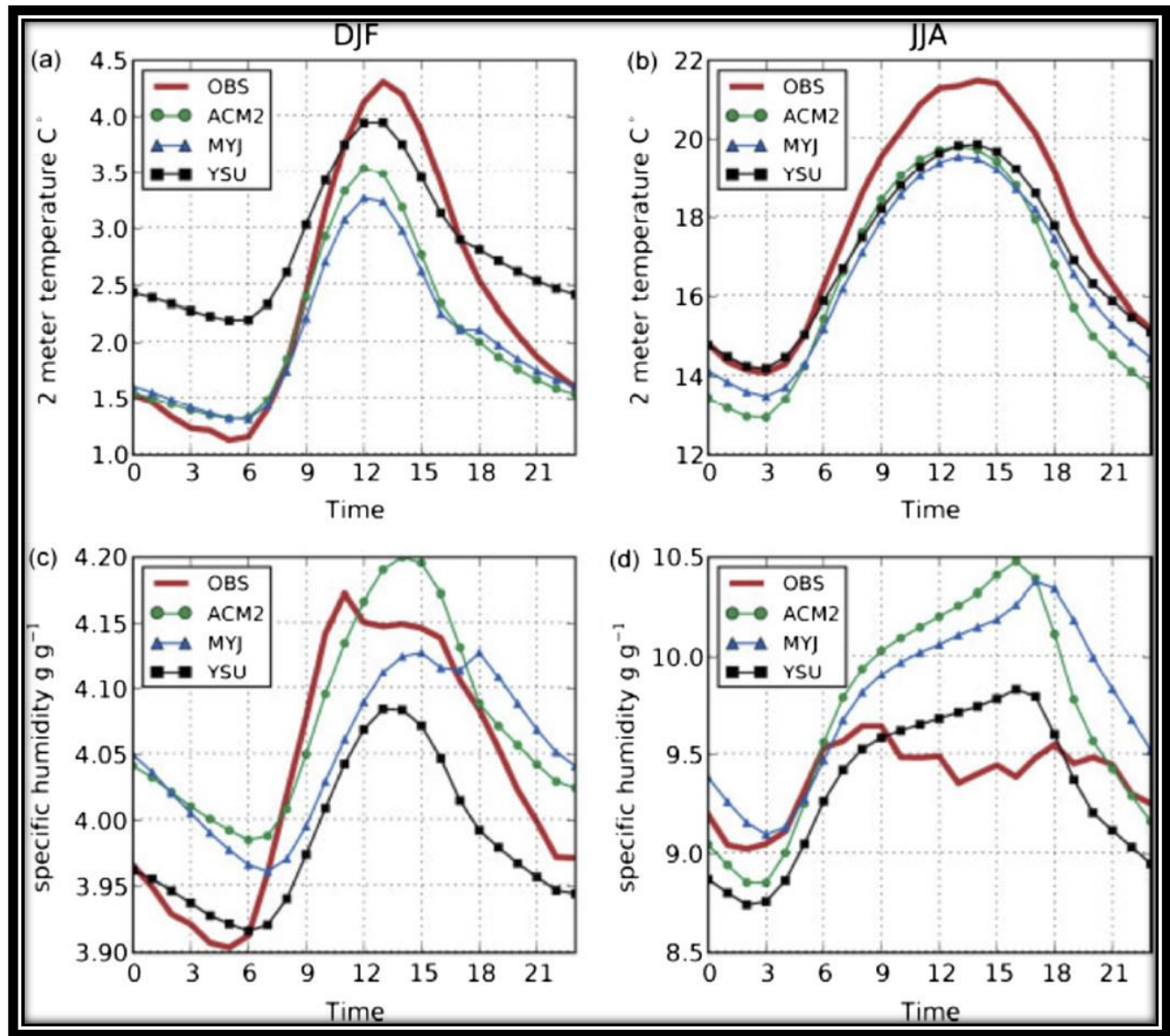
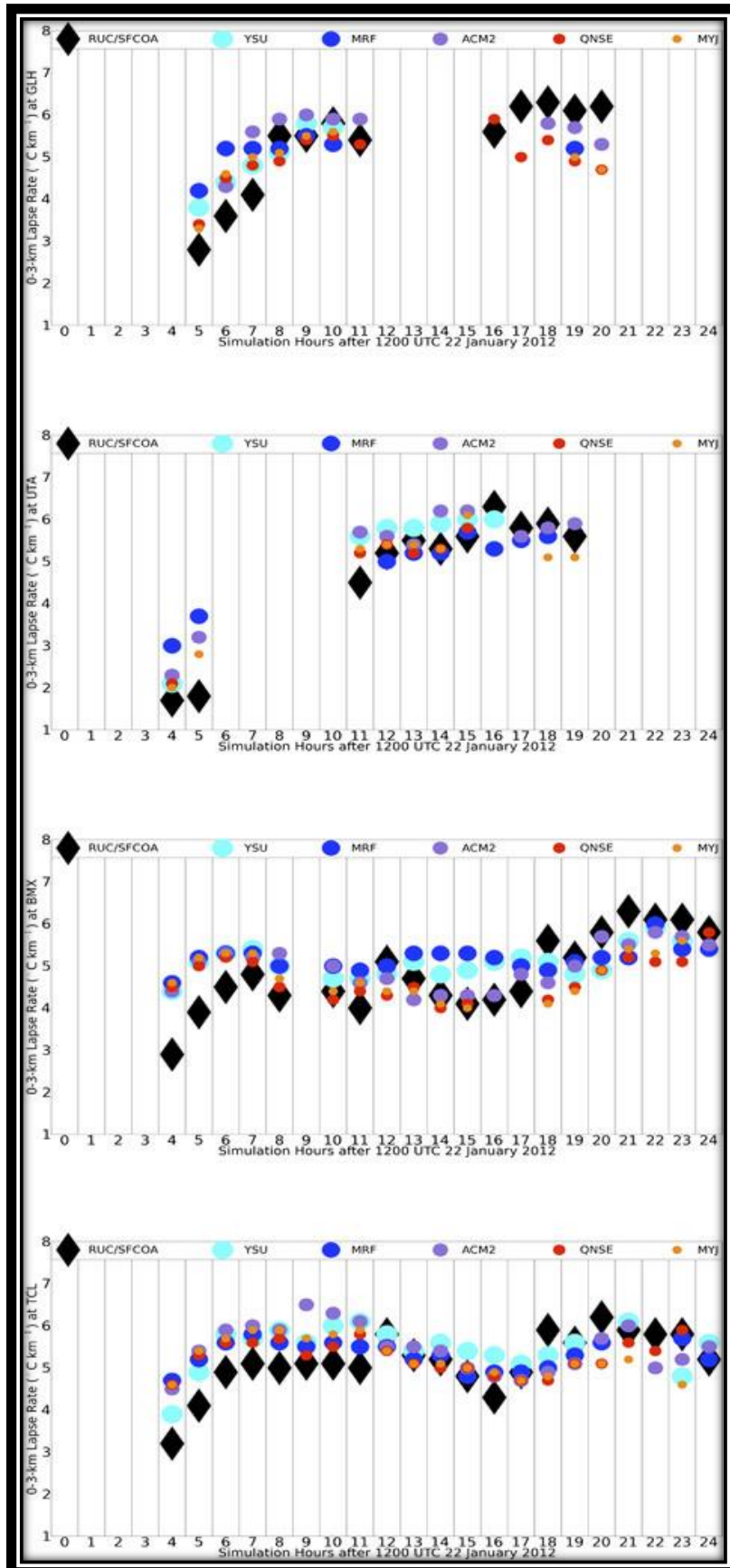


Figure 23- A comparative analysis of WRF PBL schemes against European synoptic observations (OBS), focusing on temperature and specific humidity in winter (a and c) and summer (b and c) seasons. The different profiles are represented by Asymmetric Convective Model version 2 (ACM2), Mellor–Yamada–Janjić (MYJ) and Yonsei University (YSU) schemes.

Source: Cohen et al. 2015



(Previous page) *Figure 24- A Comparison of 0–3-km Lapse Rates: Time Series Analysis of WRF Simulations (post 1200 UTC 31 Dec 2010) and Rapid Update Cycle (RUC) Storm Prediction Center (SPC) Surface Objective Analysis (SFCOA) Output at JAN, MEI, RLG, and BVN Sites (Jackson, Brookhaven, Raleigh, Meridian, Greenville, Tunica, Tuscaloosa, and Birmingham in Alabama). The marker colors and shapes indicate the PBL scheme employed in WRF Simulations and RUC–SFCOA output as per the legends. Cool colors (various shades of blue) denote nonlocal schemes, warm colors (red and orange) denote local schemes, purple represents the hybrid scheme (e.g., ACM2), and RUC–SFCOA Output is represented by black. Missing data implies soundings affected by convective contamination.*

Source: Cohen et al. 2015

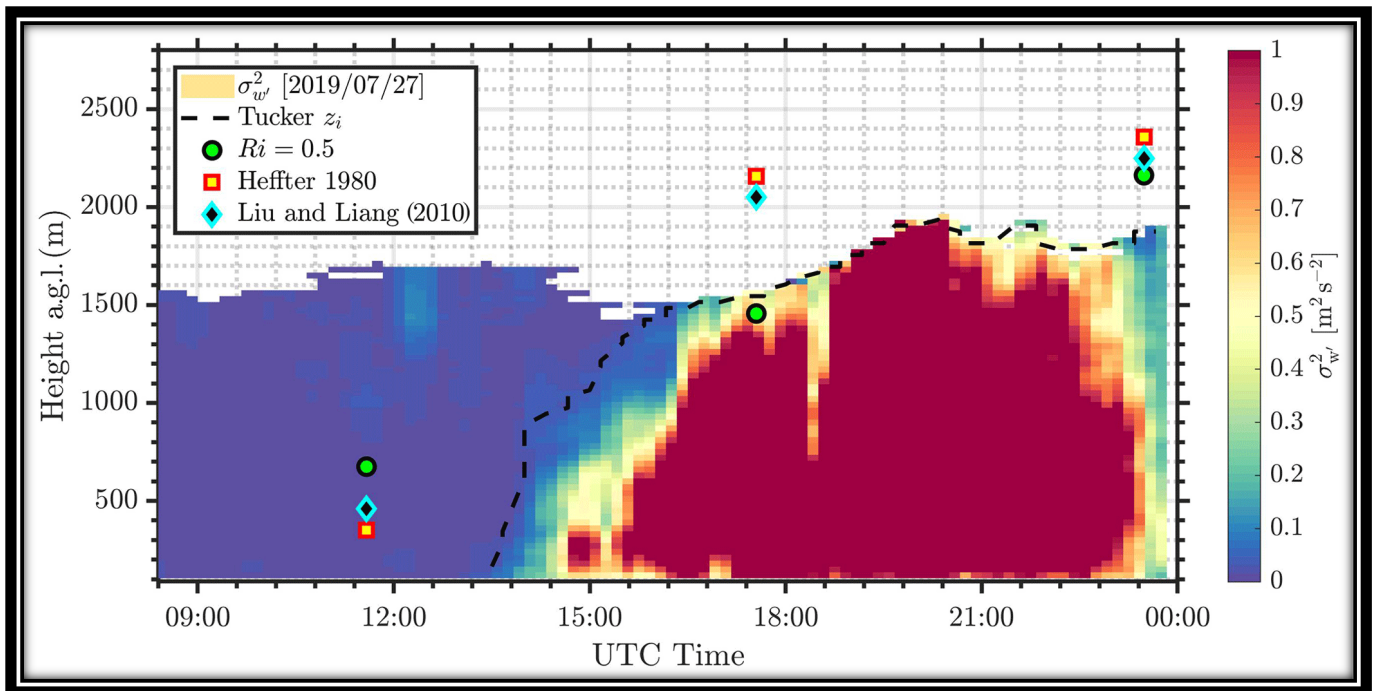


Figure 25- A standard CBL (Convective Boundary Layer) representation is depicted, illustrating the variations in lidar data (represented by colors). The black line corresponds to the Tucker  $z_i$  value, while the radiosonde  $z_i$  value is displayed using three distinct methods (represented by symbols). The horizontal axis represents the time elapsed in hours after 00:00 UTC on 27 July 2019. Note the differences between the different methods' abilities to capture the PBL height variations.

Source: Krishnamurthy et al. 2021

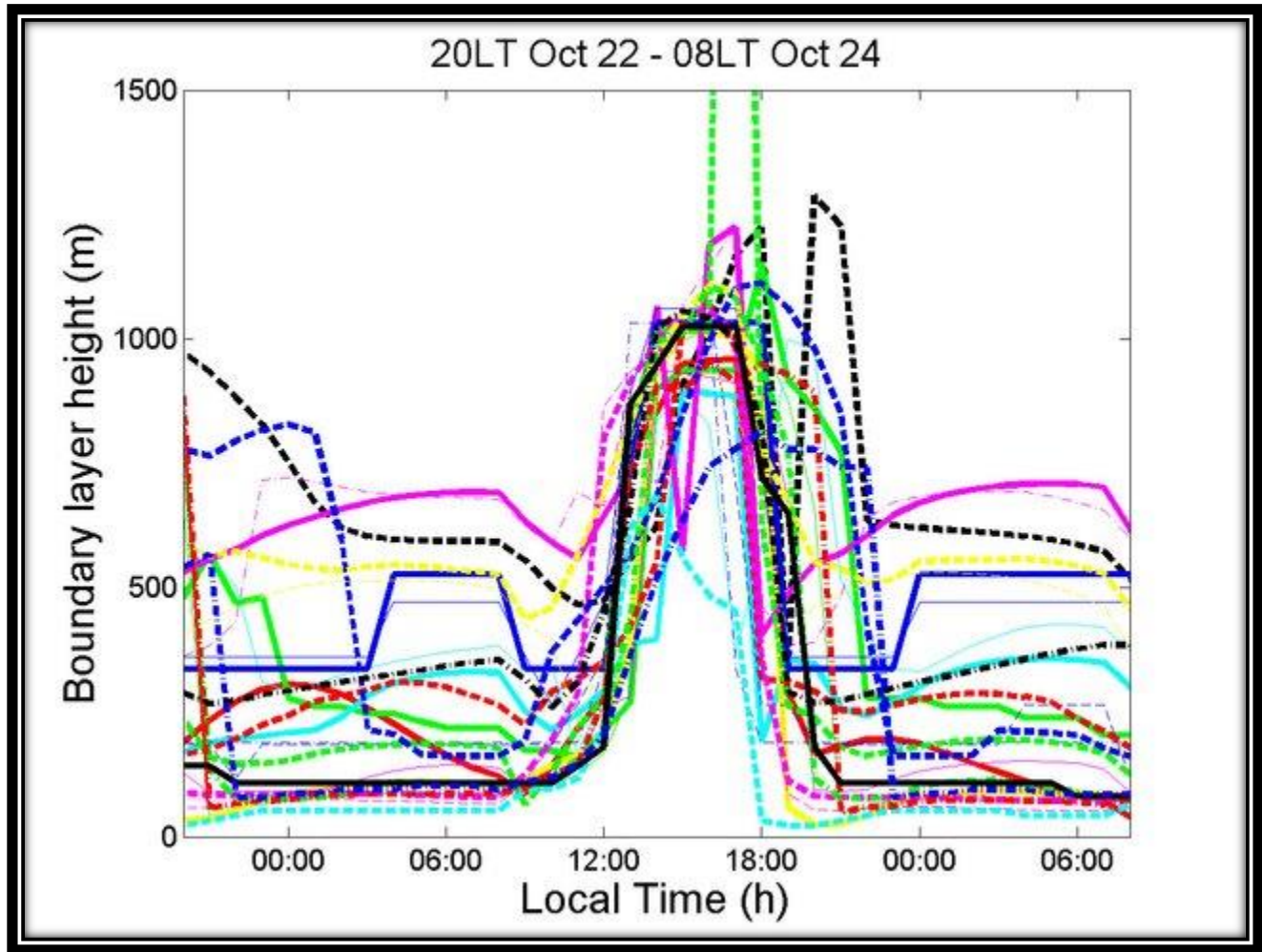


Figure 26- PBL height representations from several parameterization schemes (see Figure 27 for details to colors).

Source: Svensson et al. 2007

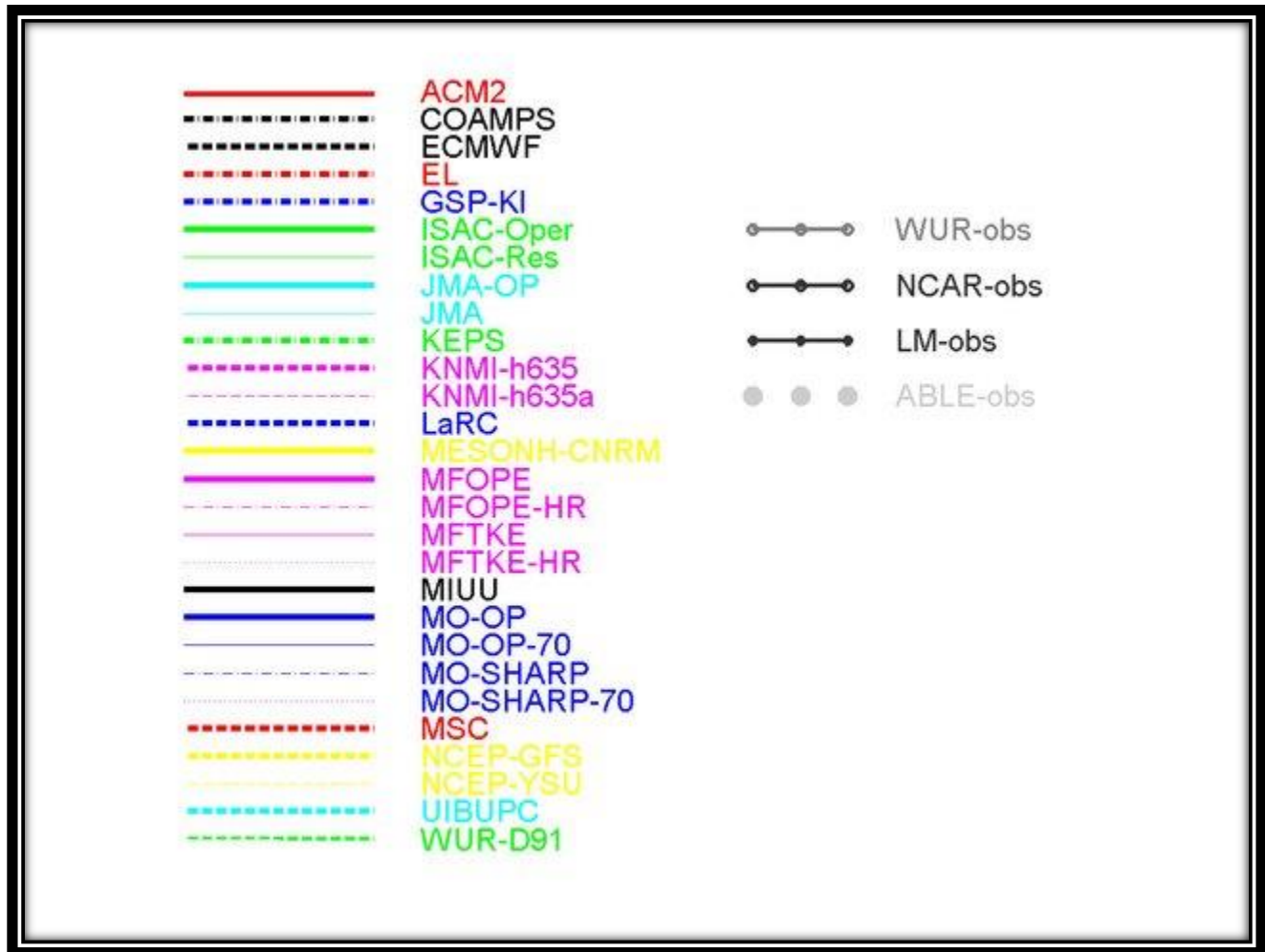


Figure 27- Legend for the models and their observations. A full list of participating models can be found in Svensson's study of GEWEX (<https://www.researchgate.net/publication/40114769>)

Source: Svensson et al. 2007

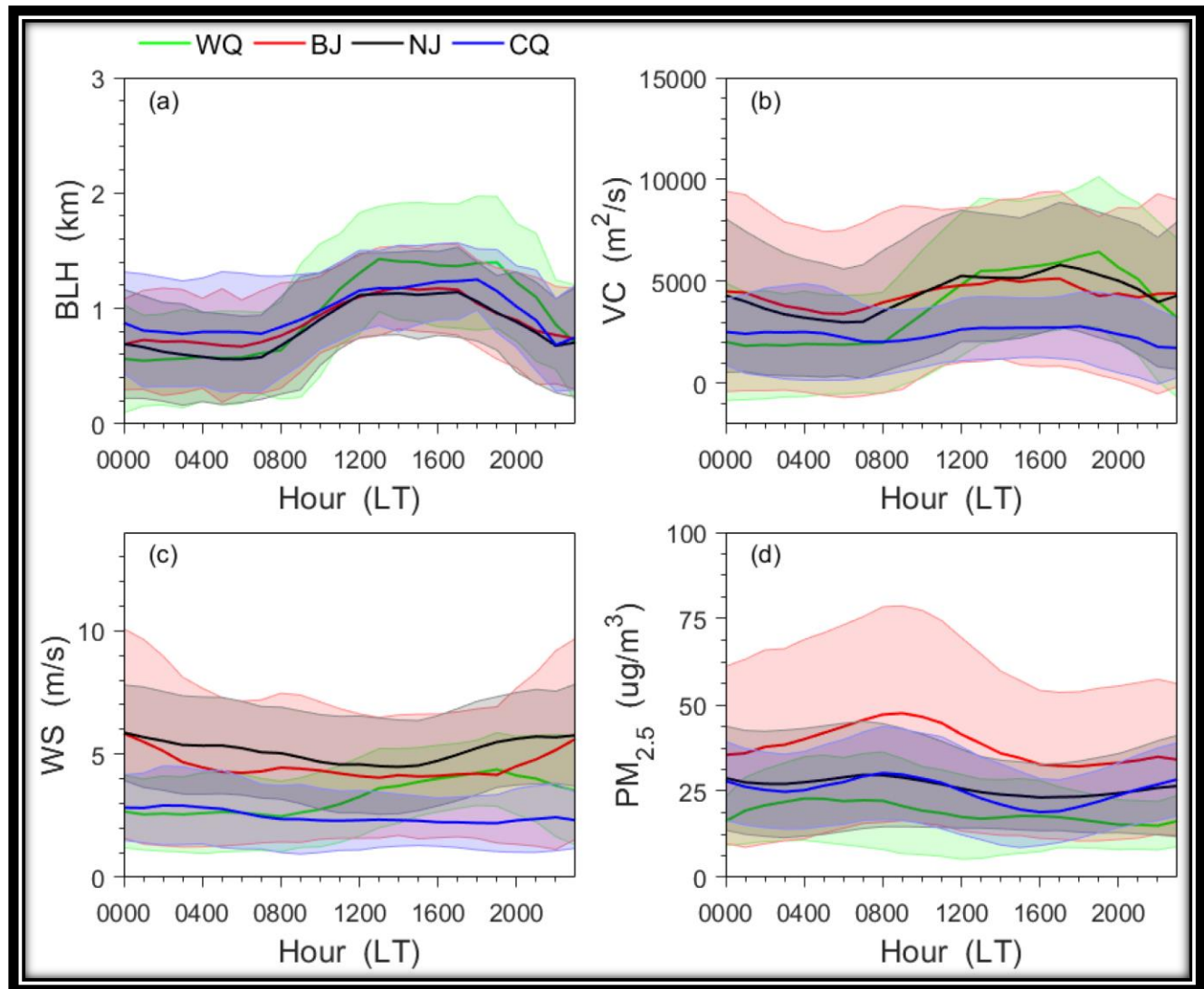


Figure 28- The diurnal averaged fluctuations of (a) Boundary Layer Height (BLH), (b) Ventilation Coefficient (VC), (c) Boundary Layer Wind Speed (WSBL), and (d) Particulate Matter with aerodynamic diameter  $\leq 2.5 \mu m$  ( $PM_{2.5}$ ) are observed at four monitoring profiler stations across Summer 2019 (June to August). Beijing (BJ), Nanjing (NJ), Chongqing (CQ), and Wulumuqi (WQ) sites are represented by green, red, black, and blue lines, respectively. The shaded regions of corresponding colors depict one standard deviation of each analyzed variable. Note the strong daily variation characteristics, with low values at nighttime that increase rapidly after sunrise. This showcases the wide temporal and spatial variability, creating the challenges present in modeling PBL height (and other atmospheric variables) across different locations.

Source: Liu et al. 2020

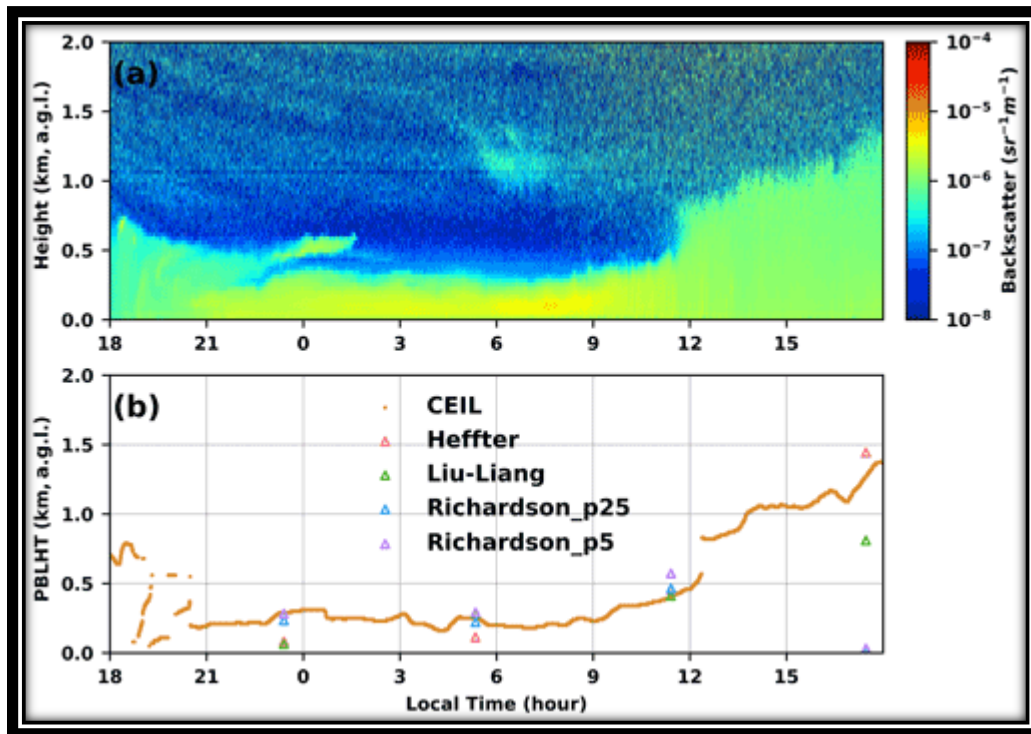


Figure 29- An illustration showcasing the estimated Planetary Boundary Layer Height (PBLHT) obtained from Atmospheric Radiation Measurement (ARM) ceilometer measurements and the radiosonde-estimated PBLHT (PBLHT-SONDE) Value-Added Product (VAP) on 9-10 February 2015, at the fixed-location atmospheric observatory at US Southern Great Plains (ARM SGP) site. (a) A time-height cross section displaying the total attenuated backscatter coefficient captured by the ceilometer. (b) The estimated PBLHTs derived from ceilometer measurements (labeled as "CEIL") and the PBLHT-SONDE VAP, utilizing the Heffter method (labeled as "Heffter"), Liu and Liang method (labeled as "Liu-Liang"), and bulk Richardson number method (labeled as "Richardson\_p25" using Ric of 0.25, and labeled as "Richardson\_p5" using Ric of 0.5). Note the different abilities between each method, some capturing different PBL height profiles.

Source: Zhang et al. 2022

#### ACKNOWLEDGEMENTS

The author would like to be made to the National Oceanic and Atmospheric Administration (NOAA) Award# NA16SEC4810006; Dr. Xinrong Ren and Mr. Phillip Stratton of NOAA's Air Resources Laboratory (ARL), Atmospheric Sciences Modeling Division; Dr. Xin-Zhong Liang of University of Maryland's Earth System Modeling Group (EaSM); Dr. Jo-Anne Butty and Dr. Charles Ichoku of the NOAA Cooperative Science Center in Atmospheric Sciences and Meteorology (NCAS-M); NOAA Center for Weather and Climate Prediction (NCWCP); and the NOAA Cooperative Science Center in Atmospheric Sciences and Meteorology (NCAS-M). Without their guidance and supervision, this manuscript would not have been possible.